Deep Learning-based Brain Tumour Image Segmentation and its Extension to Stroke Lesion Segmentation

A thesis submitted in fulfilment of the requirement for the degree of Doctor of Philosophy

By

SALMA ALI RIDHA AL-QAZZAZ

B.Sc., M.Sc.

School of Engineering

Cardiff University

UK

2020

DECLARATION AND STATEMENTS

DECLARATION

This work has not previously been accepted in substance for any degree and is not concurrently submitted in candidature for any degree.

Signed ……..….... Date…….…….

STATEMENT 1

This thesis is being submitted in partial fulfilment of the requirements for the degree of Doctor of Philosophy (PhD).

Signed ……..…. Date…….…….

STATEMENT 2

This thesis is the result of my own independent work/investigation, except where otherwise stated. Other sources are acknowledged by explicit references.

Signed ……..… Date…….…….

STATEMENT 3

I hereby give consent for my thesis, if accepted, to be available for photocopying and inter-library loan, and for the title and summary to be made available to outside organisations.

Signed ……..…. Date…….…….

ABSTRACT

Medical imaging plays a very important role in clinical methods of treating cancer, as well as treatment selection, diagnosis, an evaluating the response to therapy. One of the best-known acquisition modalities is magnetic resonance imaging (MRI), which is used widely in the analysis of brain tumours by means of acquisition protocols (e.g. conventional and advanced). Due to the wide variation in the shape, location and appearance of tumours, automated segmentation in MRI is a difficult task. Although many studies have been conducted, automated segmentation is difficult and work to improve the accuracy of tumour segmentation is still ongoing.

This research aims to develop fully automated methods for segmenting the abnormal tissues associated with brain tumours (i.e. those subject to oedema, necrosis and enhanced) from the multimodal MRI images that help radiologists to diagnose conditions and plan treatment.

In this thesis the machine-learned features from the deep learning convolutional neural network (CIFAR) are investigated and joined with hand-crafted histogram texture features to encode global information and local dependencies in the representation of features. The combined features are then applied in a decision tree (DT) classifier to group individual pixels into normal brain tissues and the various parts of a tumour. These features are good point view for the clinicians to accurately visualize the texture tissue of tumour and sub-tumour regions. To further improve the segmentation of tumour and sub-tumour tissues, 3D datasets of the four MRI modalities (i.e. FLAIR, T1, T1ce and T2) are used and fully convolutional neural networks, called SegNet, are constructed for each of these four modalities of images. The outputs of these four SegNet models are then fused by choosing the one with the highest scores to construct feature maps, with the pixel intensities as an input to a DT classifier to further classify each pixel as either a normal brain tissue or the component parts of a tumour. To achieve a high-performance accuracy in the segmentation as a whole, deep learning (the

SegNet network) and the hand-crafted features are combined, particularly in the grey-level co-occurrence matrix (GLCM) in the region of interest (ROI) that is initially detected from FLAIR modality images using the SegNet network.

The methods that have been developed in this thesis (i.e. CIFAR _PI_HIS _DT, SegNet_Max_DT and SegNet_GLCM_DT) are evaluated on two datasets: the first is the publicly available Multimodal Brain Tumour Image Segmentation Benchmark (BRATS) 2017 dataset, and the second is a clinical dataset.

In brain tumour segmentation methods, the F-measure performance of more than 0.83 is accepted, or at least useful from a clinical point of view, for segmenting the whole tumour structure which represents the brain tumour boundaries. Thanks to it, our proposed methods show promising results in the segmentation of brain tumour structures and they provide a close match to expert delineation across all grades of glioma.

To further detect brain injury, these three methods were adopted and exploited for ischemic stroke lesion segmentation. In the steps of training and evaluation, the publicly available Ischemic Stroke Lesion (ISLES 2015) dataset and a clinical dataset were used. The performance accuracies of the three developed methods in ischemic stroke lesion segmentation were assessed. The third segmentation method (SegNet_GLCM_DT) was found to be more accurate than the other two methods (SegNet_Max_DT and SegNet_GLCM_DT) because it exploits GLCM as a set of hand-crafted features with machine features, which increases the accuracy of segmentation with ischemic stroke lesion.

ACKNOWLEDGEMENTS

I am grateful to my God “ALLAH”, the Prophet Muhammad, and Ahl al-Bayt and their corresponding (the peace and blessings of Allah be upon them) for giving me the strength and the ability to attain this goal.

My sincere appreciation and gratitude go to my supervisor Doctor Xianfang Sun for his continuous valuable advice and guidance, and his constructive feedback on my thesis. Thank you for all the skills I learned from you and thank you for being a great supervisor.

I would like to thank my supervisor Doctor XinYang and Professor Leonard Derek Nokes for providing me with necessary information and direction.

I express my gratitude to my lovely husband Mr Ali Magsoosi for his help, guidance, and support during my study.

I dedicate this work to my wonderful family. Mum, Dad, my amazing sons, my beautiful daughter, my dear brothers, and sister. It is a pleasure to have them in my life.

I deeply appreciate the financial support of my sponsor, HCED and the University of Baghdad. Without their support and immediate help, this work would not have been achievable.

I would like also to thank all the members of the Biomedical Engineering Department at Cardiff University for their kind assistance.

Salma Alqazzaz

December 2019

TABLE OF CONTENTS

Table of Contents

LIST OF ABBREVIATIONS

ADC	Apparent diffusion coefficient
BRATS	Multimodal brain tumour image segmentation benchmark
C-MRI	Conventional MR images
CNNs	Convolutional neural networks
CONV	Convolutional layer
CRF	Conditional random field
CSF	Cerebrospinal fluid
CT	Computed tomography
D_{tree}	Tree depth
DNNs	Deep neural networks
DSC	Dice similarity score
DT	Decision tree
DTI	Diffusion tensor imaging
DWI	Diffusion weighted imaging
ET	Echo time
ET	Enhanced tumour
FC	Fully convolutional layers
FCN	Fully convolutional networks
FID	Free induction
FLAIR	Fluid attenuated inversion recovery
FN	False negative
FP	False positive
GBMs	Glioblastomas
Gd	Gadolinium
GLCM	Grey-level co-occurrence matrix
GM	Grey matter
HGG	High grade glioma
ISLES	Ischemic stroke lesion
LGG	Low grade glioma
MRI	Magnetic resonance imaging
NMR	Nuclear magnetic resonance
NMV	Net magnetisation vector

PET	Positron emission tomography
POOL	Pooling layers
PPV	Positive predictive value
RF	Random decision forest
ROI	Region of interest
RT	Repetition time
SISS	Sub-acute ischemic stroke lesions
SVM	Support Vector Machine
T1ce	Contrast-enhanced T1-weighted
TC	Tumour core
TN	True negative
TP	True positive
VSD	Virtual skeleton database
WHO	World Health Organisation
WM	White matter
WT	Whole tumour

Chapter 1

Introduction

1.1 Problem Definition

Every year, about 16,000 people in the UK are diagnosed with a brain tumour and over 60,000 people are currently living with a brain tumour. According NHS, the incident count of brain tumours in the UK has been increased and it is a serious issue (Brain Tumour Research 2019). Up to 30% of all brain and central nervous system tumours are gliomas, of which about 80% are malignant (Goodenberger and Jenkins 2012). This finding illustrates the value that a well-considered remedy for this type of tumour would have. However, despite the large number of brain tumours worldwide, primary brain tumours are relatively rare. Primary tumours start within the brain and central nervous system and rarely spread to the rest of the body. Most brain tumours, however, are metastatic brain tumours that originated in another part of the body and spread to the brain via the bloodstream or the lymphatic vessels (Paolillo and Schinelli 2015). Most primary brain tumours originate from glial cells (termed 'glioma') and are classified by their histopathological appearance using the World Health Organisation (WHO) division into low-grade glioma (LGG) and high-grade glioma (HGG).

The treatment of gliomas combines surgery, radiation therapy and chemotherapy. The successful treatment of a tumour depends on its location, cell type and the grade of the tumour. Therefore, the segmentation of a tumour is critical for planning surgery and other forms of treatment. Medical imaging modalities are used for detecting and assessing tumours. Of the many different clinical diagnosis, choosing the best treatment in support of surgery and for planning radiotherapy (Fink et al. 2015). Conventional MR images (C-MRI) can be useful when define the target volumes are sought for planning the radiotherapy of high-grade gliomas (Niyazi et al. 2016). The 3D slice representation of MRI has advantages which are facilitating the ability of radiologist to visualize 3D anatomy from cross sectional images through integrating spatial information over a series of cross-sectional images and it is useful in clinical practice by reducing error (Wu et al. 2010). Tumour assessment requires the full-3D volume of the tumour to be accurately measured, which is achieved by manually drawing around the target region. However, manual segmentation around the tumour margins on a slice-by-slice basis is time-consuming and can take 16 minutes or more per tumour; semi-automatic methods take less than 2 minutes (Odland et al. 2015). Furthermore, human detection of the visible features of the image is limited, which increases the risk of

human error in manual segmentation. Therefore, some kind of automated segmentation will always be helpful, especially for large MRI datasets.

1.2 Motivations

Computer-aided procedures currently play an important role in medical image analysis. The segmentation of various tissues or organs is critical to medical decision-making, such as the assessment of risk and disease classification. The segmentation result provides target separation, diagnosis, quantitative measurements and treatment planning. With brain tumours, accurate segmentation may aid diagnosis and treatment planning via a fast and objective measurement of tumour volume. Many segmentation methods have been developed for brain tumour segmentation and are reviewed in Chapter 3. However, despite the effort that has so far been devoted to the segmentation problem, brain tumour segmentation is still a matter for research.

The classification approach, using the convolutional neural network (CNN), is under hot debate at present. Some of the CNN-based approaches have been adopted for the task of segmenting brain tumours in medical images, especially in MRI data. Studies describing it have registered the best performance in brain tumour segmentation. Therefore, the CIFAR network was suggested for the first part of our study because it performs the task of classification well (Krizhevsky 2009). However, using the pooling layers in the CIFAR architecture can cause down-sampling in the data, which loses some of the image information that is useful for learning. In addition, the brain tumour image, the centre pixel of a patch of 32×32 pixels, does not have enough dependencies to acquire a label from this patch, which includes a great deal of overlapping tissue information. Consequently, hand-crafted features may be combined with the CIFAR machine-learned features to compensate for the lost information by providing features that correlate closely with neighbouring pixels and makes the classification more accurate.

The CNN architecture is then modified in several ways in fully convolutional networks (FCN). Specifically, instead of CNN making probability distribution predictions patch-wise, FCN models predict a single probability distribution pixel-wise. To further improve the brain tumour segmentation, in our second and third approaches we used

SegNet. It is a deep fully convolutional neural network architecture that has great advantages for semantic pixel-wise segmentation (Badrinarayanan et al. 2017).

Most of the existing studies on brain tumour segmentation are performed using MRI modalities, which are stacked together as different input channels into deep learning models. However, the correlation between the various MRI modalities has not been explicitly considered. Consequently, a feature fusion method is proposed to select the most effective information from these modalities. In addition, a model is proposed to deal with multiple MRI modalities separately, while their spatial and sequential features are incorporated for 3D brain tumour segmentation.

The greatest challenge in the field of brain tumour segmentation is to develop an efficient way of accurately separate from one another the sub-tumour structures, which are characterized by complexity, less regularity (especially in the number of classes) and the varying appearance of their texture and shape. Using only a method based on deep learning is insufficient for accurately mapping a brain tumour in its region. It falls short because the SegNet based approach does not sufficiently consider the local features related to changes of tissue texture due to the growth of the tumour. Still, considering only the region of interest (ROI) (which represents only the extensions of the complete tumour structure) as input image data and suppressing the intensity of other irrelevant areas helps to reduce the computational complexity of the model, due to the reduced amount of data and the smaller size of the features. In that case, combining SegNet machine-learned features and the hand-crafted features from the ROI, which form part of our third approach, will help to encode global information and local dependencies into feature vectors that are smaller, require less computational time and offer more accurate tumour segmentation.

1.3 Aim and Objectives

The aim of this thesis is to develop an automatic image processing technique to accurately segment the brain tumour and sub-tumour tissue from multimodal MR images.

To achieve this aim entails the following objectives:

- Explore new feature representations that integrate hand-crafted features (which consider local dependencies) with machine-learned features (which provide global information) for the accurate segmentation of brain tumours.
- Investigate the effective combination of features extracted from multi-modal MR images, while maximising the useful information from certain modalities of MR images.
- Develop an automated method to generate an ROI segment that agrees with expert's delineation across all grades of glioma using a single, commonly used MRI protocol.
- Evaluate the developed algorithms by conducting experiments on two datasets: first, a clinical dataset, which was acquired from Guilin NanXishan Hospital, Guangxi, China; and second, a publicly available dataset from the Multimodal Brain Tumour Image Segmentation Benchmark (BRATS2017).
- Adapt and validate the proposed algorithms to detect another brain injury (i.e. an ischemic stroke lesion: ISLES) from normal brain tissues.

1.4 Structure of the Thesis

A brief description of the structure of this thesis follows:

Chapter 1: This chapter highlights the motivation, aim and objectives of the research, and outlines the structure of this thesis.

Chapter 2: This chapter provides a brief introduction to the clinical background of brain tumour segmentation in MRI images, including the MRI acquisition technique (which is common for brain tumour clinical tasks) and the various MRI modalities. In addition, a very brief description of the ischemic stroke lesion task will be given. The datasets that are used for evaluation will then be described.

Chapter 3: This chapter reviews the literature on the methods of brain tumour segmentation using MRI modalities. It also briefly reviews the methods of ISLES segmentation in MRI. In addition, this chapter reviews some of the commonly used methods of evaluation.

Chapter 4: This chapter discusses the first contribution of this thesis to brain tissue segmentation. An intensity-adding histogram model of a texture descriptor is generated, which is calculated according to a clustering-based image thresholding method, using the distribution of similar intensities of brain tissue in the three MRI modalities to encode the local correlation with nearby pixels into feature representation. Then a classification-based method is proposed based on a combination of machine learned features and hand-crafted features for the accurate segmentation of a brain tumour.

Chapter 5: This chapter describes the next step in brain tumour segmentation, which is based on maximum features joint modelling. This is achieved by using 3D data information from the neighbours of a single slice in the data to increase the accuracy of segmentation in the modality of an MR image and the effective combination of features extracted from multi-modal MR images, while maximizing the useful information from the various modalities of these MR images.

Chapter 6: This chapter takes a step towards a more accurate brain tumour segmentation method. It proposes an automated method that uses single MRI modality (FLAIR) to generate ROI images. The extracted hand-crafted texture features (GLCM) are then combined with the machine learned-based features (score maps of SegNet) for the corresponding pixels in the ROI. Moreover, to improve the accuracy, a voting fusion method is proposed which is based on the connection between a 2-label mask (background, oedema) and a 3-label mask (background, necrosis and enhanced).

Chapter 7: This chapter assesses the robustness of the three methods proposed in this thesis using a practical clinical dataset of a brain tumour. It also demonstrates the ability of the proposed methods to segment injured brain tissue in another case, that of a stroke lesion. It does so by modifying and evaluating the three proposed methods, using public and clinical datasets of ischemic stroke lesion.

Chapter 8: This chapter summarises the main conclusions obtained in this research. It also makes suggestions for further study.

Chapter 2

Clinical Background

2.1 Introduction

Medical imaging techniques and processes are used to acquire images of different parts of the human body for diagnostic and treatment purposes within digital health. MRI is a technique that provides detailed images of the inside of the body, including the brain's soft tissues and spinal cord, at any plane. It is primarily used to visualize the structure and function of the body (Pedapati and Tannedi 2018).

The human brain is one of the most important organs of the body because it coordinates every action of the human body. Many diseases can affect the brain, such as infections, strokes, and tumours. Furthermore, a brain tumour might be a cancerous or non-cancerous mass or growth of abnormal cells in the brain. MRI is the most important technique to detect a brain tumour. Recently, medical image analysis of MRI scans has come to attention because of the need for an efficient and objective evaluation of large amounts of data (Bauer et al. 2013). The detection of brain tumours and automatic brain tissue classification from MRI images are both very important in the medical community, and in clinical studies of the normal and diseased human brain. The most important stage in the medical imaging processes of an MRI image is the segmentation of the image, which divides the objects in the image and separates them for processing.

This chapter provides general background information related to brain tumours and the techniques that are used for the detection of brain tumours. This chapter also discusses the physical principles of MRI. The dataset acquired and used the conventional MRI is described. In addition, although the main objective of this thesis is to segment brain tumour, the methods developed in this thesis will be adopted to the other segmentation task of brain injury (ischemic stroke lesion) to present their ability to segment an image. A brief description of ischemic stroke lesion and dataset will also be given in this chapter.

2.2 Brain Tumours

The human brain is an organ that controls all the functions of the body, including intelligence, creativity, emotion, and memory. The brain is protected within the skull and is composed of the cerebrum, cerebellum, and brainstem. It is connected to the spinal cord by the brainstem (Mayfield Brain and Spine 1999).

The largest part of the brain is the cerebrum, which is composed of right and left hemispheres. It performs vital functions, such as interpreting touch, vision, and hearing, and produces speech, reasoning, emotions, learning, and the fine control of movement. The cerebellum, which is located under the cerebrum, controls muscle movements and maintains posture, and balance. The brainstem—which consists of the midbrain, pons, and medulla—works as a relay centre to connect the cerebrum and cerebellum to the spinal cord (Mayfield Brain and Spine 1999). The cerebrum surface tissue is called the cerebral cortex; it is the most superficial layer of the cerebrum. The cerebral cortex is grey and folded, and contains about 70% of the brain's 100 billion nerve cells (Mayfield Brain and Spine 1999; Miller et al. 2010). In addition, the brain has long connecting nerve fibres called axons between the neurons and beneath the cortex, which form the white matter (Miller et al. 2010). The centre of the brain consists of four connected hollow spaces, called ventricles. These ventricles contain a liquid called cerebrospinal fluid (CSF), which circulates throughout the central nervous system (CNS) (Wallace and Wallace 1973). Within the brain, the most featured and detectable parts in the images are Grey Matter (GM), White Matter (WM) and Cerebrospinal Fluid (CSF).

A brain tumour is a mass of abnormal cells that grows inside or around the brain and multiplies uncontrollably. These cells can be differentiated from the surrounding tissue by their structure (Wallace and Wallace 1973; The Brain Tumour Charity 2000; Gardner 2018; Win and Urvey 2014). Brain tumours originate in the brain and rarely spread to other sections of the body. However, secondary or metastatic brain tumours are produced from cancer cells in another part of the body that pass to the brain through the bloodstream, in a process which is called metastasis (The Brain Tumour Charity 2000).

Tumours that start in the brain can be classified into four types: gliomas, meningioma, pituitary adenomas, and nerve sheath tumours. According to the World Health Organisation (WHO), tumours are graded from I, the least advanced. to IV, the most advanced, form of the disease, (Louis et al. 2007). In 2016, WHO presented a recent classification of tumours based on histologic and molecular criteria (Louis et al. 2016), which had been revised from the 4th edition (Louis et al. 2007).

2.2.1 Low-grade Glioma

Low-grade gliomas (LGG) are primary brain tumours that arise from the glial (supportive) cell in the brain or spinal cord. Gliomas of grades I and II are considered low-grade tumours, but this category of tumour underwent major restructuring by the WHO in 2016 (Louis et al 2016). Low grade gliomas may take years to grow, but usually develop into high grade gliomas over time. In 2007, the WHO classification of gliomas was based on histological subtype (i.e. they could be astrocytic, oligodendrocytic, or oligoastrocytic). The 2016 classification grouped astrocytic and oligodendroglial tumours together, and defined specific entities further on the basis of their IDH mutation and 1p/19q codeletion status (Stieber 2016).

LGG tumours possess a wide range of imaging features which define their histological categories. LGG can be seen as hyper-intense on T2-weighted images and may appear with diffuse indistinguishable boundaries or focal shapes with clear borders. A cyst may be seen in the image and they usually have little oedema. The appearance of LGG tumours can be enhanced by changing the image contrast. Figure 2-1 shows examples of LGG tumours in several MRI protocols.

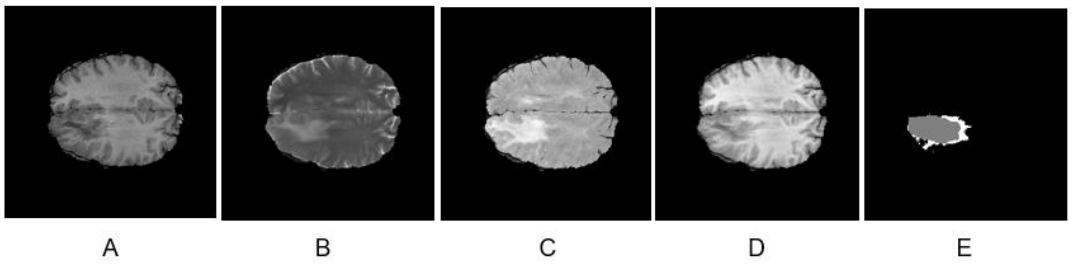

Figure 2-1: MRI images of low-grade gliomas: A) FLAIR, B) T1 weighted, C) T1-contrast, D) T2-weighted, E) ground truth.

2.2.2 High-grade Glioma

High-grade glioma is the most aggressive type of glial intra-axial tumour of the CNS. HGG also account for most malignant primary brain tumours and correspond to the WHO categories of grade III and grade IV. Glioblastomas (GBMs) account for about 60% to 70% of high-grade gliomas, anaplastic astrocytoma, and anaplastic oligodendrogliomas and anaplastic oligoastrocytoma account for the rest (Eftimov et al. 2007). The prognosis for patients diagnosed with HGG is still poor. In the MRI images, the HGG can be seen as a heterogeneous mass with a surrounding oedema. There is often a necrosis in the central region with an extensive oedema (see Figure 2-2). Advanced MRI techniques, such as diffusion weighted imaging (DWI), diffusion tensor imaging (DTI), and conventional MRI are used for the clinical HGG purposes.

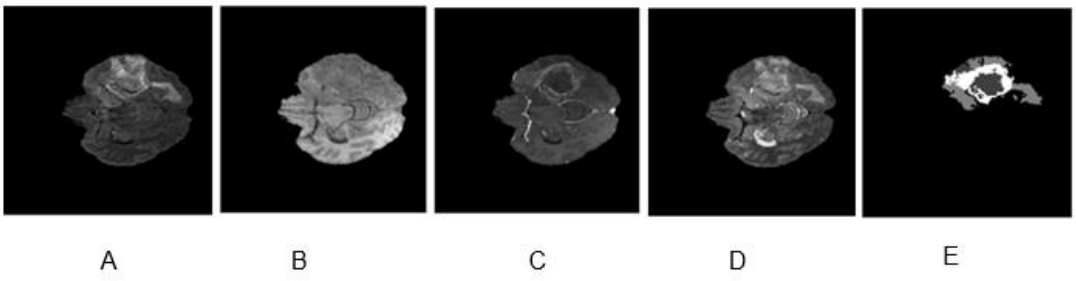

Figure 2-2: MRI images of high-grade glioma: A) FLAIR, B) T1 weighted, C) T1-contrast, D) T2-weighted, E) ground truth.

2.3 Medical Imaging Techniques

It can be seen that medical imaging plays an important role in the detection of brain tumours because it is non-invasive method, presents different texture features of different tissues and it does not need to surgery. Therefore, we cannot detect the brain tumour without medical imaging. The two most common and most often used medical imaging modalities are computed tomography (CT) and MRI. These two modalities play an important role and have a significant effect on patient care. The advantage of using contrast material in the imaging of brain tumours is that it improves the detection and the evaluation of brain neoplasms (Drevelegas 2011).

To diagnose a brain tumour, the following modalities may be used:

(1) MRI of the head: this provides detailed images that can detect brain abnormalities such as tumours and infections. This technique has high sensitivity in detecting tumours and evaluating the surrounding area to define their extent.

(2) Spinal MRI: this provides images of the anatomy of the vertebrae, spinal cord and the spaces between the vertebrae through which nerves pass. It can be used to detect tumours that grow in, or spread to, the spine and spinal cord or the cerebrospinal fluid around it.

(3) Brain fMRI or functional MRI: this is used to measure the tiny metabolic changes that occur in an active part of the brain. The scan is used to assess areas in the brain related to language and muscle movement. It is also used to monitor the growth and function of tumours, and to evaluate the potential risks of surgery or other invasive treatments.

(4) CT of the head: this can detect brain tumours and help plan the use of radiation therapy. CT can also reveal bleeding or swelling in the brain.

(5) PET and PET/CT of the head: a positron emission tomography (PET) scan is a diagnostic test that uses a small amount of radioactive material as a tracer to diagnose and detect the severity of a variety of diseases. A PET/CT combined exam provides images from a PET and CT scan together to detect both the anatomy (from the CT scan) and function (from the PET scan) of the brain. This test depends on the measurement of the brain tumour's use of glucose.

(6) Cerebral angiography: this is an invasive test that uses x-rays and an iodine-containing contrast material to produce images of the blood vessels in the brain. It can provide more information on the abnormalities displayed in an MRI or CT of the head.

(7) Myelography: this uses a real-time form of x-ray (called fluoroscopy) to assess tumours, including those of the bony spine, meninges, nerve roots or spinal cord. It is used in addition to MRI or when MR imaging cannot be used.

(8) Biopsy: this is the removal of tissue to test it for disease. It requires an imaging guide (e.g. an X-ray, CT, or MRI) to locate the precise place and perform the biopsy. In addition, lumbar punctures and neurological exams may be performed to diagnose a brain tumour (Gardner 2018).

Conventionally, the main diagnostic tool for central nervous system diseases is MR. However, CT is still a superior modality for the imaging of brain tumours, and it is used to detect calcification and haemorrhage, as well as evaluate any bone changes related to a tumour. CT is the most commonly used diagnostic technique for patients who live with metallic devices or who are critically ill, paediatric or unstable (Eftimov et al. 2007).

The imaging modality used in this project is conventional MRI scanning and uses several datasets that were acquired by means of MRI. The next section presents more detailed information about the physics of MRI and how it works.

2.3.1 Magnetic Resonance Imaging

Magnetic Resonance Imaging (MRI) is a modern clinical imaging technique that is used to detect and visualise the details in the internal structure of the body (Azhari et al. 2014; Hassan and Aboshgifa 2015). This technique exploits the fundamental principles of Nuclear Magnetic Resonance (NMR), which has been investigated since the early twentieth century. MRI does not use X-rays; instead it uses a powerful magnet and sends radio waves through the body. The images can then appear on a computer screen or on film. MRI has much greater contrast than CT, making it especially useful for neurological diseases. The main advantages of MRI over other medical imaging techniques are its non-invasive nature, versatility, excellent tissue contrast, and sensitivity to flow and diffusion.

MRI works on atomic nuclei and their property of magnetization. A uniform external and powerful magnetic field is applied to the tissue to be tested. This process of alignment is known as magnetization and is carried out to align the protons of the water nuclei in the tissues. These protons are oriented randomly within the nuclei. The magnetization becomes unstable because of external radio frequency (RF) energy. The nuclei return to their resting alignment through various relaxation processes and RF energy is emitted as a result. After a time, the emitted signals are measured. The signals from each imaged plane site consist of frequency information, which is converted to its corresponding intensity levels by the implementation of a Fourier transform. Afterwards, they show up in shades of grey on a matrix of pixels. Several different types of image can be created by varying the sequence of the RF pulses applied and collected.

2.3.1.1 Physical Principles of MRI

MRI uses the quantum mechanical properties of subatomic particles, such as the proton, which has a quantized angular momentum called spin. The hydrogen atoms that around found in water and fatty tissues have only one proton. Given that most of the human body consists of water and fat, this property can be used to detect the amount of hydrogen in medical applications. This spin generates a net nonzero spin when exposed to an external magnetic field and acquires a magnetic moment. It then aligns itself to an external field.

In the absence of a magnetic field, the magnetic moment of the hydrogen is oriented in random directions and the net magnetic field will be zero. If an external magnetic field of B_0 is applied, the nuclei will align along the flux lines of the field. Subsequently, a secondary spin will be added to its normal spin as it wobbles through its magnetic moment around B_0. This secondary spin is called "precession" and it forces the magnetic moments to take a circular precessional path at the precessional frequency speed, which is called the Larmor frequency.

2.3.1.2 Magnetic Resonance

Resonance is the basis for all MR procedures; it occurs when applying a radio frequency (RF) pulse at the same energy as the processing hydrogen nuclei at an angle of 90 degrees to the magnetic field B_0. Resonance is essential to the absorption and emission of energy by many objects and devices. As a result of applying an external magnetic field, the number of spin-up and spin-down nuclei are equal. The net magnetisation vector (NMV) will then lie at 90° to the transverse (X-Y) plane, which is known as the "flip angle". Pulses with 90° and 180° flip angles are the most common but smaller flip angle pulses are also used in some imaging methods, such as gradient echo imaging. The hydrogen nuclei absorb energy from the RF pulse, which increases the number of high energy (spin-down) nuclei. The magnitude of the flip angle depends on the magnitude and duration of the RF pulse. As the magnetic field B0 increases, the required energy to generate the resonance also increases. Figure 2-3 shows a schematic representation of NMV before and after applying an RF pulse to MR active nuclei. Phase coherence occurs at resonance when the magnetic moment of hydrogen is aligned in the same position of the processional path around the magnetic field B_o. This results

in a superimposed magnetic vector called transverse magnetisation (Jr 2000) within the X-Y plane, as shown in Figure 2-4.

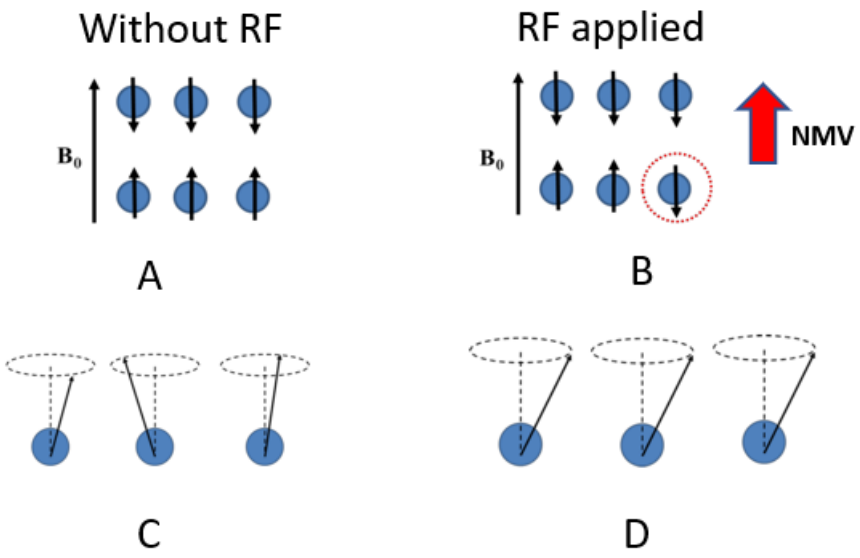

Figure 2-3: The effect of applying an RF pulse when the nuclei are exposed to the external magnetic field. NMV is related to the spin-up and spin-down nuclei: (A) without the application of a RF pulse; (B) when a RF pulse is applied, the number of spin-down (high energy) nuclei increases and this results in an NMV. Phase coherence (C) is out of phase or incoherent in the absence of an RF pulse. (D) shows phase coherence in-phase or coherent when the RF pulse is applied at Larmor frequency.

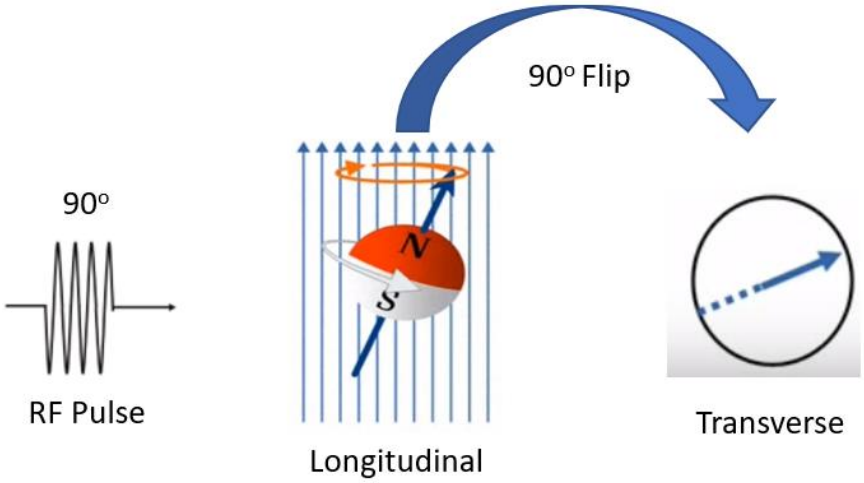

Figure 2-4: Excitation of a magnetic nucleus by applying a pulse of RF energy.

The MR signal is generated by applying a strong and constant magnetic field to a sample or target tissue. The magnitude of the signal depends on the amount of magnetisation in the transverse plane. The frequency of the signal is equal to that of the Larmor frequency. Once the RF pulse is terminated, the nuclear energy gained from this RF pulse will be lost; I this case, the NMV attempts to realign with the external magnetic field B_0. The magnetisation in the longitudinal plane (which has exponential properties) increases, in a phase known as the recovery. At the same time, the magnetisation in the transverse plane decreases exponentially, which is known as the decay phase. Consequently, the magnitude of the induced voltage within the receiver coil declines during the decay, in what is called a free induction (FID) signal.

2.3.1.3 Relaxation

Relaxation describes how signals change over time. In the relaxation phase, the hydrogen nuclei lose the excitation energy that was absorbed when RF was applied. This makes the NMV return to the initial B_o, making the magnetic moments of the hydrogen nuclei lose their coherency. The relaxation time of the hydrogen protons can vary, and it commonly measured twice: the longitudinal relaxation time, which is known as T1 recovery, and the transverse relaxation time, which is known as T2 decay. Figure 2-5 illustrates the process of relaxation.

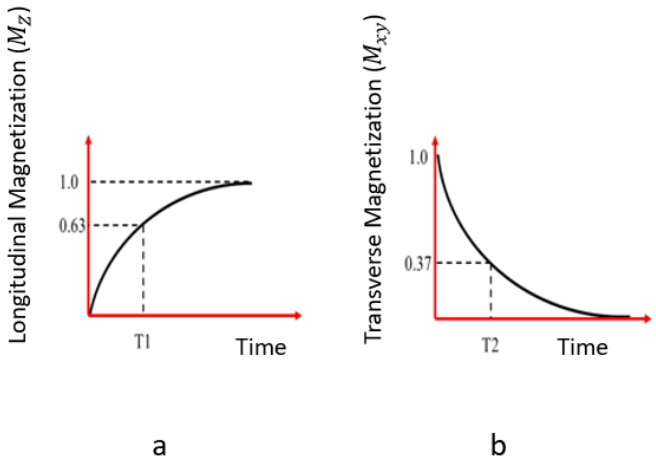

Figure 2-5: (a) T1 recovery curve, which represents exponentially increasing longitudinal magnetisation; (b) T2 decay curve, which represents the decay of magnetisation in the transverse plane (NMV) after switching off the RF pulse.

The process associated with T1 is responsible for the loss of signal intensity. This leads the magnetic moments of nuclei to recover their longitudinal magnetisation. T1 is related to the properties of the tissue and the magnetic field strength. The other process, which is associated with T2, is responsible for the broadening of the signal. T2 decay occurs when the nuclei transfer energy to the surrounding nuclei. In the process of decay a loss of magnetisation occurs in the transverse plane, which is also called spin-spin relaxation (Jr 2000). T2 depends on the tissue characteristics and the magnetic field strength and is usually 5 to 10 times faster than the T1 recovery time.

The intensity of the signal and the signal-to-noise ratio depends on the magnetic characteristics of the target tissue being imaged. The characteristics of the tissue, which may enhance the signal-to-noise relationship, are the high magnetic nuclei (proton) concentration, the short T1, and the long T2 for a particular set of imaging factors. The most important limitation in imaging nuclei other than the hydrogen nuclei is their low tissue concentration, which results in low signal intensity (Jr 2000; Bjornerud 2008).

In most imaging methods, repetition time (TR) and echo time (TE) are used to control contrast and signal intensity. These two parameters must be taken into consideration to select the factors for a specific imaging procedure. If a short TR is used to obtain a T1-weighted image, the longitudinal magnetisation has no opportunity to reach its maximum and produce high signal intensity. Moreover, if the TR is reduced to shorten the image acquisition time, then the limiting factor is image noise. In addition, when using long TE values, the transverse magnetization, and the resulting signal that it produces, can decay to very low values. This produces noisier images. Table 2-1 lists the T1 and T2 relaxation times for brain tissues at a magnetic field of 1 Tesla.

Table 2-1: T1 and T2 times for brain tissue at the magnetic field of 1 Tesla.

Tissue	T1 (ms)	T2 (ms)
Water	2500	2500
Grey matter	900	90
White matter	500	100
Fat	200	100
CFS	2000	300

2.3.1.4 Conventional MRI Protocols

The conventional MRI protocols (C-MRI) are generated based on the characteristics of tissue, and TE and TR. This section explains the details of C-MRI acquisition.

A- T1-weighted

A T1-weighted protocol is acquired when both TE and TR are short. The clinical significance of this is that tissues with short T1 values will appear bright in T1-weighted images. This protocol generally produces superior contrast between fluids, water-based tissues and fat-based tissues. For brain images, this protocol provides good contrast between GM and WM. Using a low TR value of about 500 ms, three types of tissue (i.e. CSF, brain tissue and fat) will be clearly separable. In a T1-weighted image, the CSF appears hypo-intense, while the brain tissues (GM and WM) can be seen with medium intensity, and fat has great hyper-intense values. Contrast agents can also be injected into the patients to help increase the specificity by providing more images with different levels of contrast.

B- Contrast-enhanced T1-weighted

T1-weighted image contrast (T1ce) can be enhanced using a contrast agent, which depends on substances with low molecular weight such as gadolinium (Gd). Contrast-enhancing agents for brain tumour imaging are effective because their molecules do not pass the blood vessel barriers inside the healthy brain tissues and they remain inside the vessels. In contrast, malignant primary brain tumours cause damage to the blood brain barriers and, therefore, the contrast agent comes out of the vessels and leaks into the tissue space. The influenced area will have shorter T1, which results in an appearance of outstanding hyper-intensity on the T1-weighted images (Bauer et al. 2013).

C- T2-weighted

A T2-weighted protocol is obtained when both TE and TR are long. This protocol provides a good distinction between the parts of the brain (i.e. GM, WM, CSF) and scalp fat for the T2 values of brain tissues (Roberts and Mikulis 2007). In the fluid areas of tissues with higher mobility, the spin interactions take place faster with slower loss

of transverse coherence, which leading to longer T2 time. Furthermore, for more constrained structures such as those with a dense population of cells, the spin interactions are longer with faster loss of transverse coherence, which leads to a shorter T2 time.

Usually, in T2-weighted images, fluids show up very intensely, while water- and fat-based tissues appear mid-grey. Tumours tend to damage the microstructures of the brain, which prolongs the T2 values of the affected tissue.

D- FLAIR

A fluid attenuated inversion recovery (FLAIR) image is obtained by applying an 180º RF pulse instead of a 90º pulse to increase the dynamic range of the T1-weighted images. An RF pulse of 180º will fully invert the longitudinal magnetisation of all the underlying tissue opposite B_0, and is therefore called an "inverting pulse". Thus, the magnetisation begins at a negative initial value and passes through the zero value.

The FLAIR protocol creates a T2-weighted image with a suppressed CSF signal, which makes FLAIR the most used protocol for diagnosing non-enhancing lesions in brain tumours. Figure 2-6 shows some C-MRI images of a brain tumour.

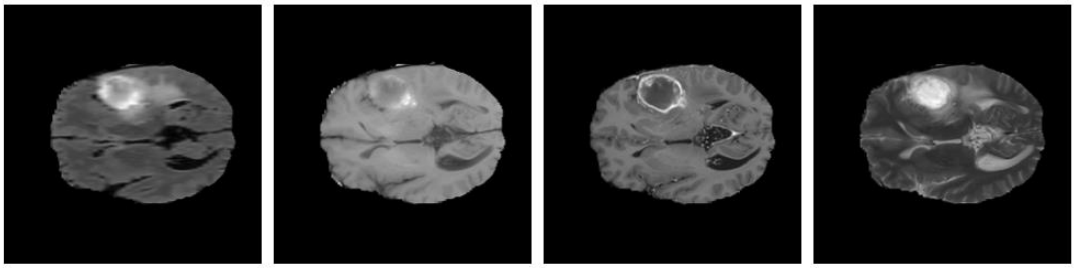

Figure 2-6: Examples of C-MRI images of a brain tumour: (left to right) FLAIR, T1-weighted, T1-contrast, T2- weighted.

2.3.2 Diffusion Magnetic Resonance

Diffusion imaging modalities are among the most important advanced MRI techniques in neuroradiology (Huisman, 2010). In this thesis they are investigated in a medical application study of stroke lesion, alongside conventional MR techniques. The next section defines the concept of diffusion and describes how MR images are generated by the diffusion of water molecules in the brain structures.

2.3.2.1 Diffusion Weighted Imaging

A diffusion-weighted imaging (DWI) MRI provides an image contrast unlike that provided by conventional MR techniques. In particular, DWI is sensitive to the detection of acute ischemic stroke and it can demarcate an acute stroke from other processes that appear with sudden neurological deficits (Kim et al. 2014).

DWI is a form of MRI that is based on measuring the random Brownian motion of water molecules within a voxel of tissue. In general, this means that the highly cellular tissues or those tissues with cellular swelling exhibit lower diffusion coefficients. The DWI technique based on water motion can be used indirectly to extract information about tissue organisation at the cellular level. This technique is particularly useful in tumour characterization and cerebral ischemia (Barucci et al. 2016)

In general, the signal intensity in DWI can be quantified by using a parameter known as the apparent diffusion coefficient (ADC); however, it should be emphasised that this is not the real diffusion coefficient, which is a measure of the average water molecular motion. Water molecule distribution diffusing over a certain period is considered to have a Gaussian form, with its width proportional to the ADC (Basser and Jones 2002).

The strength, direction, and temporal profile of the imaging gradient affect its sensitivity to diffusion, and they are commonly reduced to a single simplified parameter that is referred to as the *b* value. Images obtained at different b-values are subsequently used to compute a parametric map, which allows the water diffusion behaviour of the tissue to be quantified. In this context the corresponding echo attenuation in a voxel can be expressed as:

$$S(b) = S_o\, e^{-bADC} \qquad (2\text{-}1)$$

where S is the signal intensity (depending upon the apparent diffusion coefficient (ADC) and the b value is a parameter that is used in diffusion weighted imaging, which can be calculated as:

$$b = \gamma^2 G^2 \delta^2 \left(\nabla - \frac{\delta}{3} \right) \qquad (2\text{-}2)$$

where δ is the duration of one diffusion-encoding gradient lobe, ∇ is the time interval between the leading edges of the gradient lobes, G is the strength of the gradient, and γ is the gyromagnetic ratio.

The b values control the amplitude and the strength of the bipolar gradient coils, which are activated to detect the thermal motion of water in and about the cells (Brownian motion). Therefore, the ADC map can be superimposed on the standard anatomical images to obtain more information on the tissue under investigation.

Commonly, b values of between 500 or 1000 can produce the best balance of signal and tissue diffusion (Albers 1998; Hagmann et al. 2006; Kane et al. 2007) (see Figure 2-7).

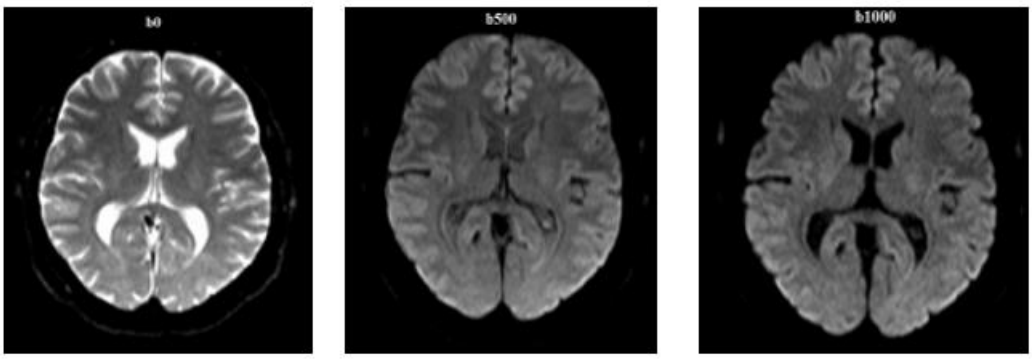

Figure 2-7: Example of DWI of different b value.

2.4 Ischemic Stroke Lesion (ISLES)

A stroke is unexpected interruption in the blood supply of the brain that lasts more than 24 hours. An acute stroke refers to the first 24-hour period of a stroke. Most strokes are caused by a sudden blockage, known as an ischemic stroke, in the major arteries to the brain. Other strokes are caused by a blood vessel that bursts and bleeds into brain tissue, known as haemorrhagic stroke. In general, a stroke is classified on the basis of its aetiology as either ischaemic (87%) or haemorrhagic (13%) (Wittenauer and Smith 2012; Subbanna et al. 2019). Ischemic cerebral infarction or ischaemic stroke accounts for approximately 60%–80% of all cerebrovascular events. This type of stroke is more common than haemorrhagic stroke and contributes to mortality and long-term disability worldwide (Kim et al. 2014; Chen et al. 2018). Haemorrhagic transformation (HT) is a serious complication and refers to secondary bleeding into the ischemic cerebral area after a stroke. Sometimes, a stroke occurs following an anticoagulant or thrombolytic therapy. A stroke can also be a consequence of ischemic injury to the brain's microvasculature. This complication occurs in 8.5%–30% of all patients with ischemic stroke. Severe HT can be lethal and may worsen a patient's condition (Paciaroni et al. 2008; Chen et al. 2018).

An ischemic stroke occurs when an artery to the brain is blocked. The blood carries oxygen and nutrients to the brain and takes away carbon dioxide and cellular waste. If an artery is blocked, then the brain cells (neurons) cannot make enough energy to function and will eventually stop working. The neurological symptoms and signs of an ischaemic stroke usually appear suddenly but may sometimes be progressive (stroke-in-progress). Symptoms and signs vary, depending on the location of the occlusion and the extent of the collateral flow. An atherosclerotic ischemic stroke is more common in the elderly, and occurs without warning in more than 80% of cases (Wittenauer and Smith 2012). An ischemic stroke can be caused by several different kinds of disease, such as narrowing of the arteries in the neck or head, which is most often caused by atherosclerosis or cholesterol deposition; blood clots in the heart, which can occur as an effect of irregular heartbeat, heart attack, or abnormalities of the heart valves; or other possible causes, including drug use, traumatic injury to the blood vessels of the neck, or disorders of blood clotting.

MRI is widely used to diagnose a cerebral ischemia. Conventionally, T1-weighted imaging (T1WI) and T2-weighted imaging (T2WI) do not adequately delineate the acute lesions in the early hours after an ischemic stroke. Moreover, they are not adequate for HT risk assessment. Meanwhile, diffusion-weighted imaging (DWI) is sensitive to the changes in the diffusion of the water molecules associated with cytotoxic oedema. The movement of the molecules in the ischemic areas of the brain is liable to be restricted (Wittenauer and Smith 2012; Kim et al. 2014; Barucci et al. 2016; Chen et al. 2018). The pathological mechanism of a stroke has been described in many studies, starting with the ischemic lesion topography on DWI. In particular, multiple lesions in the unilateral anterior circulation or small scattered lesions in one vascular territory have been reported to be related to large artery atherosclerosis (Kim et al. 2014).

2.5 Datasets

Two datasets are used in this study to develop the algorithms and establish an evaluation in their results. The first dataset is the brain tumour dataset. The second dataset is a set of images of patients who had an ischemic stroke lesion, which was used in this thesis to investigate the ability of the methods developed for detecting another brain injury.

2.5.1 Brain Tumour Dataset

2.5.1.1 Public Dataset

MICCAI BRATS 2017 is a publicly available dataset (Menze et al 2015; Bakas et al. 2017; Bakas et al. 2018; Bakas, S. et al. 2017). The version that was used in this study was provided by the Virtual Skeleton Database (VSD), which was released during the period of this study. Therefore, the BRATS 2017 dataset was considered as a benchmark to evaluate our proposed algorithms and make a fair comparison among them using the same dataset. The total patient dataset consists of 285 training (including 210 HGG and 75 LGG) MR scans of glioma. In each patient data, four MRI modalities are available, which are FLAIR, T1, T1ce and T2. The ground truths are provided with the training dataset by expert board-certified neuroradiologists (Menze et al. 2015). Data were acquired from multi-centres and using different scanners with a field strength of 3 Tesla. The provided data are distributed after their pre-processing (i.e. skull stripped). The

importance of skull removal in MRI brain image analysis was discussed in Zhuang et al. (2006), and Shanthi and Kumar (2007). The other pre-processing techniques that are implemented on the supplied data are co-registered to the same anatomical template and interpolated to the same resolution (1^3 *mm*).

2.5.1.2 Clinical Dataset

The clinical patient data was provided by Guilin NanXishan Hospital, Guangxi, China. There were two reasons for using this dataset: first, to cooperate with the hospital in the use of MRI images of patients with brain tumour glioma; and second, to further evaluate the algorithms that were used in this study. The types of dataset were conventional MRI protocols (FLAIR, T1, T1ce and T2), which were acquired from one scanner with a field strength 1.5 Tesla. The acquired dataset involved 29 patients, each with a glioma type of brain tumour. The dataset consisted of 8 LGG and 21 HGG tumours. The patients, 15 females and 14 males, at the time of scanning were between 24 and 78 years old. All of the data were acquired in the axial plane.

2.5.1.3 Ground Truth

Manual annotations called ground truths come with the MR images from the VSD system. The ground truth contains information about the location of the various tumour structures. Three types of intra-tumoral structures were defined as follows: oedema, necrosis, and enhanced tumour. These tumour structures were labelled by a trained team of radiologists and seven radiographers. The tumour structures were labelled on every third axial slice of MRI. More morphological operators (region growing) were used to interpolate the segmentation and the results were visually reviewed for the sake of additional manual corrections, if necessary (Menze et al. 2015).

The protocol for manual annotation of the tumour structures, for both low- and high-grade cases in BRATS challenge (see Figure 2-8) (Menze et al. 2015) was as follows:

1- Oedema was segmented from T2 and FLAIR images. T2 was used for the initial segmentation. Then FLAIR was used to check the extension of oedema and discriminate it from other tissues such as those with necrosis and ventricles.

2- The complete tumour core, which contained all three tumour structures, was segmented using the hyper-intense areas in T1ce with the heterogeneous area of hyper-intense and hypo-intense lesion in T1.

3- The enhanced core of the tumour was segmented using T1ce via thresholding on the complete tumour core region, which resulted in keeping the gadolinium and subtracting the necrosis tissue. The threshold levels were determined individually for each case by visual inspection.

4- Necrosis or fluid-filled core was defined using T1ce in the low-intensity structures inside the enhanced tumour. The same label was considered for the rare haemorrhages.

5- The non-enhanced core was considered to be the remaining part of the complete tumour core. Because they were not detected in lists 3 and 4, they were obtained by subtracting the corresponding areas from the complete tumour.

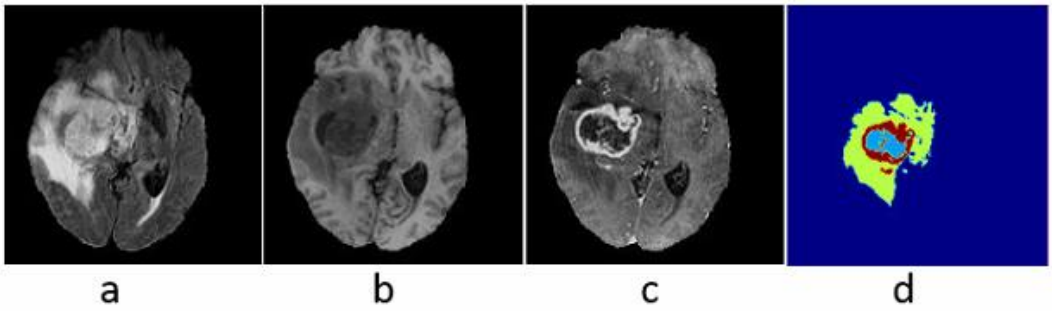

Figure 2-8: (a) Complete tumour visible in FLAIR; (b) tumour core visible in T2; (c) enhanced and necrotic tumour component structures visible in T1ce; (d) final labels of the observable tumour structures noticeable: oedema (yellow), necrotic/cystic core (light blue), enhanced core (red) (Alqazzaz et al. 2019).

The ground truths that came with the clinical dataset were labelled by a trained radiologist, using the protocol of the tumour structure outlines as they were labelled in the public dataset (see Figure 2-9).

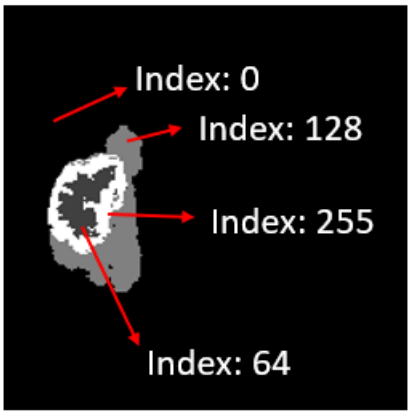

Figure 2-9: Ground truth image with all indices; index 255 represents enhanced tumour, index 128 represents oedema, index 64 represents necrosis, index o represents background.

2.5.2 Ischemic Stroke Lesion Dataset

2.5.2.1 Public Dataset

ISLES 2015 is a publicly available dataset (Maier et al. 2017), which was used in this study for stroke lesion segmentation. These data were collected from two centres of clinical routine acquisition using MRI with 3T. The total patient dataset consisted of 28 MR scans. Four MRI modalities were available, namely, DWI, FLAIR, T1 and T2. The ground truth was assembled manually by an experienced radiologist. The ISLES data were pre-processed in a consistent manner to allow for easy application of the method. Therefore, all the MRI sequences were skull-stripped, re-sampled to an isotropic spacing of $1^3 mm$ and then co-registered to the FLAIR modality.

2.5.2.2 Clinical Dataset

The clinical patient data were provided from the same hospital: Guilin NanXishan Hospital, Guangxi, China. The clinical dataset included 30 patient files, each file with DWI, FLAIR, and T2 MRI sequences. The dataset was acquired using one scanner with a field strength of 1.5 Tesla. All the ischemic stroke lesion images were in the axial plane.

2.5.2.3 Ground Truth

The lesions were visually classified as sub-acute ischemic stroke lesions (SISS) if a pathologic signal was found alongside in the FLAIR and DWI images (i.e. in the presence of vasogenic and cytotoxic oedema with an indication of swelling due to increased water content). Experienced raters are prepared for all the expert ground truths that are used in ISLES.

The annotation protocol and the corresponding GT labels of the region where ischemic stroke lesions were located are as follows (see Figure 2-10).

1- Healthy brain tissues and background.
2- Stroke lesion, whose boundaries are drawn using the FLAIR sequence, which is known to exhibit lower inter-rater differences.

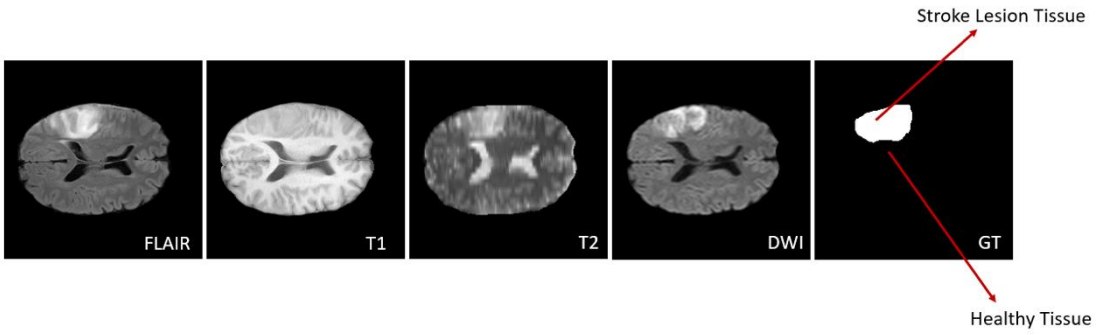

Figure 2-10: An example of an ischemic stroke lesion in different MRI sequences.

2.6 Conclusion

This chapter surveyed the clinical background for brain tumours. The application of MR protocols in a brain tumour was also reviewed. The C-MRI acquisition techniques were discussed and advanced MRI modality was given. A very brief description of ischemic stroke lesion was provided. The clinical and publicly available datasets that were used in this project were also described.

Chapter 3

Review of the literature and the approaches taken to segmentation in cases of brain tumour and brain lesion

3.1 Introduction

This chapter reviews first the literature and next the techniques related to the task in hand. In particular, this chapter discusses brain tumour segmentation in MRI images. The automatic methods previously proposed to segment brain tumours in MRI images are surveyed and discussed in some detail. In addition, this chapter discusses the protocols that are used to evaluate the procedure for validating the results of segmenting MRI images and related works on the segmentation of ischemic stroke lesions.

3.2 Segmenting a Brain Tumour

Many approaches have been used for brain tumour segmentation in MRI images. This is a challenging task because of the complex nature of the tumour and the inherent characteristics of MR imaging. The structure of a brain tumour presents various textures with irregular boundaries, which are unclear and discontinuous due to infiltration. Regarding the characteristics of the MR image, aspects which are hard to determine, such as the contrast agent dosage and the acquisition time, make segmentation a challenging task because they can affect the appearance of the tumour in the image and show the same tissue with a different intensity.

In the literature, many methods have been proposed for delineating a brain tumour and sub-tumour regions. These methods can be divided into automatic and semi-automatic, according to the categories suggested by Bauer et al. (2013). Other authors have suggested that the segmentation techniques can be grouped as generative or discriminative in their methods (Menze et al. 2015).

In general, image segmentation can be divided into three types based on the degree of human interaction entailed, be it manual segmentation, semi-automatic segmentation or fully automatic segmentation (Zhao and Xie 2013; Chitradevi and Sadasivam 2016; Fasihi and Mikhael 2016).

Although imaged objects can be manually divided into sub-regions, it is time-consuming to do this, expensive and prone to operator bias; hence, it is not reproducible. In semi-automatic segmentation methods, minimum human involvement is needed to initialise the method or to correct segmentation results manually at some stage (Fasihi and Mikhael 2016). In fully automatic methods, robust techniques require only that

prior human knowledge (e.g. of the location, size, or shape of the tumour) is incorporated into the algorithms (Fasihi and Mikhael 2016).

In the case of manual segmentation of the brain tumour, marking the tumour regions slice by slice is sometimes limited by the human viewpoint. The semi-automatic methods employ computers and human expertise, and the results then depend as much on the strategy as on computation. Fully automatic segmentation methods using MRI can resolve these issues by providing an efficient tool for reliable diagnosis and prognosis of brain tumours, which can quickly process large numbers of images. Therefore, many researchers have chosen automated brain tumour segmentation from MRI images.

The automatic segmentation techniques may be classified into three types based on the use of the learning method, as follows: supervised, semi-supervised, and unsupervised segmentation. Supervised segmentation needs user interaction throughout the segmentation process, whereas the unsupervised methods generally require operator participation only after the segmentation stage is completed. Labelling all the training data in supervised segmentation requires expert knowledge and is also time-consuming. In semi-supervised algorithms, a small number of training data are labelled correctly and the rest are unlabelled (Fasihi and Mikhael 2016). Unsupervised methods do not depend on a labelled training set at all.

Unsupervised segmentation techniques use image-based features such as intensities and/or textures. These approaches can handle more complicated cases. For example, unsupervised segmentation produced an accurate segmentation of all the regions present in a heterogeneous tumour. When a brain tumour is segmented, the lack of shape or intensity in the tumour makes unsupervised segmentation difficult. Consequently, few attempts have been made to devise techniques for unsupervised brain tumour segmentation in MR images that do not use an anatomic objective measure (Jalab and Alwaeli 2019).

A brief review of different segmentations for detecting a brain tumour from the MRI of a brain is to be found in Angelini et al. (2007), Roy et al. (2013), Bauer et al. (2013), and Zhao and Xie (2013).

Segmentation methods may be divided into four major classes, as follows: (1) threshold-based techniques, (2) region-based techniques, (3) pixel classification techniques and

(4) model-based techniques (Kotsiantis 2007; Gordillo et al. 2013; Patil and Deore 2013; Roy et al. 2013; Fasihi and Mikhael 2016).

In this study, the brain tumour segmentation approaches are divisible into two main categories: image classification-based approach and the image semantic segmentation-based approach.

3.3 Image Object Classification-based Techniques

This method classifies the image objects into groups based on some similarity in measurement. The classifier is an algorithm that uses a set of features which describe the objects; it employs the features to determine the class of each object (Kaur and Kaur 2015).

In supervised classification, the classes that an object may belong to are determined by experts, who provide a set of sample objects whose classes are known. This set of known objects is known as a training set because it is employed by the classification algorithm to learn how to classify objects. In unsupervised classification methods, there is no need to use training sets or pre-determined classes (Kaur and Kaur, 2015).

Classification starts by training the algorithm on the training dataset. The extracted model is then validated against a labelled test dataset to measure the model performance and accuracy. This type of classification can be used in different applications, such as document classification, image classification, fraud detection, churn analysis, risk analysis, and etc. (Singh 2016).

In general, the classification techniques require the following steps: (1) creating a training set; (2) selecting powerful features; (3) training the classifiers; and (4) assessing classifier accuracy (Kotsiantis 2007).

In the first step, a dataset with known labels is collected. In medical imaging, image labelling is often visually obvious and can be done after examination by an experienced operator (Pham et al. 2000). Then the data preparation and data pre-processing steps follow. Pre-processing algorithms can be used for issues such as missing values, discretisation, and noise removal. The third step uses feature selection to identify and remove irrelevant and redundant features. This improves the speed of the algorithms and enhances their performance. The critical step is selecting the learning algorithm. The final step is evaluation. In this context, there are at least three techniques for

calculating classifier accuracy, which are all based on splitting the data into training and testing sets. The difference between these techniques reflects how these two datasets are divided from each other.

The most common approaches to brain tumour segmentation emerge in the supervised techniques, which depend on a labelled training dataset (Juan-Albarracín et al. 2015). The size and quality of labelling in the dataset, a time-consuming task, directly determines the accuracy of the method.

In the testing stage, the testing dataset, which is also called the "unlabelled dataset", is fed to the trained model. The MR image voxels are then assigned to one of the classes. The detection methodology has to be highly accurate because its results are extremely important for planning the treatment of brain tumours.

The output of an image classification-based model is a discrete probability distribution. The model is trained to recognise the characteristics of each class. Some of image classification-based models are trained on hand-crafted designed features, while other classification-based models use high-level features that are generated automatically.

In the next section, hand-crafted feature methods and deep learning feature methods are described.

3.3.1 Hand-crafted Feature Methods

Many automatic tumour segmentation methods have been proposed in the last decade. Most automatic brain tumour approaches use the hand-crafted features method, as follows: features such as local histograms, Gabor and region shape difference are first extracted; they are then given to the classifier, such as a support vector machine (SVM) or a Random-decision Forest (RF), whose training procedure does not affect the nature of these features (Osman 2017; Donahue et al. 2014; Havaei et al. 2017).

Hand-crafted feature segmentation methods are based on extracting features from the images and creating models based on the relationship between the image features and the pixel/voxel classes (Roy et al. 2013).

In the pipeline in classical machine learning, the features are first extracted, and then given to the selected classifier. The classifier is trained to separate healthy from non-healthy tissues, as long as the input features have sufficiently high discriminative power.

These features may include the intensity values of raw input pixels, histograms, and the texture of images. A linear kernel has been shown to provide the best performance in many applications; it also requires only one parameter to be tuned (Walker 2010).

Classical discriminative classifiers techniques such as SVM and RF rely on hand crafted features (Havaei et al. 2017; Osman 2017). SVM is a classical discriminative learning technique that uses powerful data classification algorithms, which are very high accurate (Hsu et al. 2003; Singh 2016). SVMs belong to the general category of kernel methods which employ an algorithm that depends on the data from dot-products (Kotsiantis 2007; Orrù et al. 2012; Harefa and Pratiwi 2016).

The SVM model has been used for the accurate automatic segmentation of glioma brain tumours in multimodal MRIs and for predicting patients' survival (Osman 2017). In the present research, image intensity features were extracted for the purpose of segmentation, with pre-and post-processing of the MRIs.

Ruan et al. (2007) apply an SVM classifier for a limited number of MRI modalities in brain tumour segmentation. Their method can detect the whole tumour region without segmenting the tissue subtypes.

One limitation of the hand-crafted features is that they often require a large number of features to be computed, which makes computing slow and expensive in terms of memory (Havaei et al. 2017).

3.3.1.1 Decision Trees

A decision tree is a hierarchical tree structure that is used to classify classes based on a series of questions (or rules) about the attributes of the class. A decision tree is assembled by recursively splitting the feature space of the training set. The objective is to find a set of decision rules that naturally partition the feature space to provide an informative and robust hierarchical classification model (Myles et al. 2004). A decision tree can be used for both classification and regression tasks and is so named because it is a model that can be presented as a tree-like graph. In a decision tree, the training is performed by adjusting the parameters of a split function at every tree node through splitting the training data by exploiting the information gain. In testing, the feature vector of the testing data is applied to the tree at each node until a leaf node is formed.

Algorithms have been successfully applied in brain tumour segmentation. This technique is now commonly used due to its natural capacity to handle multiclass problems, as well as large feature vectors (Pereira et al. 2016). The algorithm is a supervised method that was developed for brain tumour segmentation by Zikic et al.(2012), who introduce an algorithm based on context-aware spatial features. In this step, the probabilities obtained by tissue-specific Gaussian mixture models are used as an additional input to train decision tree classifiers.

Goetz et al. (2015) propose a similar algorithm but theirs uses an extremely randomized tree classifier, which introduces more randomness during the phase of training to leverage the variety of the features in splitting the trees.

Meier et al. (2013) introduce a fully automated method for brain tumour segmentation in which a variety of different feature types is employed to capture the information for a decision forest classifier, which is followed by conditional random field as a spatial regularisation.

The conditional random field was introduced by Bauer et al. (2013a); it is an energy minimisation procedure and is integrated with RF. The energy contains the sum of singleton potentials and pairwise potentials, while the RF output is used to control the spatial regularisation of the conditional random field. In this approach, the feature is extracted from fix-sized local patches of HGG and LGG image datasets. Bauer et al. (2013a) compare their approach to previous work of theirs, in which instead of RF they use SVM as a classifier.

The decision tree-SVM cascaded classification approach is proposed by Amiri et al. (2016). The SVM stage in this is used to refine the final segmentation result. Although this method demonstrates results in brain tumour segmentation that are comparable to those from other RF based approaches, the results do not outperform other methods based on machine learning.

RF classification was performed for the task of brain tumour segmentation, and the RF classifier was selected for a proposed classification pipeline by Rehman et al. (2019), due to its better qualitative performance and significantly better quantitative performance than SVM and AD classifiers could offer.

3.3.2 Deep Learning Feature Methods

Deep learning techniques have been widely used for learning task-adaptive features in image segmentation applications, including brain tumour segmentation. However, most existing brain tumour segmentation methods based on deep learning are unable to ensure the appearance and spatial consistency of the segmentation results (Zheng et al. 2015; Zhao et al. 2018). One of the problems with deep learning is the limited capacity of its techniques to delineate visual objects (Zheng et al. 2015).

The deep learning method is an alternative for designing task-adapted feature representations that learn a hierarchy of increasingly complex features directly from in-domain data (Havaei et al. 2017; Zhao et al. 2018). Features based on deep learning often outperform those that are based on hand engineering designs (Lai 2015).

Brain tumour segmentation approaches apply the deep learning method to learn hierarchy features that combine information across MRI modalities (Havaei et al. 2017; Garcia-Garcia 2017; Pereira et al. 2016; Zhao et al. 2018).

3.3.2.1 Deep Convolutional Neural Network Layers

Convolutional neural networks are supervised visual models that learn to finely discriminate features with different levels of complexity. CNNs are multilayer feed-forward structures that are successfully applied in many visual applications, such as detection, recognition and segmentation tasks (Alvarez et al. 2012). Commonly CNNs are formed of one to three stages or levels. Each level consists of a convolutional filter bank layer, a non-linear transform layer and a spatial feature layer (or down-sampling).

In the training process (learning), local features are extracted from the input image and combined in sequenced layers to obtain a higher order architecture. Hence, the training process consists of learning the kernels and connection weights for each layer to infer the label instances in the training set. The output of this process is a set of filters banks (kernels), which are combined and tuned for the task in hand.

CNN-based methods perform better than conventional classification methods and have recently been able to learn hierarchical features. CNNs are composed of many blocks stacked on top of each other to form a hierarchy of features and are used in designing a deep neural network. These blocks are formed of the following main layers:

convolutional (CONV) and non-linear activation function (ReLU) layers, followed by pooling layers (POOL). these blocks are repeated according to the chosen design, until the image reaches a certain size (Long et al. 2015). Finally, the last block is connected to the fully convolutional layers (FC) to produce the class label. The building of these blocks admits of several architectural selections. The following section briefly describes a set of CNN layers.

A- Convolutional Layer

A convolutional layer is the basic building block in constructing a CNN. It is formed of units that are connected to the local patches of the previous layers through a set of weights, which are named "filter kernels". The width and height of the kernels are hyper-parameters that must be recognised by the user. A convolutional layer output is created by convolving the output of the previous units with the kernel of the current layer. A good initialization of the weights is important in deep networks that have many convolutional layers and different paths through the network (Ronneberger et al. 2015). Feature maps result from each convolutional layer. Therefore, the output volume is created by concatenating all of these filter maps along the third dimension. The filter response dimension is decreased through the convolutional layers below the special dimensions of the input array.

B- Non-linear Activation Function

An element-wise non-linearity is applied to the result of the kernel convolution to obtain features that are non-linear transformations of the input. The rectified linear unit (ReLU) is the most popular nonlinear function, as noted by Pereira et al. (2016):

$$f(z) = \max(z, 0) \qquad (3\text{-}1)$$

ReLU can learn faster in networks with many layers, which makes it appropriate for use in deep learning processes.

C- Pooling Layer

To introduce invariance for the network with respect to the local changes of each feature level (e.g. intensity), it has been found useful to subsample feature maps, which are treated as a pooling layer, along with spatial dimensions in X and Y directions. The pooling layer reduces the result dimensionality and the parameter numbers in the network and makes the network invariant with respect to small changes in each level of feature (e.g. intensity or position) in the previous layers. However, some studies forecast that future CNNs will use fewer or no pooling layers (Springenberg et al. 2015). The most common pooling operation is Max-pooling, in which the maximum values within each feature map are taken. Figure 3-1 shows an example of the popular window of a max-pooling layer with stride 2 and filter size 2.

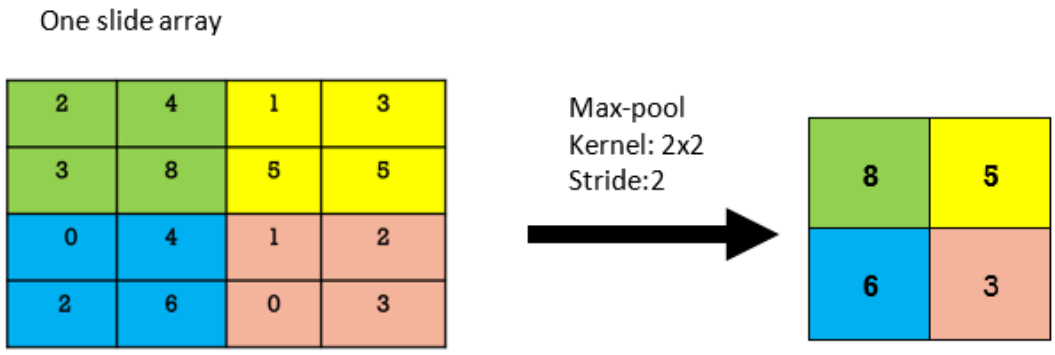

Figure 3-1: Max-pooling example with kernel size 2×2 and stride 2.

D- Fully Connected Layers

After several convolutional and max pooling layers, the data class in the neural network is generated via fully connected layers (FC). Each hidden unit in the FC layer is connected to all the units in the previous layer, and the weights of these connections are specific to each neuron. This makes a difference with the CONV layer, in which the units are connected locally to the input region.

3.3.2.2 CNN in Brain Tumour Segmentation

A two-pathway deep network with parallel pipelines was proposed by Davy et al. (2014). One pipeline is "convolutional" and comprises two CONVs and a MaxOut unit. The input to this pipeline is patches with a fixed size of 32 × 32 and considers a wider and more general region of the input image. The other pipeline is "fully connected" and consists of an FC and a MaxOut unit. This pipeline relates to two smaller patches from the input of size 5 × 5 and considers more local details of the image. Ultimately, the output of the two structures is combined with that of another FC layer and a SoftMax unit. This method was later used by Havaei et al. (2017), who developed an architecture with two stages of different kernel sizes for global and local contextual segmentations.

Pereira et al. (2016) presents an automatic segmentation method based on CNNs to explore small 3×3 kernels. According to Pereira et al. (2016), small kernels enable a deeper architecture to be designed and have a positive power to combat overfitting, given the smaller number of weights in the network. This study used intensity normalization as a pre-processing step, which is common in CNN-based segmentation methods. It was found to be very effective for brain tumour segmentation in MRI images. The same proposal was validated in the Brain Tumour Segmentation Challenge 2013 database (BRATS 2013) and Brain Tumour Segmentation Challenge 2015 (BRATS 2015), obtaining Dice Similarity Coefficient metrics of 0.88, 0.83, and 0.77, and 0.78, 0.65, and 0.75 for the Challenge dataset, respectively.

Castillo et al. (2017) introduce a convolutional neural network for brain tumour segmentation. This proposed method is based on DeepMedic with more convolutional layers; it is organized in three parallel pathways, each with its own input resolution, and fully connected layers in addition. The proposed method was tested over the BRATS 2017 dataset, reaching an average dice coefficient of 0.87 for whole tumours over the Challenge dataset.

A convolutional neural network is a patch-wise network that predicts the label of the central pixel. However, the labels of a central pixel cannot represent the entire content of a patch. Therefore, Chen et al. (2017) propose a label distribution and multi-feature networks in brain tumour segmentation. Label distribution is presented to help patch-wise neural networks extract features, while multi-level features are exploited to distinguish subtle differences.

Razzak et al. (2018) suggest a two-pathway-group CNN (2PGCNN) model which incorporates the global and local information in parallel. They further employ the cascaded 2PG-CNN architecture to enhance the overall performance.

A new method is presented by Hu et al. (2019), who designed multi-cascade CNNs to take care of several local pixel dependencies and multi-scale features of 3D MRI images. The output results of the CNNs were refined using conditional random fields.

Prasanna et al. (2019) propose a fully automated approach, the radiomics-based convolutional neural network (RadCNN), for segmenting gliomas by means of multi-modal MR images (T1ce, T2, FLAIR). The proposed method comprises two stages. First, the top features are extracted and selected, with RadCNN combining radiomic texture features (i.e. Haralick, Gabor, Laws). Then the selected texture map volumes are applied, along with the normalized multi-parametric MRI (T1c, T2w, FLAIR) scans as channel inputs to a 3D CNN for classification. The authors compare their method with the DeepMedic model which shows the best-performing automated brain sub-regions segmentation in the BRATS16 challenge dataset. The use of RadCNN improves DSC scores in the BRATS 2016 challenge dataset for both enhanced and whole tumours. However, it did not achieve state-of-the-art status in the BRATS 2017 challenge dataset for segmenting tumour regions.

3.4 Techniques Based on Image Semantic Object Segmentation

The aim of semantic segmentation approaches is to segment the image into its object regions, based on predicting one probability distribution prediction per pixel (Zheng et al. 2015), whereas the image classification-based model makes one probability distribution per image. Fully convolutional networks (FCNs) are powerful visual models that are based on image semantic segmentation. FCNs have been known in many studies to exhibit state-of-the-art performance in semantic image segmentation (Shelhamer et al. 2017; Long et al. 2015 and Li et al. 2017).

In the progression from coarse to fine prediction, FCNs can be trained end to end for pixel-wise prediction. FCNs predict dense outputs from arbitrary-sized inputs. Both learning and inference are performed a whole image at a time by dense feed-forward computation and back propagation.

3.4.1 Fully Convolutional Network Architectures

The FCN approach for the semantic segmentation of images was suggested by Long et al. (2015) and Shelhamer et al. (2017). This approach makes some modifications to the CNN architecture. First, a Skip layer is added between layers to fuse the finer appearance information from the shallow layers and the semantic information from the deep layers. The Skip architecture refines the semantics and spatial precision of the output. In the second modification, instead of a pooling layer an up-sampling process is used for learning dense prediction. Convolution operations have been suggested in the CNN final layer to extend it for semantic segmentation. Various CNN networks can be transferred to FCN. Experimentally, the VGG 16 network achieved the best result and performance in the FCN architecture. Therefore, this network will be used in the present thesis.

3.4.1.1 U-net Architecture

U-net architecture is an extension of the FCN model (Long et al. 2015) and it is used for end-to-end pixel-wise prediction. The U-net was proposed by Ronneberger et al. (2015). The network architecture, which consists of 23 layers, is illustrated in Figure 3-2. The U-net has two main paths: a contracting path and an expansive path. The typical architecture of CNN is followed by the contracting path (on the left-hand side). This path has two 3×3 convolutions, each followed by a rectified linear unit (ReLU). A max-pooling layer of kernel size 2×2 with stride 2 is included in each block of the architecture for downscaling. In the expansive path of the U-net (on the right-hand side), an up-sampling of the feature map is performed in each step followed by convolution with a kernel size of 2×2, which is called the up-convolution. The feature maps are concatenated with a cropped feature map from the contracting path. They are followed by two convolutions with a kernel size of 3×3 and two ReLUs. A convolution with kernel size 1×1 is implemented in the final layer of the U-net architecture to map each component of the feature vector to the anticipated number of classes.

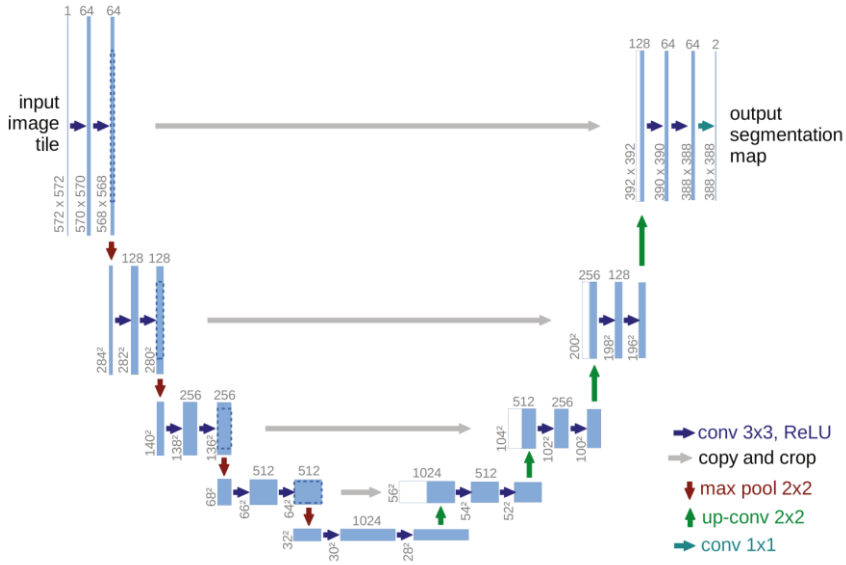

Figure 3-2: U-net architecture: example with 32×32 pixels in the lowest resolution (source: Ronneberger et al. 2015).

3.4.2 FCN for Brain Tumour Segmentation

Wang et al. (2017) introduces a cascade of fully convolutional neural networks to segment multi-modal MRI images with brain tumour: it consists of background, whole tumour, tumour core and enhanced tumour. The cascade is created to decompose the multi-class segmentation problem into a sequence of three binary segmentation problems, corresponding to the subarea hierarchy. In the first step, the whole tumour is segmented, and the bounding box of the result is used for segmenting the tumour core in the second step. Then the enhanced tumour is segmented according to the result of segmenting the tumour core by the bounding box. The results demonstrate that the proposed method of automatic brain tumour segmentation was competitive in performance.

Zhao et al. (2018) proposed a brain tumour segmentation model in two parts, a Fully Convolutional Neural Network (FCN) and a Conditional Random Field (CRF). The proposed model in three steps was trained using image patches and slices. FCN includes most parameters in the segmentation model. The training of the model was based on image patches, which were extracted from slices of the axial view, to address the problem of a lack of training samples, since thousands of patches can be extracted from each image. In addition, this training helps to avoid the imbalance inherent in a training

sample because the number and position of training samples for each class can easily be controlled by using different patch sampling schemes. The model was evaluated on a BRATS 2013 dataset and obtained second position on its Challenge dataset. This method performed well with only three imaging modalities (i.e. Flair, T1c, T2), instead of four (i.e. Flair, T1, T1c, T2) (Zhao et al. 2018).

FCNN has been successful in segmenting brain tumour tissues from FLAIR MRI modality. Lorenzo et al. (2019) introduce an approach for segmenting brain tumours from FLAIR MRI using FCNN. The FCNN is trained on 256 × 256 patches, formed only from those sub-areas of the original images that include tumours, and provides segmentations of full-sized FLAIR MRI scans. The authors find that the proposed model outperforms the best-known FLAIR brain tumour segmentation algorithm in the literature and presents very fast training and instant segmentation (with the proposed technique a whole FLAIR image can be segmented in less than a second).

3.5 Segmentation Evaluation Metrics

Classification is important in data analysis, pattern recognition and machine learning. It also enables intelligent decision-making (Norouzi et al. 2014). Classification is a process in which a model or classifier is constructed to predict class labels. In particular, the aim of classification is to accurately predict the target class for each case in the data (Kesavaraj and Sukumaran 2013). The simplest type of classification is binary classification, where the target attribute has only two possible values. Multiclass targets have more than two values. To use the supervised classification technique, a subset of observations and measurements for which the target value is already known should be defined as training data, which include both the input and desired results. The accuracy of a diagnostic test lies in its ability to distinguish between patients with disease and those without (Leeflang et al. 2018).

Typically, the results of the test are categorised as positive or negative for the target condition. The terms positive and negative originate in early medical applications, where patients with some observed medical phenomenon (e.g. an illness) were denoted as positive and the other patients were described as negative. A true positive (TP) arises when a patient is positive for illness and is classified as positive by the test. It is called a false negative (FN) when the classifier is predicted as negative. Similarly, if the patient

is negative for the illness but has a positive classifier prediction, it denotes a false positive (FP), while if both are negative, a true negative (TN) is established. In addition to accuracy, sensitivity and specificity are also used in evaluating medical diagnosis. Sensitivity indicates the proportion of true positives that have been correctly identified. In contrast, specificity refers to the proportion of true negatives that have been correctly identified (Orrù et al. 2012; Harefa and Pratiwi 2016). The sensitivity of a binary test is often expressed as its accuracy (Leeflang et al. 2018). Five measures are used for the assessment of binary classification, namely, accuracy, precision, sensitivity, specificity and balanced error rate (BER) (Majnik and Bosni 2013)

To evaluate the methods, many studies have used various combinations of tumour parts, which makes a comparison between them difficult. Consequently, the BRATS challenge organisers have provided the tumour parts most often referred to. Several methods can be used for segmentation, including the Dice similarity score (DSC), sensitivity, and the positive predictive value (PPV). Figure 3-3 shows the segmented regions that were used for evaluating the segmentation method in the present study. The tumour region was assessed according to Menze et al. (2015), especially the complete tumour region, the core tumour region except the "oedema" and the enhancing tumour region, which included the enhanced tumour structure.

For each tumour region, the F-measure was computed as follows (Davy et al. 2014; Menze et al. 2015):

$$Precision = \frac{TP}{TP+FP} \quad (3\text{-}2)$$

$$Recall = \frac{TP}{TP+FN} \quad (3\text{-}3)$$

$$F - measure = \frac{2(Precision \times Recall)}{Precision+Recall} \quad (3\text{-}4)$$

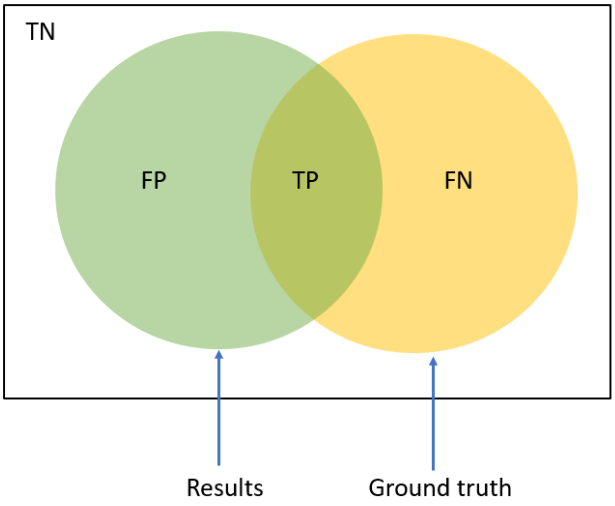

Figure 3-3: An example of TP, FP, TN and FN. The green circle region represents the results, the yellow circle region represents the ground truth.

3.6 Works Related to Ischemic Stroke Lesion

Strokes are a leading cause of death and disability worldwide (Subbanna et al. 2019). An ischemic stroke is caused by an obstruction in the cerebral blood supply, which leads to infarction of the affected brain tissue. An automatic segmentation of high accuracy and reproducibility is of great interest because the lesion volume is an important endpoint for clinical trials. However, factors such as the wide variation in lesion shape, location and appearance make this a difficult task. Therefore, a fully convolutional neural network model for segmenting ischemic stroke lesions in CT perfusion images was developed for the ISLES 2018 challenge by Abulnaga and Rubin (2018).

A novel framework based on deep CNNs to segment the acute ischemic lesions in DWI is presented by Chen et al. (2017). Their results were validated on a large dataset of 741 subjects acquired by DW images and their study achieves a mean accuracy of the Dice coefficient obtained, 0.67 in total. The mean Dice scores based on subjects with only small and large lesions were 0.61 and 0.83, respectively (Chen et al. 2017).

In another study, Kamnitsas et al (2017) have obtained excellent performance results in the challenging task of sub-acute stroke lesion segmentation using a dual pathway, which was 11 layers deep, using a 3D convolutional neural network called DeepMedic. Zhang et al. (2018) demonstrated the 3D FCDenseNet, which can make the network deeper by using an improved dense net tight connection structure to enhance the back propagation of image information and gradients. In a study by Subbanna et al. (2019), they propose a new method for segmenting sub-acute stroke lesions unimodally from fluid-attenuated inversion recovery (FLAIR) MRI datasets. It uses three databases to develop and evaluate a method for lesion segmentation. The results obtained by the proposed technique are superior to previous results and were obtained by two methods based on convolutional neural networks and three phase level-sets using multi-modal imaging datasets in the ISLES 2015 challenge.

3.7 Conclusion

This chapter has reviewed the relevant literature and then the approaches taken in automatic brain tumour segmentation in MRI images, as follows: image object classification-based techniques and the hand-crafted feature methods that are commonly used for automatic brain tumour classification; the decision tree (DT) a supervised classifier that has been used for brain tumour classification in many studies; image semantic object segmentation-based techniques used for brain tumour segmentation. Then some commonly used evaluation methods were introduced and finally it briefly presented the related works on imagining ischemic stroke lesions. Medical image segmentation is still a challenging task and further research is needed to improve the accuracy and robustness of segmentation methods. Merging different modalities, methods, and clinical knowledge may help to improve medical image segmentation methods. In view of this, the next chapter will discuss a combined method for the accurate segmentation of brain tumours.

Chapter 4

The Segmentation of Brain Tumour Tissue based on Image Classification

4.1 Introduction

The decision tree (DT) classifier is often chosen of all conventional classifiers for brain tumour segmentation (Menze et al. 2015; Rehman et al. 2019). Furthermore, hand-crafted features have been input into the DT classifier (Bharath et al. 2017; Phophalia and Maji 2017; Revanuru and Shah 2017). A good description of the different tissue classes must bring in many features. However, every high dimensional feature vector means a complex procedure and high computational cost. This limitation was mitigated by using another variant of the discriminating approaches. deep convolutional neural network methods have recently attracted attention in the classification of images. Some of the CNN-based approaches have been adopted for segmenting brain tumours in medical images, especially in MRI data (Havaei et al. 2017; Zikic et al. 2014 and Pereira et al. 2016). In the CNN-based approaches, classification is performed by labelling the central pixel patch. In consequence, the main limitation of the CNN-based method is that the local pixel dependencies are not considered enough for pixel classification. Meanwhile, hand-crafted features such as histogram-based texture features have proven to be robust descriptors of pixel local dependencies. Hence, the main contention of this chapter is that more local information can be gathered by fusing machine-learned features with hand-crafted features to improve the classification method in brain tumour segmentation.

In this chapter, CIFAR architecture was selected for model implementation because the CIFAR network performs classification tasks well. However, the size of the input images to the CIFAR network is 32×32 pixels, which restricts the size of the input image patches in our work. Because the pooling layers in the CIFAR architecture cause down-sampling in the data, some of the layers in the CIFAR architecture cause down-sampling in the data and therefore some of the image information that is useful for learning is lost. Moreover, the centre pixel of an image patch that is 32×32 pixels in size does not have enough dependencies to give a label for this patch, where much of tissue information is overlapping. In other words, only a limited space of the context features is explored because the method is patch-wise. Accordingly, to obtain more accurate classification a histogram-based texture is used to compensate for the lost information by providing features in which the neighbouring pixels are closely correlated.

Considering the Hybridge method or combing two or more methods is useful for compensating the limitations in the performance in one of these methods. Histogram texture features method has limitation. This method needs large feature vectors to improve its classification performance which lead to cost computational time. However, histogram texture features method has ability to provide robust feature descriptors of pixel local dependencies. Therefore, this method is combined with CIFAR network to compensate the limitation in the CIFAR network (not enough considering the local pixel dependencies) and in the same time it is not need large feature vector to do the brain tumour segmentation.

The motivation of this chapter is to generate a model that can extract useful features from the MRI images, such as local dependency features, and then combine them with machine-learned features. This model would be useful for the accurate segmentation of complex tumour structures.

The contributions of this chapter can be summarized as follows:

- A novel histogram-based texture descriptor developed for each interesting pixel within each MRI modality, using an image threshold method, based on clustering, named Otsu's method. The distribution of similar intensities of different brain tissues is used to encode the local correlations between the neighbouring pixels in feature representation.

- A new method to address the limitations of the CIFAR network and improve the performance of brain tumour segmentation by combining hand-crafted features with the machine-learned features that are extracted from the last fully connected layer of the CIFAR architecture.

- A decision tree-based method for segmenting brain tumour accurately, based on the above combined features together with image intensities.

4.2 CIFAR as Classifier for MRI Segmentation

The concepts and the modifications of the CIFAR architecture will be explained in detail in the two following sections.

4.2.1 CIFAR model architecture

The CIFAR network is designed as a series of convolutional layers for the task of image classification. The details of the CIFAR network are shown in Figure 4-1. The CIFAR model takes images 32×32 pixels in size as an input to the first layer. Above the input layer, the middle layers of the network are made up of three blocks, repeated. Each block consists of a convolutional layer with a kernel that is 5×5 in size; it has a pad of size 2 and stride of size 1, followed by the ReLU and a Max pooling layer with a pool size 3, stride size 2 and padding size 0.

The convolutional layers are defined as sets of filter weights, which are updated during network training. The ReLU layer improves the non-linearity of the network, which permits the network to carry out approximate non-linear functions that map image pixels to the semantic content of the image. The final layers of the CIFAR model are typically composed of two fully connected layers, which lead into SoftMax and a classification output layer. The model follows the architecture described by Alex Krizhevsky (Krizhevsky 2009). The other reason for selecting CIFAR net in this chapter is that the model is small enough to train quickly, which is ideal for trying out new ideas and experimenting with new data.

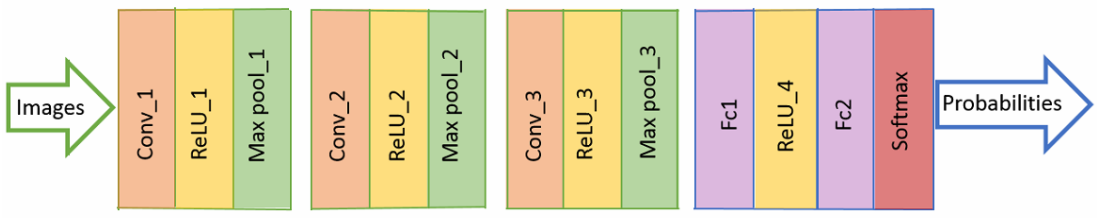

Figure 4-1: Schematic architectures of the CIFAR classification network.

4.2.2 Retrained CIFAR for brain tumour segmentation.

The CIFAR model is pre-trained to distinguish 10 classes using the CIFAR-10 data set, which has 50,000 training images. These images are RGB, 32x32 pixels in size. Transfer learning is commonly part of deep learning applications. Therefore, a pretrained CIFAR network can be trained again to classify a new set of images. Additionally, the more abstract features of images that are more common among some types of image than others are learned in the first layers of any CNN. Hence, the learned features can be rapidly transferred to a new task using a smaller number of training images. In this chapter, the F-measure 0.67 is obtained by use of the CIFAR model without pretraining for a whole tumour, which is a poor segmentation. This was possible because the model was trained from scratch, with brain tumour data set that was insufficient. This suggests that using pre-trained CIFAR model speeds up the training procedure with more accurate results in a specific epoch number, because the network has learned rich feature representations for a wide range of images. The pre-trained CIFAR network is modified and adopted for the segmentation of a brain tumour in MRI images. Some modifications in the pre-trained CIFAR should be considered. Starting with input data, the CIFAR model is designed to train RGB natural images that have three channels each 32×32 pixels in size. Three MRI models (FLAIR, T1-contrast and T2-weighted) were correspondingly employed to figure out the input data. T1 modality was not selected as input data because it does not carry enough information for tumour regions. The choice of these MRI protocols and of scale extraction of the patches in MRI images in this method is discussed in Section 4.3.1.1, below. To fine tune and retrain CIFAR to classify MRI images, the last layers are replaced and the fully connected layer (FC2) of the network, which previously had 10 classes, is set to the desired number of classes. Four categories – background, oedema, necrosis, and enhanced tumour – are used for the task of brain tumour segmentation. Additionally, the learning rate factors of the fully connected layer are increased so that they learn more quickly in the new layers than in the transferred layers. Figure 4-2 demonstrates all the transfer learning in the pre-trained CIFAR network.

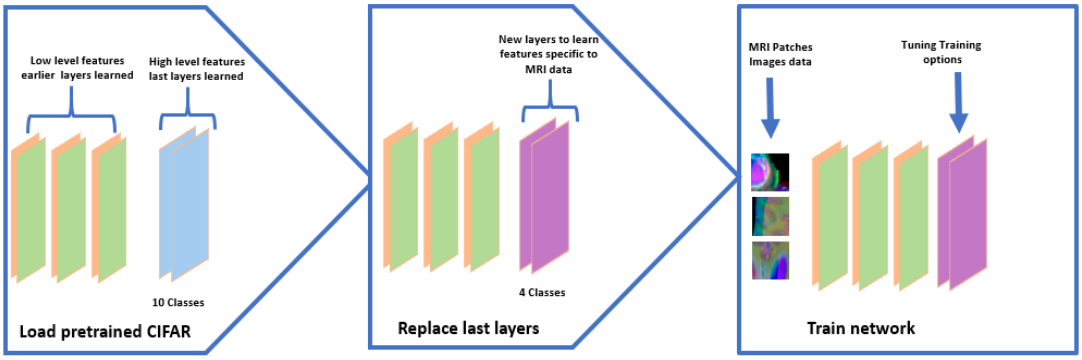

Figure 4-2: Reuse of pre-trained CIFAR model.

4.2.3 Prediction Mask for a Brain Tumour Using CIFAR

In a brain tumour, the CIFAR model makes a single probability distribution prediction for the central pixel of each patched image. The network is then trained to predict which class this pixel belongs to. The results of the classification output prediction mask are illustrated in Figure 4-3.

From the results it can be seen that the global detection of the tumour structure was successfully achieved using the CIFAR classifier. However, smooth boundaries and some misclassification between classes can be recognized in some tumours and parts of tumours (sub-tumours). This suggests that the centre pixel of such a small image patch (size 32×32 pixels) does not have enough dependencies to give a label for this patch, which includes a good deal of overlapping tissue information. In other words, using a patch-wise method limits the space of the context features that is explored. To address this limitation and improve the results, finer segmentation is required. This is achieved by combining more contextual information from the local dependencies of the pixel. Consequently, the next section introduces the hybrid method, which integrates the hand-crafted features that reflect the histogram-based texture features with the CIFAR features to compensate for the limitations of the latter and improve the performance of brain tumour segmentation in MR images.

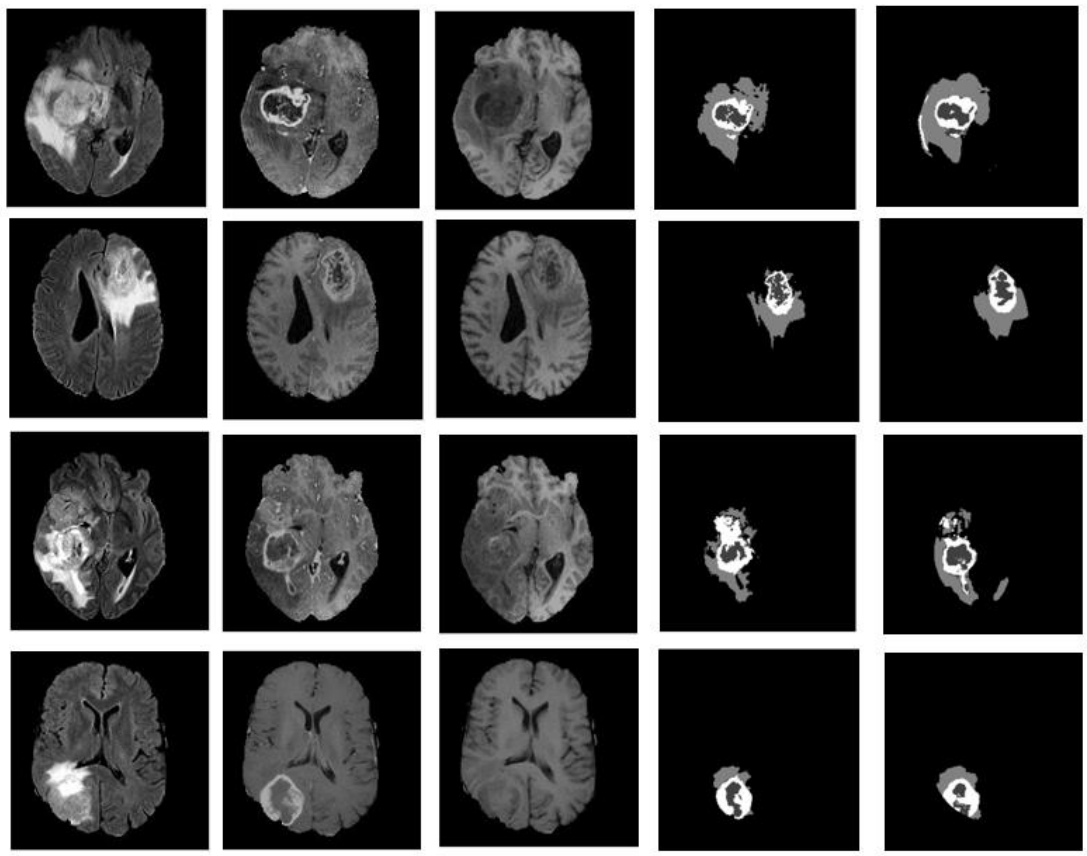

Figure 4-3: FLAIR, T1ce and T2 MRI models, ground truth and the CIFAR network segmentation mask (left to right).

4.3 Methodology

The general framework of our proposed method in this chapter comprises four main stages: pre-processing, CNN design, extracting texture features and classification. In the pre-processing step, the image intensities of a multimodal MRI are normalised because the complex brain tissues in MRI overlap. Then MRI models (FLAIR, T1ce and T2) are divided into regular patches that are approximately similar in size and intensity values. The image patches are then fed into the CNN system to generate the highest scores for the brain tumour classes as machine-learning features. From the same MRI models, texture intensity histogram features are extracted as hand designed features. In the last step, both feature types are joined together with the pixel intensity of the same images and are then fed into a DT classifier to divide the pixels of each MRI image into regions of healthy tissue and sub-tumour tissue. The overall workflow of the proposed method is shown in Figure 4-4.

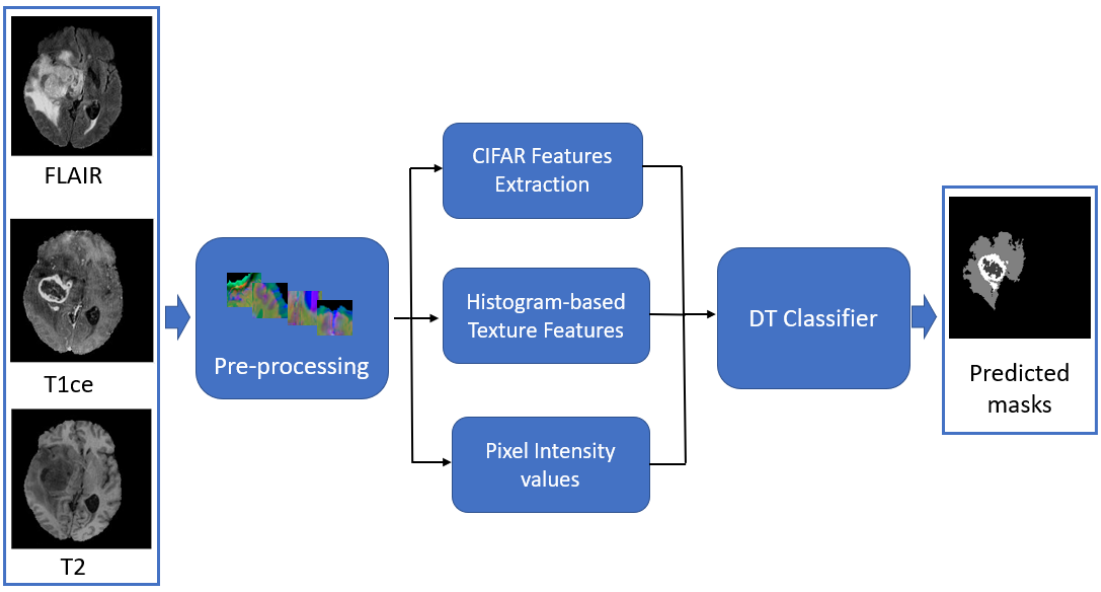

Figure 4-4: Flowchart of the proposed system.

4.3.1 Pre-processing

MRI data are sourced from different MRI institutes and integrated so as to acquire enough study cases various different manufacturers and scanner-models are included. This is why several kinds of artefact, such as non-homogeneity, occur in the dynamic intensity range of brain tissue. Consequently, significant variance is found in the tissue intensity behaviours of brain MRI volumes. These artifacts can affect the quality of the data and can limit the performance accuracy of the segmentation results for different segmentation techniques in medical imaging, because they cause false intensity levels, which leads to false positives in the automated segmentation. To compensate for the non-homogeneity of MR and to reduce the effect of the whole pixel intensity on the models, a bias field correction algorithm based on N4ITK (Tustison et al. 2010) and intensity normalisation are both applied to the MRI models. Figure 4-5 illustrates a typical MR image, with and without the bias field. In the first scan, higher intensity values are observed near the bottom left-hand corner, which can lead to false positives in the predicted output mask. By correcting the bias in the second scan, a better contrast is achieved near the edges of the MR image. Therefore, the additive bias field should be removed to improve the accuracy in segmentation.

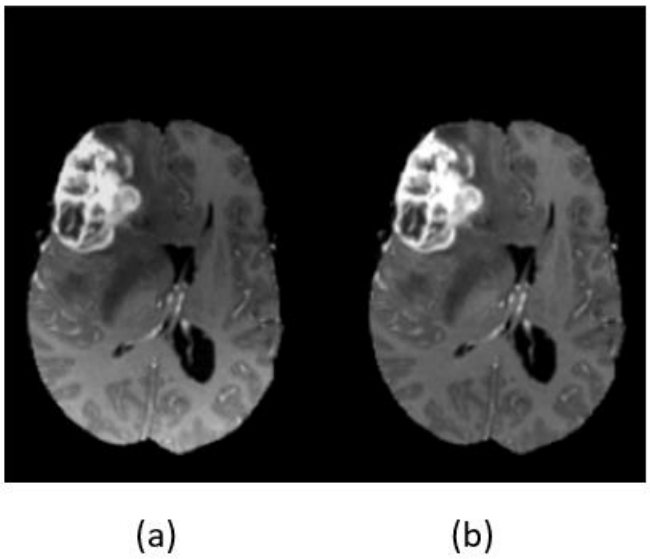

Figure 4-5: MRI scan: (a) before (b) after N4ITK bias field correction.

Intensity normalization is applied to the bias field correction to take the mean intensity value and variance close to 0 and 1, respectively. This process is important for features that are based on intensity values in classification-based segmentation methods; it ensures that the values of these features are normalised with the comparable dynamic range. Equation (4-1) shows the formula that was used to compute the normalized slices I_{n}.

$$I_n = \frac{I-\mu}{\sigma} \tag{4-1}$$

where I represents the original intensity value of the MRI slice, and μ and σ are the mean and standard deviation of I, respectively.

After normalisation, the top and bottom 1% intensity values for each image were removed. The 1% highest values corresponded to the hyper-intensities of the remaining pixels related to the skull, while the 1% lowest values represent background noise.

4.3.1.1 Image Patch Extraction

Most brain tumour segmentation studies that are based on classification methods divide the MR images into 2D image patches of specific size as input data (Pereira et al. 2016; Havaei et al. 2017; Zikic et al. 2014). Usually, these patches are extracted by using a sliding square window structure with size M^2 and a specific sliding step. These square areas are designated a defined type according to the category of the centre pixel.

The patches can give the classification model access to information about the pixel's regional environment because the class of any given pixel is highly dependent on the class of its surrounding pixels, which affects the final prediction of the class of the patch. However, there is a data imbalance problem in brain tumour segmentation because a large number of pixels (98%) belong to the healthy category of brain tissues and only the remaining pixels (2%) represent the pathological part of the brain tissues. Consequently, the patch selection technique helps to ensure that the data from the classes input to the classification model (e.g. CNN) are balanced. Otherwise, the net in the total image will be overwhelmed with the class of the larger percentage and will fail to identify any of the minority classes.

Some studies used patch size 33×33, while other studies used 17×17, 15×15 and 13×13, it depends on the user design for the best performance of brain tumour segmentation. In this study, patch size 32×32 (overlapped by 3 pixels) was used as it is the usual input size of the pretrained CIFAR network.

The patches in this work were selected in several steps, a procedure which had a great impact on the results. First, selecting the patch size: after combining the three MRI models (FLAIR, T1ce, T2), a fixed square window 64 × 64 in size was used to extract patches from the FLAIR model and another 32×32 in size was used to extract patches from the other two MRI models (i.e. T1ce and T2). All of the corresponding patches of different sizes were centred at the same pixel. A patch size of 64×64 instead of 32×32 was selected for the FLAIR modality because FLAIR is considered to be a highly effective MRI sequence image that provides helpful information for separating the whole region of the tumour boundary from the healthy tissue (Jin et al. 2014). In addition, a large patch size of 64 × 64 was found to be big enough to provide global information on special features for machine learning (Havaei et al. 2017). Meanwhile, a patch 32×32 in size was selected for the T1ce and T2 modalities because a smaller

size was needed to provide local details for machine learning. The T1ce modality provides information related to the necrosis and the active tumour region (the enhanced tumour), which can be distinguished easily, while the T2 modality presents more information related to the tumour structure and healthy tissues (Bauer et al. 2013) (see Figure 4-6).

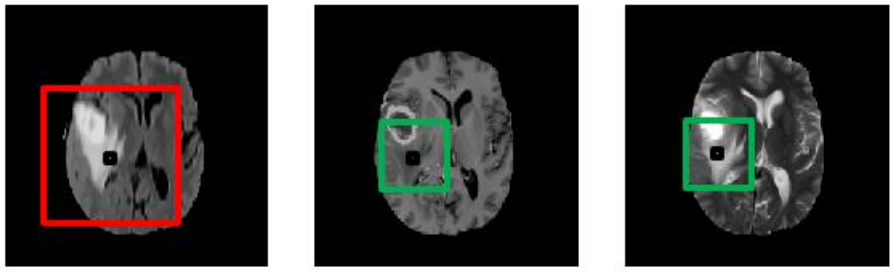

Figure 4-6: (a) Flair model with a patch of 64 × 64, (b) and (c) T1ce and T2 models, each with a patch of 32×32.

The second step involved control of the patch selection. Normally, patches are randomly selected from the MRI data according to class. However, the trained model that derives from this selection usually classifies most patches within the area of the brain tissues as tumorous and classifies as background only the patches within the black area. It does so because about half of the background patches are in the zero-intensity area with no brain tissue (see Figure 4-7).

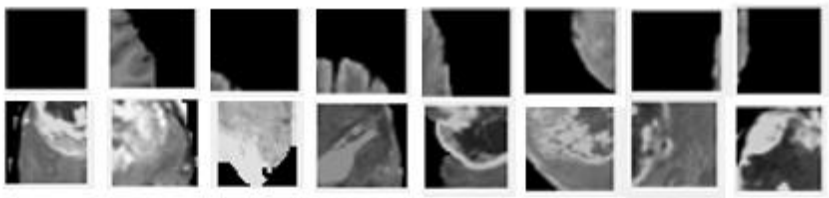

Figure 4-7: Top: image patches selected randomly; bottom: image patches with controlled selection.

Nevertheless, when the selection process is controlled to exclude patches in which more than 20% of the pixels are of zero-intensity, the results can be significantly improved (see Figure 4-8).

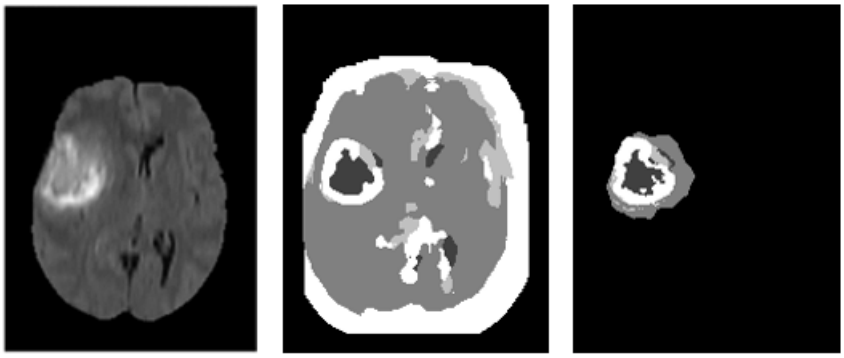

Figure 4-8: An original MR image, the result with random patch selection and the result with controlled patch selection (left to right).

4.3.2 CIFAR-based Feature Extraction

In a trained CIFAR network, each layer produces filter responses to an input MRI image. However, only a few layers within a trained CIFAR are suitable for image feature extraction. Basic image features, such as edges, corners, and blobs, are captured at the beginning of the network. Then, by using the deeper network layers, these primitive features are processed to form higher level image features. These higher-level features are better suited for the task of brain tumour classification because they join all the primitive features together to form a better representation (Donahue et al. 2014). Typically, the layer immediately below the classification layer is a good place for feature extraction because it includes the number of scores equal to the desired classification labels, which comprise background and normal brain, oedema, necrosis, and enhanced tumour. A four-dimensional feature vector is constructed from each pixel in the MRI images, with values that are equivalent to the probability values of the feature extraction layer (see Figure 4-9).

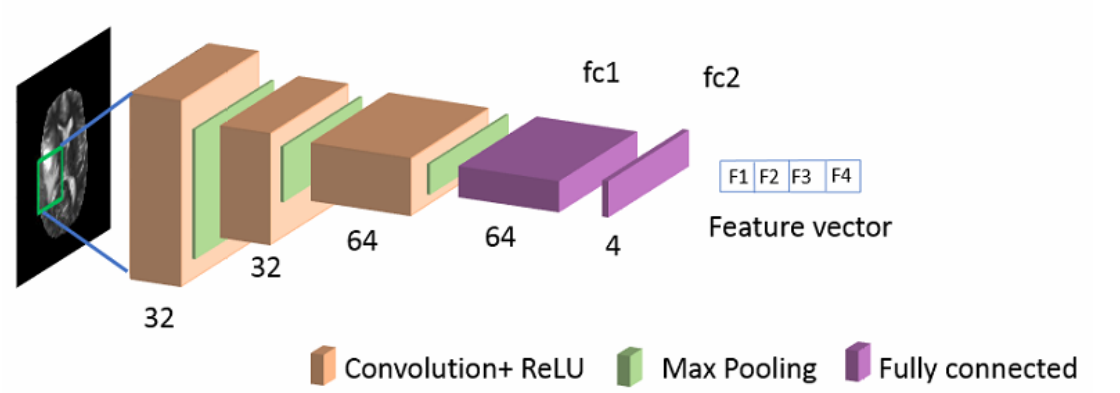

Figure 4-9: Feature extraction by CIFAR from a second fully connected layer.

4.3.3 Histogram-based Texture Feature Extraction

The distribution of the grey level values of the various tissues and the spatial geometric relationship between these tissues can be introduced into the segmentation algorithm (Zeng 2013). Typically, feature extraction algorithms for medical image segmentation are categorised as shape, intensity, and texture-based features. Most of the parameters of the feature extraction methods are set or optimised manually, designating these features as hand-crafted features. Brain tissues have complex structures that contain normal tissues overlapping tumorous regions. Consequently, the shape and intensity features are not enough to segment the brain tumour in MRI images with much accuracy. This task requires methods that are focussed on local or neighbourhood information, such as texture features. Therefore, histogram-based texture features were considered in this work as hand-crafted features for segmenting brain tumours and sub-tumours. The whole process of the histogram-based texture feature descriptor takes three steps: the Otsu threshold, quantizing of images and calculating the intensity histogram.

Otsu's method is one of the better threshold selection methods; it gives an acceptable result when the numbers of pixels in each class are closely similar. It entails an unsupervised algorithm that uses information about the neighbouring pixels in the image and directly works on the grey levels of the histogram by selecting the threshold which yields the greatest difference (Otsu 1979). Image quantization applies the multi-level thresholding version of Otsu (Liao et al. 2001) to grayscale images and produces a reasonably segmented image with the pixels clustered appropriately. In this method,

each MRI model (FLAIR, T1ce, and T2) is decomposed into clusters based on the multi-level thresholds of Otsu's method. The number of thresholds is a tuneable parameter that is defined or selected empirically by the user, based on the number of healthy and pathological tissues. In an MR image of a brain tumour, the major tissues are the enhanced tumour, necrosis, oedema, white matters (WMs), grey matters (GMs) and cerebrospinal fluid (CSF). Thus, each quantized image is assigned by ID based on the cluster number ($K_{Cluster}$**)** that is generated by applying the threshold number ($I_{Threshold}$). Figure 4-, Figure 4- and Figure 4-7 depict the process of generating image quantization with different clusters (4, 6, and 16) using different numbers of thresholds (3, 5, and 15). The labels also appear in different colours.

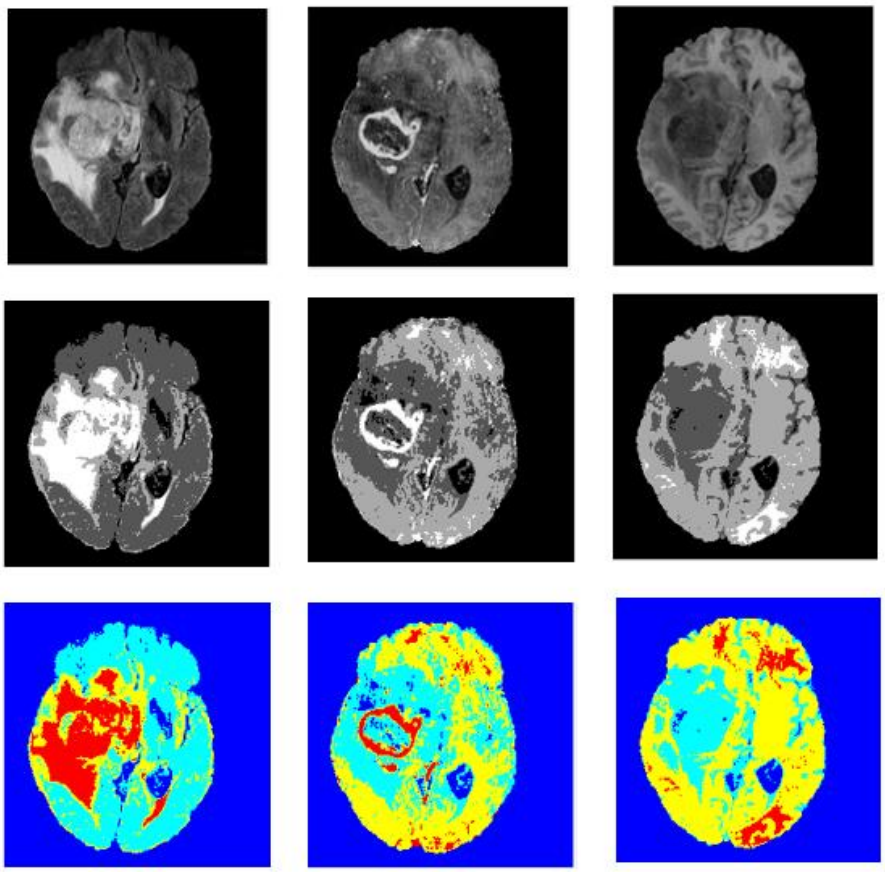

Figure 4-10: Original MR images (FLAIR, T1ce, T2), quantized images using three thresholds, and quantized image using three thresholds but with RGB labelling (rows left to right, top to bottom).

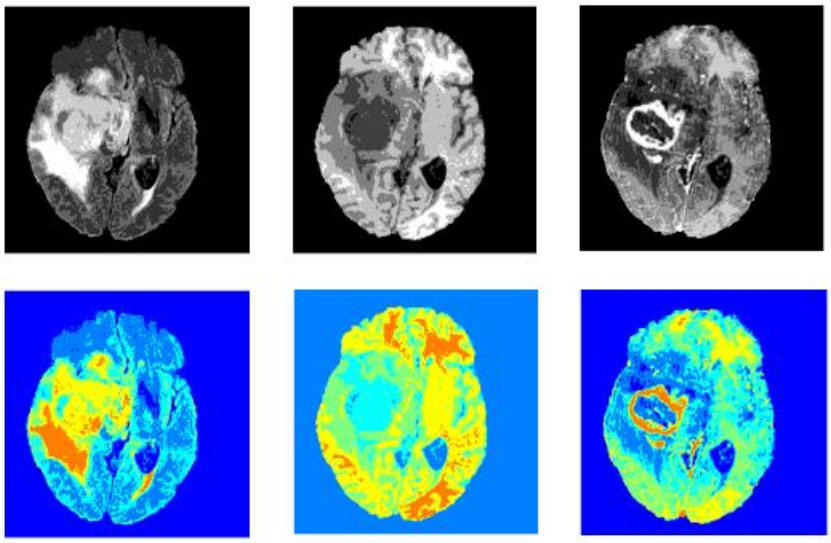

Figure 4-11: Quantized images using 5 thresholds, quantized image using five thresholds but with RGB labelling (rows left to right, top to bottom).

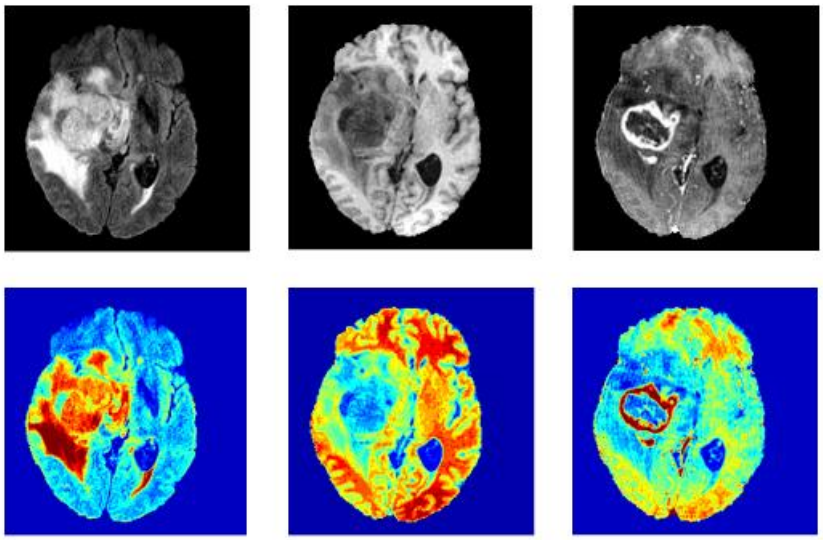

Figure 4-7: Quantized images using 15 thresholds, quantized image using 15 thresholds but with RGB labelling (rows left to right, top to bottom).

A histogram can represent the texture feature of a centre pixel with its neighbourhood of size m in pixels. In this work, the texture feature-based histogram is computed by summing up the intensity values of the original MRI modalities (FLAIR, T1ce and T2) corresponding to each cluster in the window. Various fixed window sizes of 5 ×5, 7 × 7, 9 × 9 and 11 × 11 were experimented with. The results are not affected when window sizes 5 × 5 and 7 × 7 are used, but the best result was obtained when the size of the window was 9 × 9 because this window was big enough to provide local information for labelling the central pixel. A window 11 × 11 in size was not used because it would have given similar results to those obtained with a window of 9 × 9 pixels but would have taken more time.

Normalized intensity representing the centre pixel was also used in pixel classification. This meant that a feature representation descriptor of each pixel could achieve local dependencies by encoding information about the centre pixel, which conditionally depends on its neighbourhood. An example of histogram intensity is demonstrated in Figure 4-8.

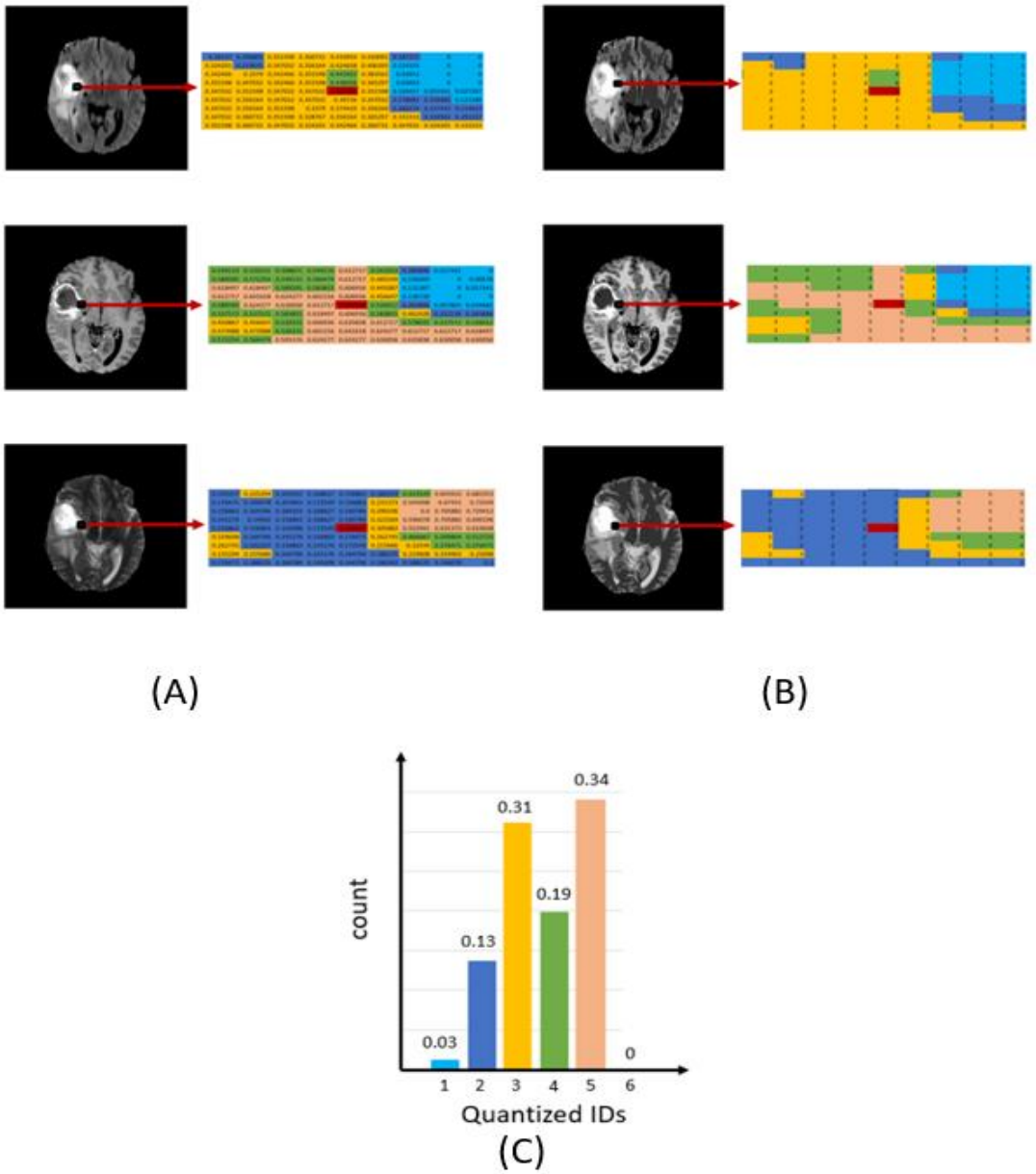

Figure 4-8: (a) Top downwards demonstrates FLAIR, T1ce and T2 MRI models, in sequence, with 9×9 pixel intensities in the neighbourhood of the centre pixel. (b) Top downwards illustrates quantized images of the corresponding FLAIR, T1ce and T2 MRI models with a 9×9 ID neighbourhood of centre pixel. (C) Mapping the 9×9-pixel intensities neighbourhood of the centre pixel of the three MRI modalities into an intensity histogram.

4.3.4 Hybrid Features

As discussed in Section 4.3.3, a histogram-based texture feature is considered to be hand crafted and provides a robust descriptor that indicates the local dependences. It follows that more local information will be incorporated by combining histogram-based texture features with the CIFAR-based feature and this will improve the final brain tumour segmentation. In total, 13 features, described in Table 4-1, were calculated from a number of MRI protocols.

Table 4-1: Total number of features calculated from concatenated hand-crafted features with machine learning features in MRI protocols.

Features calculated from pixels	One modality	Multimodalities of MRI (FLAIR, T1ce, T2)
CIFAR	-	4
Histogram based texture	6	6
Normalized intensity	1	3
Total	7	13

As described in Section 4.2.2, the CIFAR features that are considered machine features were extracted from the second fully connected layer for the corresponding pixel. Meanwhile, the texture features which were represented as hand-crafted features were extracted according to the histogram of the quantized image in a fixed window of 9×9, centred at this pixel. The pixels inside the brain region which is represented in the target area were considered for the generation of a feature vector (i.e.13 features for each pixel).

4.3.5 DT Classifier and Parameters Selection

DT was used for classification in this work, as described in detail in Section 3.3.1.1. DT is a flowchart-like tree structure that is used to categorise each pixel as part of a healthy or tumorous brain tissue. Where each internal node of the tree represents a test of an attribute, the outcome of the test is represented by each branch and the class label is represented by each terminal node (or leaf node). The trees are grown to a specified tree depth (D_{tree}), which represents the main parameter of the DT classifier that is designed.

After extracting the feature vectors from the pixels in the brain region, all these feature vectors are then fed into the DT classifier for training. To select the optimum parameter of the DT classifier, certain varieties of D_{tree} were calculated on the BRATS 2017 training patient datasets. 4-fold cross validation data were used to assess the accuracy of the classification and determine the effects of D_{tree}. Figure 4-9 shows that a DT with D_{tree} = 100 provides an optimum generalisation and accuracy. It should be noted that D_{tree} = 120 also provided optimal results. However, in order to minimise the computational costs, D_{tree} = 100 was selected.

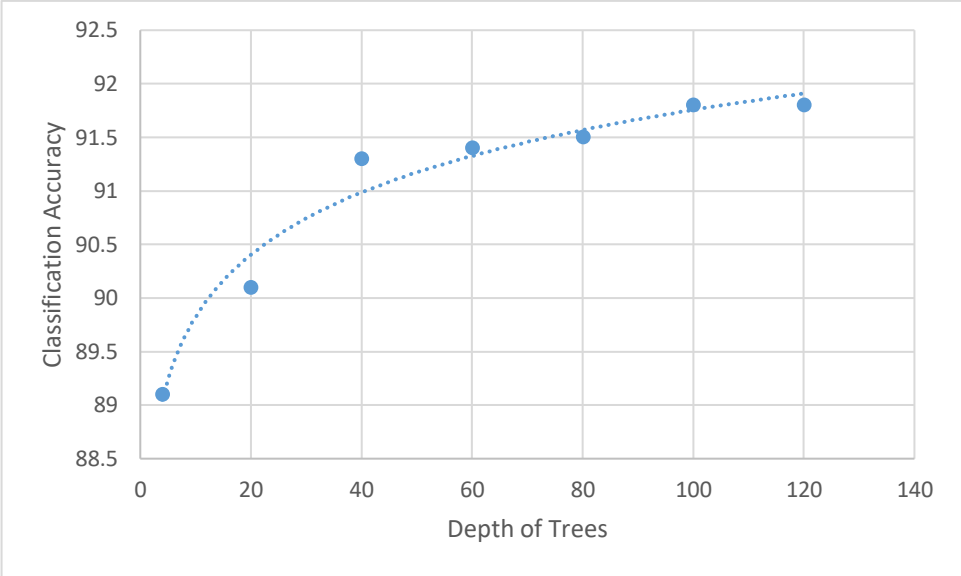

Figure 4-9: Tree depth effects on the classification accuracy of DT classifier.

4.4 Experiment Results

In this section, the evaluation results of the proposed method of multimodal brain tumour segmentation are described. First, the dataset, and, next, the parameter setting of the model and the evaluation methods of segmentation results are described. Following this step, the results analysis is reported.

4.4.1 Dataset

In this study, the BRATS 2017 dataset was chosen. This dataset includes MRI scans from 285 patients, as noted above in Section 2.5.1.1. Basically, 75% of the patients (158 HGG and 57 LGG) were selected as a training dataset to train the model and 25% (25 HGG and 18 LGG) were made the testing set. Three MRI protocols (FLAIR, T1ce, and T2) were used as an input to the CIFAR network because CIFAR was designed for three input layers. The tumour information structure presented in these three MRI models performed tumour segmentation well. Therefore, this configuration was selected in this work.

4.4.2 Implementation and Evaluation.

The performance of the model was evaluated on the testing set. Mostly due to practical clinical applications, the tumour structures were treated as three different regions, as follows:

1. The complete tumour region (comprising all four intra-tumour classes (oedema, necrosis, enhanced tumour), labels 1, 2 and 4).
2. The tumour core region (as above but excluding the oedema regions), labels 1 and 4.
3. The enhanced tumour region, label 4 only.

Chapter 3 described how the F-measure is used to evaluate the overlap ratio between the segmentation results and the manually defined brain tumour regions.

The proposed algorithm was implemented using MATLAB 2018a and ran on a PC with CPU Intel Corei7 and RAM 16 GB using the Windows 7 operating system. Our implementation was based on the specialized MATLAB deep learning toolbox and classification learner toolbox, which was also based on MATLAB for training the DT classifier. Regarding deep learning, the whole training process for the CIFAR model took approximately two and a half days on a single NVIDIA GPU Titan XP.

4.4.3 Experiment Setting

The performance of the proposed model was evaluated as an investigation of the four qualified experiments.

4.4.3.1 CIFAR

CIFAR classification was applied to the BRATS2017 challenge dataset for initial tumour segmenting (tumour location). This scenario used pre-trained CIFAR. No parameter or hand designed turning was required at this stage. Table 4-2 provides the evaluation results and Figure 4-3 shows the predicted masks of the brain tumours using the CIFAR classification method only.

Table 4-2: Segmentation results on the split testing dataset from BRATS 2017 using CIFAR.

Method	F-measure		
	WT	**TC**	**ET**
CIFAR	0.76	0.63	0.58

The results show that the F-measure for the whole tumour region was significantly better than it was for the tumour core and enhanced tumour. This demonstrates that CIFAR can segment the location of the tumour or the area that contains the tumour regions, but it cannot accurately detect or determine the exact boundaries of the tumour.

4.4.3.2 CIFAR_DT

In this setting, features were extracted from the previously trained CIFAR network. The extracted features were generated by applying the CIFAR network to the BRATS training dataset for each patient. Then the CIFAR extracted features were thought of as feature vectors and fed into the DT classifier for training. The DT parameter was tuned by examining a range of numbers of trees. The DT parameter was obtained by applying a 4-fold cross validation to the training dataset. Optimum accuracy was achieved when a 100 tree depth was chosen.

Table 4-3 provides the evaluation results obtained by implementing the machine learning features, which represent the CIFAR extracted features in the trained DT classifier model using the BRATS testing dataset. Figure 4-10 illustrates the segmentation masks using the CIFAR_DT method.

Table 4-3: Segmentation results on the split testing dataset from BRATS 2017, using the CIFAR_DT method.

Method	F-measure		
	WT	TC	ET
CIFAR_DT	0.74	0.62	0.58

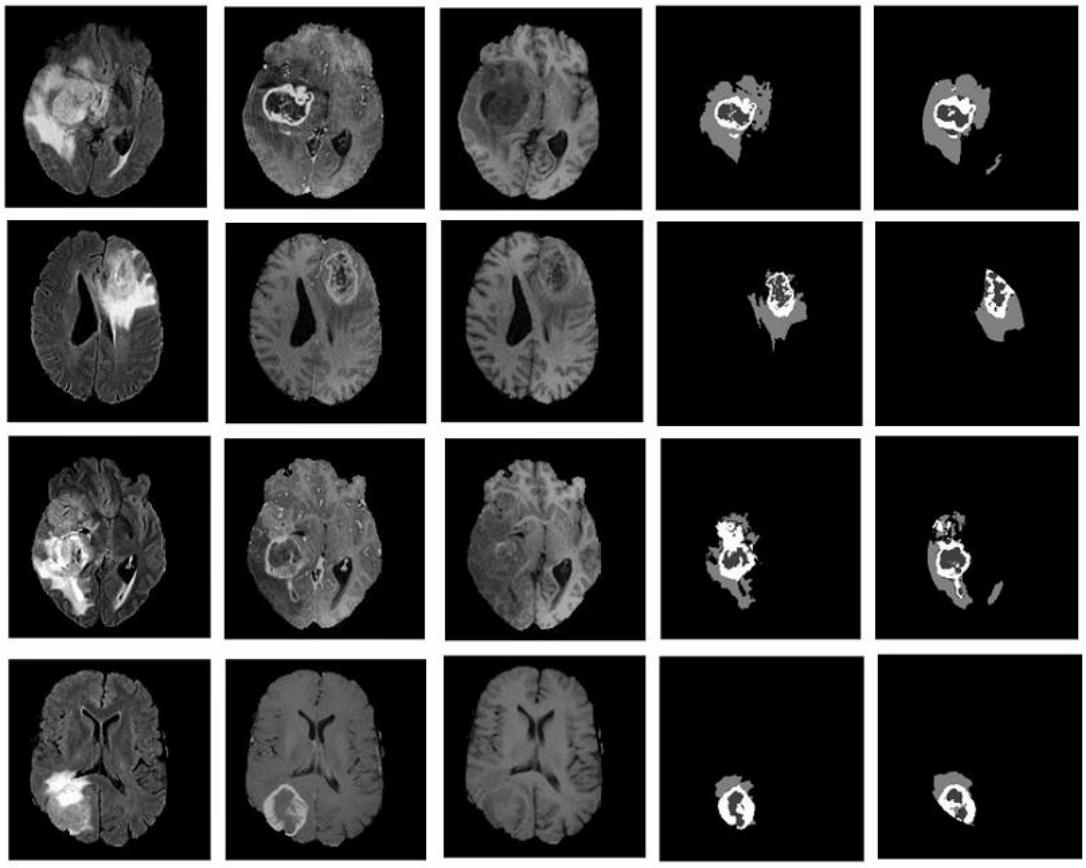

Figure 4-10: FLAIR, T1ce and T2 MRI models, ground truth and CIFAR _DT segmentation masks (left to right).

The result in Table 4-3 demonstrates that the CIFAR_DT slightly lowers the F-measure in WT and TC and preserves it in EC. This means that the CIFAR features can match more precisely with the deep learning classifier in the last layer than with the machine learning classifier (DT). The classifier layer in the CIFAR network is perfectly interpreted and the deep learning features are able to predict the label of the specific pixel.

4.4.3.3 CIFAR _PI_DT

In this setting, the experiment was designed to assess the effect of normalized pixel intensity in brain tumour segmentation. After generating the CIFAR features using the same setting as in Section 4.4.3.2, the CIFAR feature extractions were combined with a specific normalized pixel intensity for each MRI model (i.e. FLAIR, T1ce and T2) and treated as feature vectors to feed the DT classifier for training on the BRATS training dataset. Table 4-4 reveals the evaluation results obtained by applying CIFAR_PI_DT method to the BRATS testing dataset. Figure 4-11 shows images of the brain tumour segmentation results using the CIFAR_PI_DT method.

Table 4-4: Segmentation results on the split testing dataset from BRATS 2017 using the CIFAR_PI_DT method.

Method	F-measure		
	WT	TC	ET
CIFAR_PI_DT	0.79	0.63	0.60

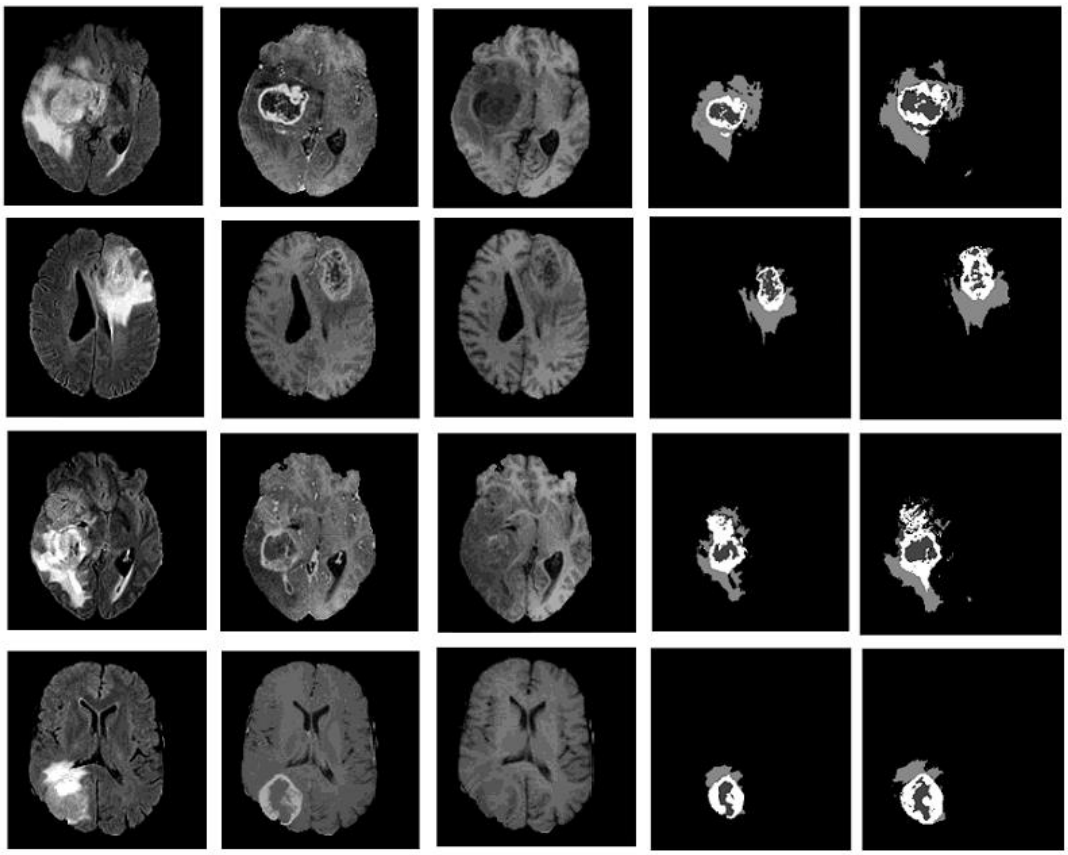

Figure 4-11: FLAIR, T1ce and T2 MRI models, ground truth and CIFAR _PI_DT segmentation masks (left to right).

The results in Figure 4-11 show that the CIFAR_PI_DT method slightly improved the F-measure for all areas (i.e. WT, TC and ET). Therefore, the prediction segmentation masks for the tumour region boundaries are much closer to ground truth. This happened because the CIFAR_PI_DT method does not consider local dependencies but considers only the normalized pixel intensity, which provides more global information.

4.4.3.4 CIFAR _PI_HIS_DT

Histogram-based texture features are considered in this scenario. As described in Section 4.3.3, the optimum parameters that were selected in this work were the number $K_{Cluster}$ and the fixed window, representing the neighbouring pixels. The reason for selecting the number $K_{Cluster} = 6$ was to consider the complexity and verity of the brain tissue intensities in MRI. Moreover, all the possible brain and tumour tissues (i.e. enhanced tumour, necrosis, oedema, WM, GM, and CSF) in the MRI had to should be

sufficiently separated and represented as ID by the cluster number. Finally, a fixed 9x9 window parameter was selected as part of the experiment.

Each quantized image was created by assigning a cluster number, which was generated by applying the threshold number to each pixel in the image. Then the histogram intensity of the centre pixel neighbourhood was calculated on the basis of the ID location in the quantized image of each corresponding MRI protocol. As described in Section 4.4.3.3, the same CIFAR feature and normalized pixel intensity feature settings were used, which were then combined with the histogram-based texture features. Then the corresponding features were treated as feature vectors and fed into the DT classifier. The DT classifier parameters selected in Section 4.3.5 were used. Table 4-5 provides the evaluation results obtained by applying CIFAR_PI_HIS_DT to the BRATS 2017 challenge dataset. Figure 4-12 shows the same examples of MRI modalities as in Figure 4-10 and Figure 4-11 in the brain tumour segmentation result images, but using the CIFAR _PI_HIS _DT method.

Table 4-5: Segmentation results on the split testing dataset from BRATS 2017 using the CIFAR _PI_HIS_DT method.

Method	F-measure		
	WT	TC	ET
CIFAR_PI_HIS _DT	0.84	0.66	0.64

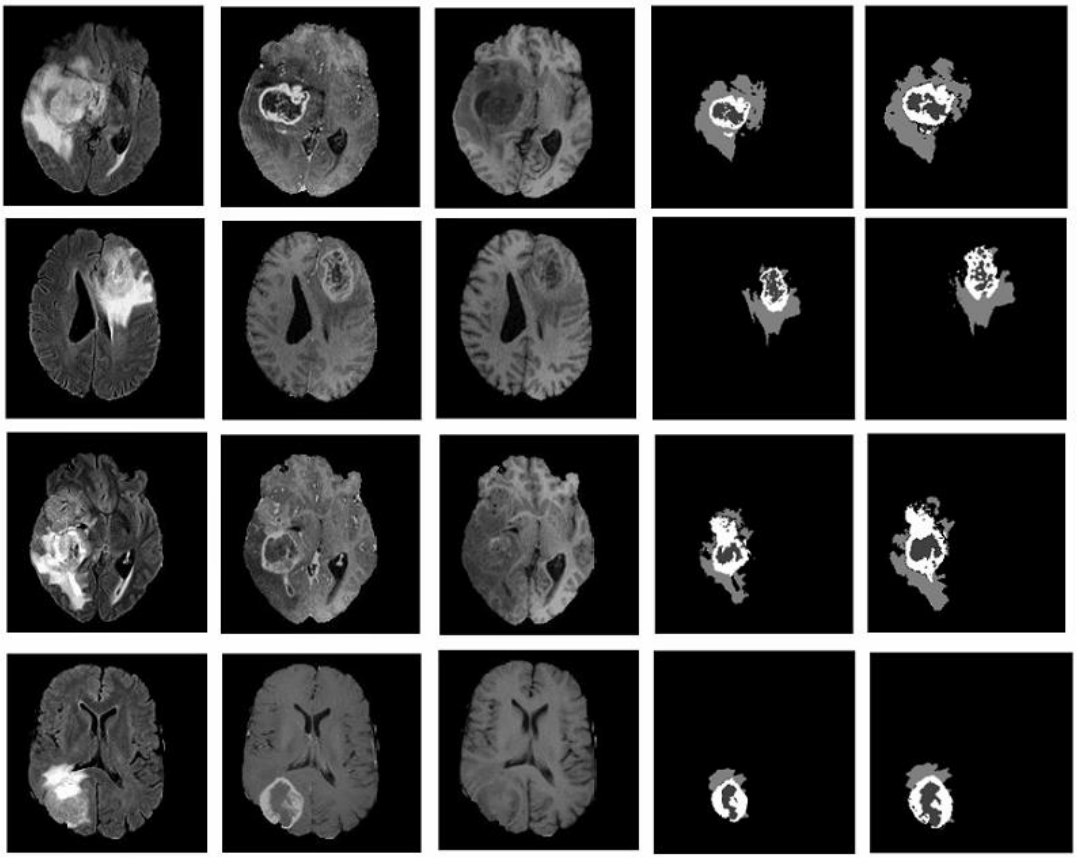

Figure 4-12: FLAIR, T1ce and T2 MRI models, ground truth and CIFAR PI_HIS_DT segmentation masks (left to right).

It can be seen in Table 4-5 that the histogram-based texture features significantly improved the F-measure for the complete, core and enhanced tumour. This was possible because the local dependences were achieved by adding the histogram-based texture features to the whole process.

4.5 Discussion

The publicly available BRATS2017 dataset was used in this study for training and testing the proposed models for brain tumour segmentation. The experiments show that the F-measure is not so good for segmentation if the CIFAR network only is used. This indicates that the CIFAR can segment the location of the tumour or the area that contains the tumour regions, but it cannot accurately detect or determine the exact tumour boundaries. There is a slight drop in the F-measure for the complete tumour and tumour core if the CIFAR machine learned features are sent to the DT classifier. This means that the CIFAR features can match more precisely with the deep learning classifier in the last layer than with the machine learning classifier (DT). The classifier layer in the CIFAR network perfectly interprets the deep learning features to predict the label of the specific pixel. Adding the pixel intensity to the process slightly improves the F-measure for all areas (CT, TC and ET). This implies that the prediction segment masks of the tumour's regional boundaries are much closer to the ground truth. However, the CIFAR_ PI _DT method does not consider the local dependencies. It considers only the normalized pixel intensity which provides more global information in its method. Adding the histogram-based texture features to the process significantly improves the F-measure for the complete tumour, the tumour core and the enhanced tumour. The reason behind this is that the local dependencies are achieved by adding histogram-based texture features to the whole process. Due to the small number of MRI examples in the training dataset, the CIFAR_PI _HIS_DT model was trained on a pretrained CIFAR and not from scratch. The original CIFAR was trained on the natural image dataset and this affected the size of the increase in the accuracy of the segmentation. The F-measures for all corresponding experiments are compared in Table 4-6. The results show that the F-measures of CIFAR_PI_HIS_DT for all tumour categories achieved the highest values, which were 0.84, 0.64 and 0.66, respectively. Meanwhile, CIFAR-DT presents the lowest F-measures for WT and TC, that is, 0.76 and 0.63, respectively. Additionally, it is clear from Table 4-7 that there is a significant improvement between some results of our methods in the brain tumour segmentation.

Table 4-6: Comparison of F-measures (mean and standard deviation) for our experiments separated into whole tumour, tumour core and enhancing tumour.

Methods	Case	F-measure		
		WT	TC	ET
CIFAR	Mean	0.76	0.63	0.58
	Standard deviation	0.28	0.42	0.54
CIFAR_DT	Mean	0.74	0.62	0.58
	Standard deviation	0.29	0.47	0.54
CIFAR_PI_DT	Mean	0.79	0.63	0.60
	Standard deviation	0.19	0.40	0.36
CIFAR_PI_HIS_DT	Mean	0.84	0.66	0.64
	Standard deviation	0.09	0.33	0.38

Table 4-7: Performance of P-values between our experiments for the brain tumour regions.

Methods	P-value		
	WT	TC	ET
CIFAR Vs CIFAR _DT	<0.05	<0.05	0.053
CIFAR _DT Vs CIFAR_PI_DT	<0.05	0.01	0.001
CIFAR_PI_DT Vs CIFAR_PI_HIS_DT	<0.05	0.001	0.022

We also compared our method with some state-of-the-art methods. Table 4-8 shows the comparison results. From this table we can see that our method performs moderately well, compared with the state-of-the-art methods. However, it should be mentioned that our model is based on an improved CIFAR network, which is the simplest of all the networks. Our model has fewer parameters and thus is faster than the other models. Additionally, in brain tumour segmentation methods, an F-measure performance of more than 0.83% is acceptable or useful from a clinical point of view for segmenting the tumour structure as a whole in a way which represents the brain tumour boundaries. Moreover, we can take a pretrained CIFAR model that has already learned to extract powerful and informative features from its brain tumour application and use it as a starting point to train a larger dataset or even to learn a new task, e.g., stroke lesion detection. This suggests that this model is quite robust to change. Regarding the comparison of times required by the various methods, we first illustrate the complexities of the network architecture because the more complex these architectures are, the more parameters they have and the more time they need for computation. The CIFAR network that we use consists of only 3 convolution-ReLU-MaxPooling blocks and 2 fully connected layers. Casamitjana's method (Casamitjana et al. 2018) uses two V-Nets, each of which consists of 21 convolution-PReLU blocks, 4 "Down" convolution layers and 4 "Up" convolution layers. Kamnitsas's method (Kamnitsas et al. 2018) uses ensembles of multiple models and architectures, which consist of two deepMedic models, three 3D FCNs, and two 3D versions of the U-Net architecture, in which U-Net has the same complexity as V-Net. And Wang's method (Wang et al. 2017) consists of 3 networks, each of which consists of 24 convolutions + batch normalization + PReLU and 4 convolution output channels. In comparing the architecture, we find that the complexity of the proposed scheme is significantly lower than other existing schemes. Bharath's method (Bharath et al. 2017) involves a superpixel-wise two-stage tumour tissue segmentation algorithm. Each stage consists of superpixel computation, with feature extraction based on multi-linear singular value decomposition on a tensor constructed from multimodal MRI data, and a random forest classifier. We cannot directly compare the time complexities of their method with those of ours on the basis of the architecture. However, as we understand it, the computation required in each step of Bharath's method is not small.

Table 4-8: Performance of our proposed method compared with other methods for BRATS 2017 dataset.

Methods	F-measure		
	WT	**TC**	**ET**
Kamnitsas et al. (2018)	0.88	0.78	0.72
Wang et al. (2017)	0.873	0.783	0.774
Casamitjana et al. (2018)	0.86	0.68	0.67
Bharath et al. (2017)	0.83	0.76	0.78
CIFAR_PI_HIS_ DT	0.84	0.66	0.64

4.6 Limitations

The first limitation of the proposed CIFAR_PI_HIS_DT method is its poor performance in the F-measure for the tumour core and enhanced tumour segmentation. Only a small number of training datasets of MRI examples on which to train the proposed model; therefore the CIFAR_PI_HIS _DT model was trained on a pre-trained CIFAR that was trained on the natural image dataset, which increased the accuracy of the segmentation. The idea was to initialise the network and achieve a perfect case by using a pre-trained CIFAR that had been trained on an actual dataset of brain MRI. In some cases of brain tumour, the MRI, CIFAR_PI_HIS _DT model failed to segment some small objects. For example, where a group of a few pixels was surrounded by a region of pixels of a different class, the model would label the pixels incorrectly. Figure 4-13 shows an example of such cases. Additionally, there is a difference in the performance of the segmentation accuracy results between the core and whole tumour structure because in some MRI modalities, the enhanced tumour appears as a hypo-intensity in some T1ce images. Therefore, the CIFAR_PI_HIS _DT model could not classify the pixels correctly but labelled them as oedema, which affected the accuracy of the core tumour

results. The promising results in the whole tumour region are due to the hyper-intensity of the oedema regions in the FLAIR and T2 images (see Figure 4-14).

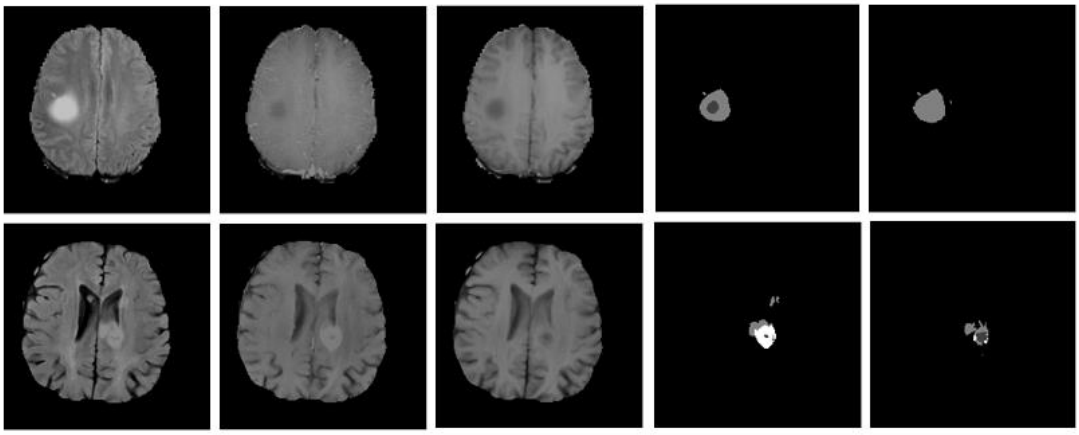

Figure 4-13: FLAIR, T1ce, T2, GT and Segmentation mask (left to right).

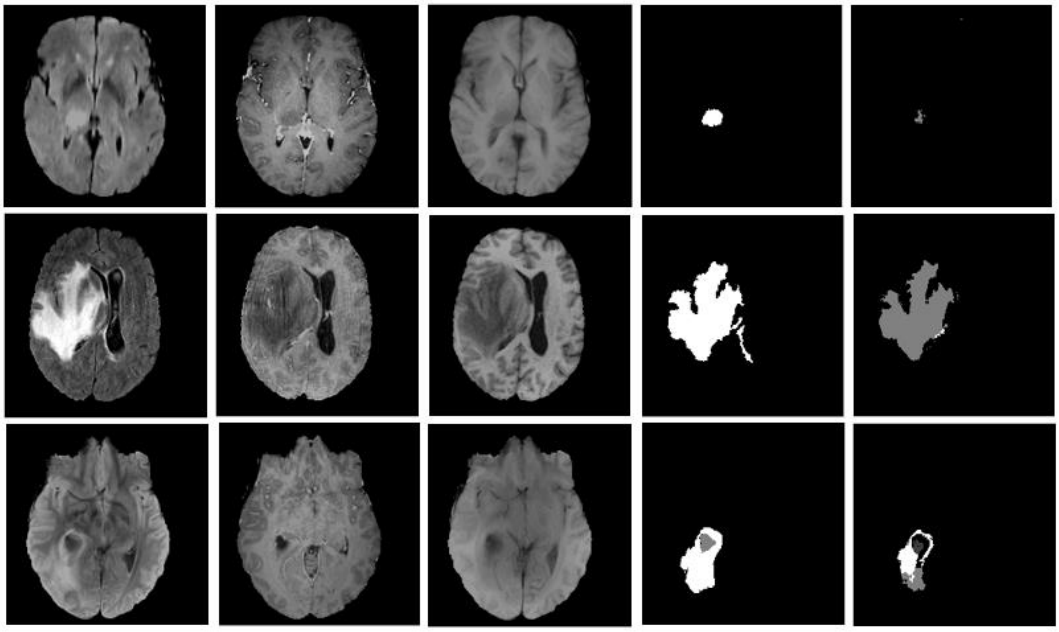

Figure 4-14: FLAIR, T1ce, T2, GT and Segmentation result (left to right).

The second limitation was that CIFAR_PI_HIS _DT needed two training steps, which was time consuming because the CIFAR and DT stages required tuned parameters and had to be trained separately.

4.7 Conclusion

As mentioned in Section 4.2.3, using the CIFAR network as a CNN classifier for brain tumour segmentation has some drawbacks (e.g. it incorrectly labels some of the tumour classes and it smooths the boundaries of the tumour regions in the segment results).This was the result of not considering correlation with the near pixels enough for classifying the pixels. To overcome this drawback, we combined ideas derived from the designed hand-crafted features, which are based on the histogram-based texture feature with the machine-learned features to compensate for the limitation in the local dependencies. The learned features were then applied to the DT to classify each pixel in the MRI images as normal brain tissue or one of the different parts of the tumour region (see Section 4.3.4). The tumour segmentation labels are oedema, necrosis, and enhanced tumour. The proposed model was evaluated on the BRATS 2017 dataset. The results of the experiment demonstrate the high segmentation performance of the F-measure, which is 0.84% for the whole tumour and average results of 0.66 % and 0.64% for the core and enhanced tumour regions, respectively.

Overall, the technique of combining the histogram-based texture features as hand-crafted features with the machine-learned features produces the best result (see Figure 4-12). It provides segment tumour masks that are close to experts' delineation across all the glioma grades, leading to faster brain tumour diagnosis and thus a faster treatment plan for the patients.

Chapter 5

Automated Brain Tumour Segmentation on a Multi-modal MR Image Using SegNet

5.1 Introduction

MRI is one of the most popular imaging techniques; it facilitates tumour analysis by visualizing the spread of the tumour. It also gives soft tissue contrast compared to other techniques, such as CT and PET. Moreover, multi-modal MRI protocols are commonly used to evaluate brain tumour tissues because they are able to separate different tissues using a specific sequence based on the properties of the tissue. For example, T1-weighted images clearly separate healthy tissues in the brain. Meanwhile, T1ce (contrast enhanced) helps to separate tumour boundaries, which appear brighter because of the contrast agent. The oedema around tumours can be detected easily in T2-weighted images, while FLAIR images are best for differentiating oedema regions from cerebrospinal fluid (Juan-Albarracín et al. 2015; Bauer et al. 2013). Recently, convolutional neural networks have attracted attention for their power to detect and segment objects and classify images. Most CNN-based methods in the BRATS challenge are patch-wise models (Havaei et al. 2017; Pereira et al. 2016). These methods take only a small region as an input to the network, which disregards the image content and label correlations. This limitation is addressed in Chapter 4, below, by incorporating more information from the local pixel dependencies (i.e. hand-crafted features which represent histogram-based texture features) and fusing them with CNN-based features. However, training in this method takes a long time. Furthermore, in fully convolutional networks (FCN) the CNN architecture can be modified in several ways. Specifically, instead of making probability distributions prediction patch-wise in CNN, FCN models predict one probability distribution pixel-wise (Long et al. 2015). In Ronneberger et al. (2015), several MRI modalities are stacked together as different input channels into deep learning models. However, the correlation between several MRI modalities is not explicitly considered. To overcome this problem, we have developed a feature fusion method to select the most effective information from different modalities. We also propose a model to deal with multiple MRI modalities separately, and we then incorporate spatial and sequential features from them for 3D brain tumour segmentation.

In this study, we first trained four SegNet models with 3D datasets, using Flair, T1, T1ce, and T2 modalities as input data. The outputs of each SegNet model are four feature maps, which represent the scores of each pixel and can be classified as background, oedema, enhanced tumour, and necrosis. The highest scores in the same

class from the four SegNet models are extracted and the four feature maps with the highest scores are obtained. These feature maps are combined with the pixel values of the original MRI models, and are taken as the input to a DT classifier to further classify each pixel. Our results demonstrate that this proposed strategy can perform fully automatic segmentation of tumour and sub-tumour regions.

The main contributions of this chapter are reports on the following:

• A brain tumour segmentation method that uses 3D data information from the neighbours of the slice in question to increase segmentation accuracy for single mode MR images.

• The effective combination of features extracted from multi-modal MR images, which maximises the useful information from the various modalities of MR images.

• A decision tree-based segmentation method that incorporates features and pixel intensities from multi-modal MRI images, which gives higher segmentation accuracy than single-modal MR images.

• Evaluation of the BRAT2017 dataset, showing that the proposed method gives state-of-the-art results.

5.2 SegNet_ Max_DT Method

The brain tumour segmentation algorithm aims to locate the entire bulk of the tumour and then accurately segment it into four sub-tumour parts. The proposed segmentation method consists of five main steps: the pre-processing step; 3D MRI datasets construction step; the training step, which fine-tunes a pre-trained SegNet for each MRI modality separately; the post-processing step, which extracts four maximum feature maps from the score maps of the SegNet models'; and the classification step, which determines the type of each pixel based on the maximum feature maps and the MRI pixel values. Figure 5-1 shows the whole pipeline of the system proposed in this chapter using SegNet networks.

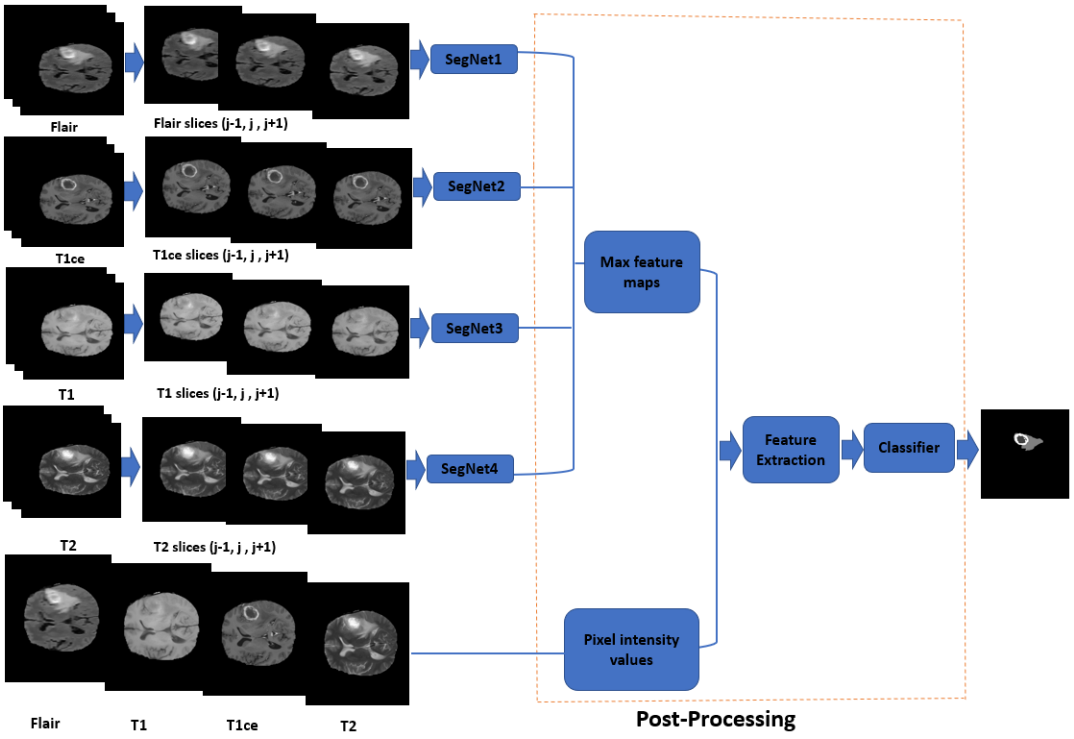

Figure 5-1: Pipeline of the brain tumour segmentation.

5.2.1 Data Pre-processing

The procedure that has been used in this section is similar to the procedure that is described in Section 4.3.1. Additionally, to remove a significant portion of unnecessary zeros in the dataset and to save training time, by reducing the huge memory requirements for 3D datasets, some black parts from the data of all MRI modalities were trimmed to get input images of size 192×192 because at this size the location of the brain tissues can be fitted in the centre of the image with equal borders and without losing information.

5.2.2 3D MRI Database Generation

The main step in this proposed method is to construct a 3D database. Because there are four distinct modalities in the MRI dataset for each patient, we took them as four independent inputs. In processing the j^{th} slice, we also used the $(j-1)^{th}$ and $(j+1)^{th}$ slices to take advantage of 3D image information. Consequently, the three adjacent slices for each modality were taken as three colour channels of an image and are treated as 3D inputs. In the training process, the ground truth for the central slice (j^{th}) was take as the label for each input 3D image because the ground truth of the central slice (j^{th}) is close to the ground truths of the $(j-1)^{th}$ and $(j+1)^{th}$ slices. Figure 5-2 shows the combination of the MRI slices for 3D database generation.

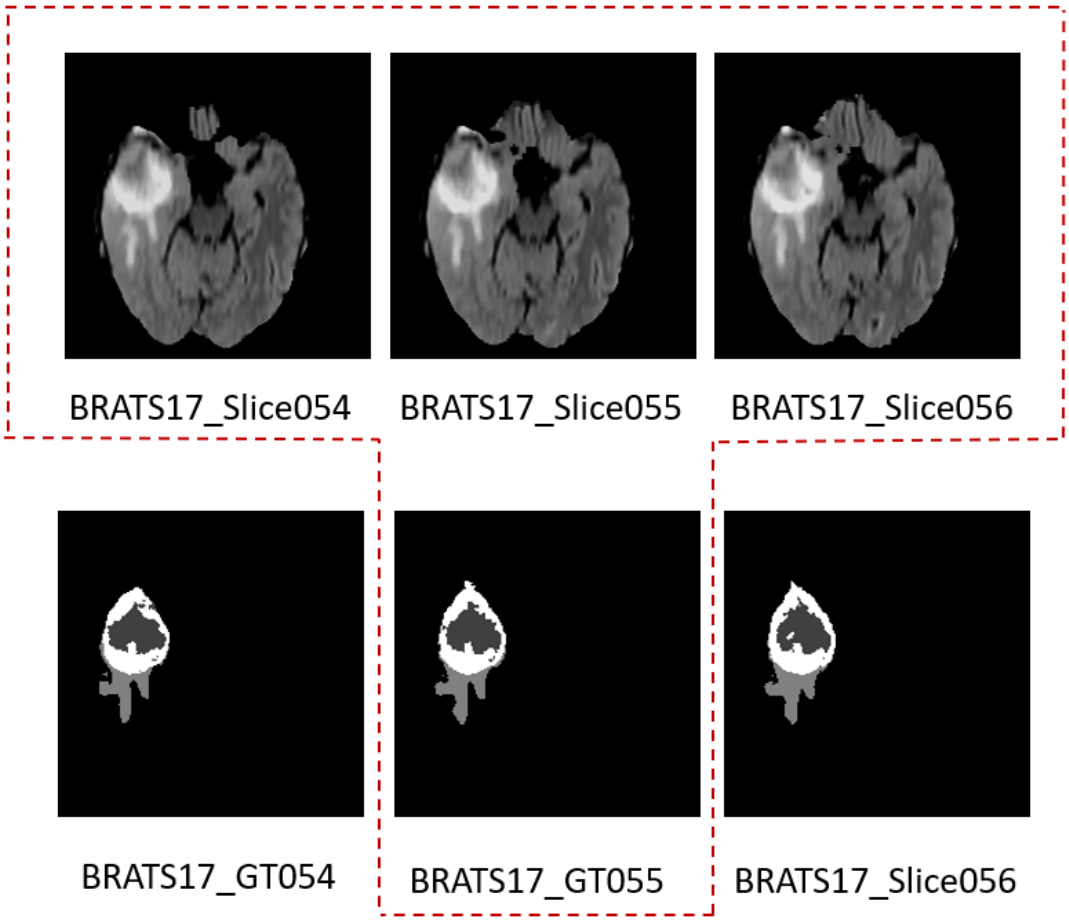

Figure 5-2: Some examples of brain tumour slices compared with their ground truth.

5.2.3 SegNet Model Architecture

In our network architecture (i.e. SegNet), the main idea from FCN was to change the fully connected layers of VGG-16 into convolutional layers. This not only helped to retain higher resolution feature maps at the deepest encoder output but also significantly reduced the number of parameters in the SegNet encoder network and enabled a classification net to get an output as a dense feature map while keeping the spatial information (Badrinarayanan et al. 2017).

The SegNet architecture consisted of a down sampling (encoding) path and a corresponding up sampling (decoding) path, followed by a final pixel-wise classification layer. In the encoder path were 13 convolutional layers, which matched the first 13 convolutional layers in the VGG16 network. Each encoder layer had a

corresponding decoder layer; therefore, the decoder network also had 13 convolutional layers. The output of the final decoder layer was fed into a multi-class soft-max classifier to produce independent class probabilities for each pixel. The encoder path consisted of five convolution blocks, each of which was followed by a max-pooling operation with a 2×2 window and stride 2 for down sampling. Each convolution block was constructed as several layers of 3×3 convolution, combined with batch normalization and elementwise rectified linear non-linearity (ReLU). There were two layers in each of the first two convolution blocks, and three layers for the next three blocks. The decoder path had a symmetric structure leading to the encoder path, except that the max-pooling operation was replaced by a up sampling operation. Up sampling takes the outputs of the previous layer and the output of the max pooling indices of the corresponding encoding layer as input. The output of the final decoder, which is a high dimensional feature representation, was fed to a soft-max classifier layer that classified each pixel independently (see Figure 5-3). Consequently, the output of the soft-max classifier is a K channel image (K represents the number of desired classes) with a probability value at each pixel.

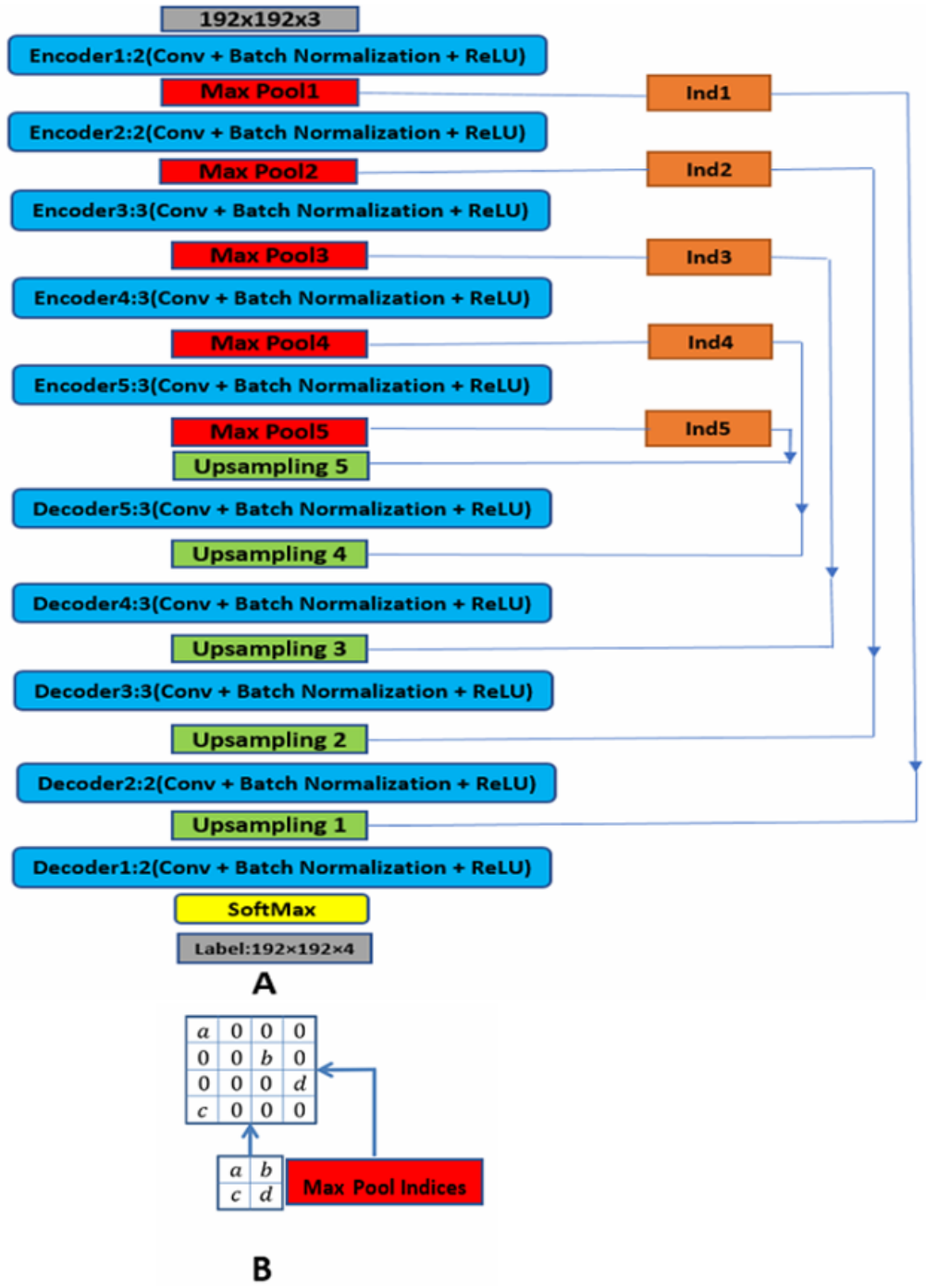

Figure 5-3: (A) Architecture of the SegNet, (B) The SegNet which uses the max pooling indices to up-sample the feature maps and convolves with a trainable decoder filter bank (Badrinarayanan et al. 2017).

5.2.3.1 Segmenting the Brain Tumour Image with the SegNet Network

The semantic segmentation model in Figure 5-3 took full-size images end-to-end as inputs for feature extraction. As discussed in Section 4.2.2, the pretrained network that had already learned to extract powerful and informative features from natural images could be used again as an initial point for learning a new task. Additionally, using a pretrained network with transfer learning is typically much faster and easier than training a network from scratch. Therefore, the pretrained semantic segmentation network (SegNet) was downloaded and employed in our method. This network was pretrained for segmenting 11 classes using the CamVid dataset (Brostow et al. 2009), a collection of images containing street-level views obtained while driving. The parameters of the pretrained SegNet are finely tuned using images with manually annotated brain tumour regions. In the testing process, the final SegNet model was used to create predicted segmentation masks of the tumorous regions for unidentified images. The reason that the SegNet network was used instead of other deep learning networks is that SegNet has few parameters, and so does not need the high computational resources required by DeconvNet (Noh et al. 2015), for example, and it is easier to train end-to-end. Moreover, in the U-Net network (Ronneberger et al. 2015), all the feature maps in the encoders are transferred to the corresponding up-sampling decoders and concatenated to the decoder feature maps, which requires considerable memory. In SegNet, however, only pooling indices are reused, which requires less memory.

The proposed method (Brain SegNet) that developed by Hu et al (2020) is involved SegNet network for brain lesion segmentation. The input to this network is multi-modality 3D MRI volume data (MRI modalities are staked together) while in our method (SegNet_Max_DT), we used 4 SegNet networks for each MRI modality. Brain SegNet has four convolutional blocks, and contains 17 convolutional layers in total, with residual units while our SegNet network has five convolutional blocks with 13 convolutional layers. Brain SegNet includes a refinement module capable of aggregating rich fine-scale 3D volume features over multiple convolutional blocks. In our method, maximum features fusion method was employed to select the most informative and powerful features from different MRI modalities for brain tumour segmentation.

5.2.4 Post-processing

Two main steps of post-processing are described in this section.

A- Selecting maximum features

As described in Section 5.2.3.1, four SegNet models were adapted and trained separately to segment a brain tumour in multimodal MR images. The four trained networks learned to identify useful features, often with one feature per channel. The earlier layers of SegNet models learned simple features, such as circles and edges, while the deeper layers learned complex, useful features, which were finer. The machine-learned features in the last deconvolution layer in each SegNet model represented four score maps, which were related to the four classification labels (i.e. background, necrosis, oedema, and enhanced tumour). Then each of the same specific classification labels in each SegNet model was grouped together in the score map to find the highest score map of them all. Finally, the four highest score maps were constructed from the 16 feature maps obtained. The values of each highest activation feature map represented the strong features that included all of the hierarchical features (at higher resolution), which helped to improve the classification performance. This process was undertaken to consider the correlations between the various MRI modalities by finding only the strong features between them and ignoring the redundant features that might have caused errors in the classification process. The selection process of the highest feature maps and their location in the SegNet architectures is illustrated in Figure 5-4.

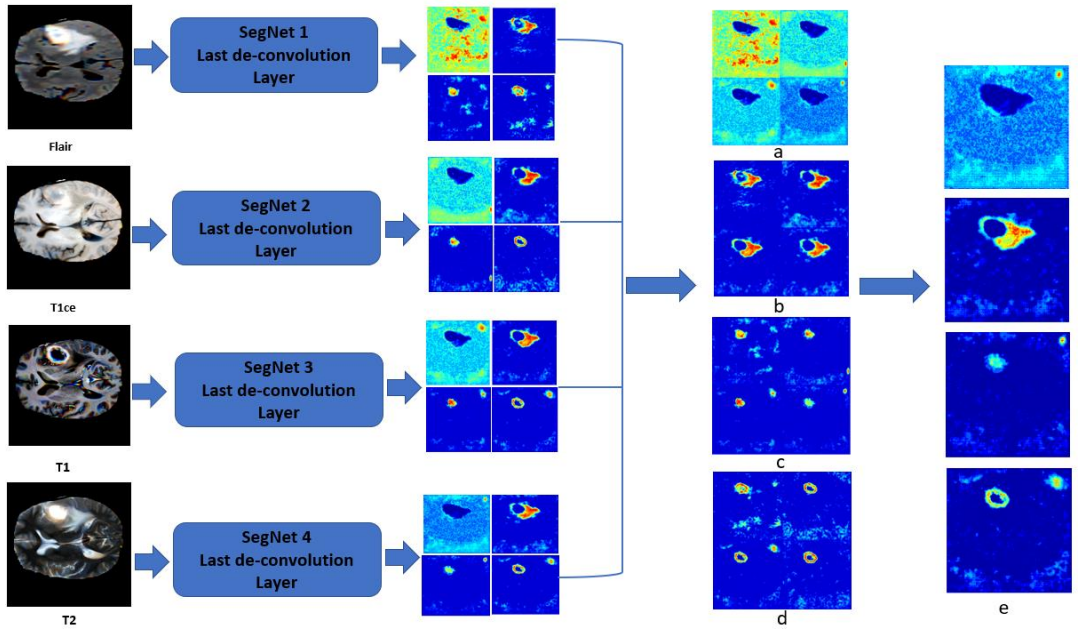

Figure 5-4: Selection process of maximum feature maps, (a), (b), (c) and (d), the background, oedema, enhanced tumour and necrosis groups, respectively. (e) Maximum feature maps.

B- Combined Selected Features

To further increase the information for classification, a feature vector was generated based on a combination of the four highest score maps and the pixel intensity values of the original MRI modalities (see Figure 5-5).

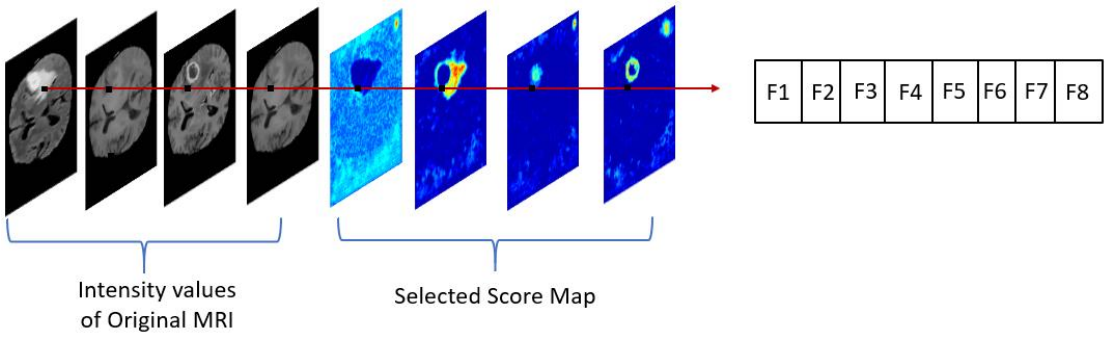

Figure 5-5: Combined features

Finally, the encoded feature vector was applied to a DT classifier to divide all the MRI image pixels into tumour and sub-tumour parts.

5.2.5 DT and Segmentation

Each pixel within the brain region was considered for classification. As described above, the four highest score maps were combined with pixel intensity values and considered as feature vectors. The feature vectors were then presented to a DT classifier. In this phase, the maximum number of splits or branch points was specified to control the depth of the designed tree. Various tree depths of the DT classifier were examined and tuned on the training datasets. Optimal generalisation and accuracy were obtained from a tree with depth 100. Meanwhile, 25% of the data was chosen for use as a testing set to determine the effects of D_{tree} by evaluating how accurate the classification was. The DT classifier was trained in the four labels (i.e. background, oedema, necrosis, and enhanced tumour). In the testing phase, the trained classifier was applied, and the appropriate labels were assigned to each pixel in the brain area. The predicted mask was then generated by mapping back each pixel class to the volume of the segmentation mask.

5.3 Experimental Results

The evaluation for this section is similar to the evaluation in Section 4.4.2, which was based on the BRATS 2017 testing dataset. The proposed algorithm was implemented using MATLAB 2018a and run on a PC with an Intel Core i7 CPU with 16 GB RAM using Windows 7. Our implementation was based on the MATLAB deep learning toolbox for semantic segmentation and its classification learner toolbox was used to train the DT classifier. The whole training process for each model took approximately 3 days on a single NVIDIA GPU Titan XP.

In this section, three main scenarios of qualified experiments were considered in order to evaluate the performance of the proposed method, as follows:

1- Single Slice Model

   In this experiment, the slices of each MRI modality (FLAIR, T1, T1ce and T2) were directly applied to the SegNet network to train and evaluate each model (i.e. SegNet1_Flair, SegNet2-T1ce, SegNet3_T1 and SegNet4-T2).

2- Joint Multi-slices Model

This experiment was designed to evaluate the effect of the 3D data construction of each MRI modality on the four models (SegNet1_Flair, SegNet2-T1ce, SegNet3_T1 and SegNet4-T2); that is, taking the three adjacent slices (j-1, j, j+1) of the same MRI modality together as an input to the SegNet network

3- SegNet_Max_DT Model

The third experiment was designed to evaluate the effect of adding the information that comes from selecting the highest features from all the trained models (SegNet1_Flair, SegNet2-T1ce, SegNet3_T1 and SegNet4-T2) with the pixel intensity of the original MRI modalities to the pipeline of the proposed segmentation model. In total, eight features were extracted from the corresponding MRI protocols. DT classification was performed in this experiment to classify each pixel as normal brain tissue or coming from a sub-tumour region.

5.3.1 Single Slice Model

Table 5-1 shows the accuracy results of the F-measure in the three tumorous regions (whole tumour, tumour core and enhanced tumour), considering single slices of MRI modalities as inputs to the each of the four SegNet models. Figure 5-6 demonstrates some visual images of these results for brain tumour segmentation.

Table 5-1: Segmentation results for the BRATS2017 data using single slices as an input to the four SegNet models.

Method	F-measure		
	WT	**TC**	**ET**
SegNet1-Flair	0.79	0.77	0.77
SegNet2-T1ce	0.71	0.70	0.70
SegNet3-T1	0.73	0.64	0.65
SegNet4-T2	0.75	0.73	0.66

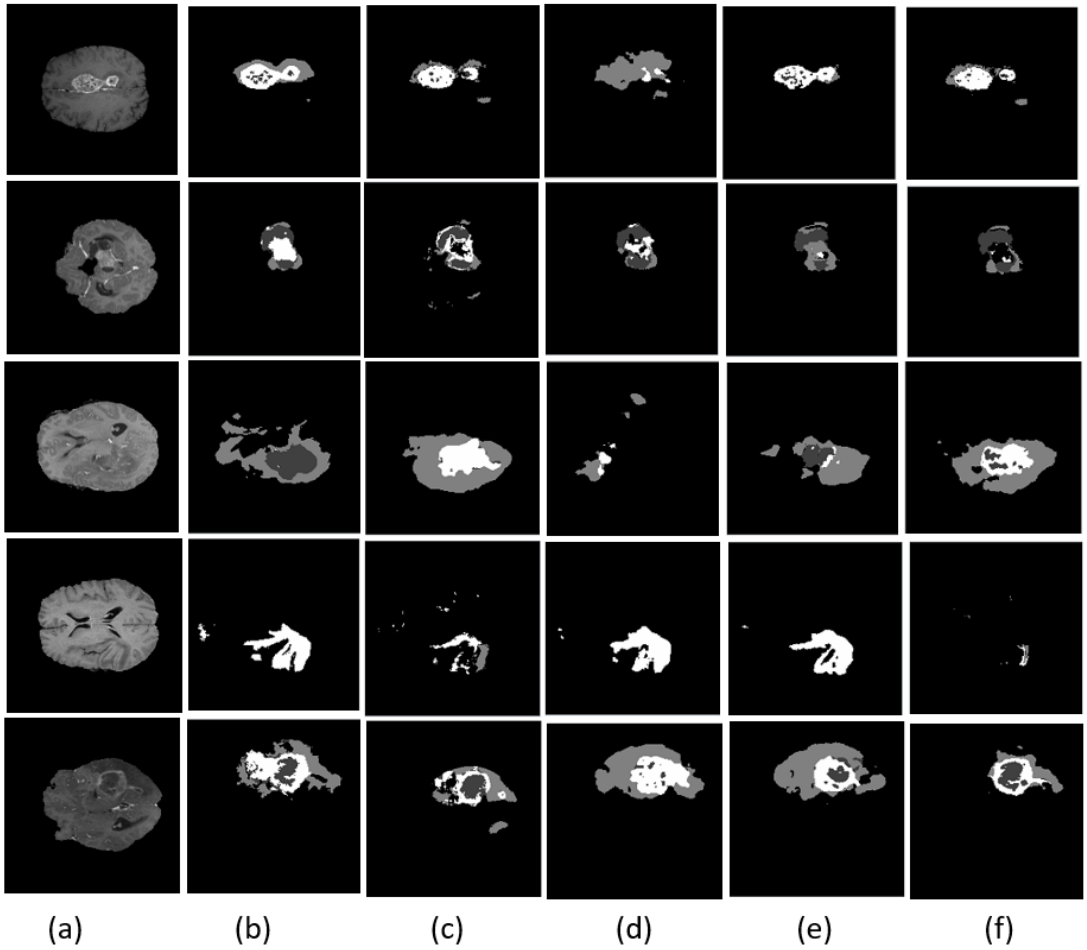

Figure 5-6: Segmentation results of SegNet models using single slices of each MRI modality: a, b, c, d, e and f corresponding to MRI slices, ground truth, SegNet1 Flair, SegNet2 T1, SegNet3 T1ce and SegNet4 T2, respectively.

5.3.2 Joint Multi-slices Model Results

Table 5-2 provides the evaluation results obtained by applying the SegNet segmentation model to each MRI modality with regard to the 3D dataset construction of the BRATS 2017 dataset. Figure 5-7 demonstrates some examples of segmented tumour parts in the same patient samples as in Figure 5-6.

Table 5-2: Segmentation results of Four SegNet models considering 3D information of BRATS 2017 dataset.

Method	F-measure		
	WT	**TC**	**ET**
SegNet1-Flair	0.81	0.81	0.78
SegNet2-T1ce	0.83	0.80	0.78
SegNet3-T1	0.80	0.80	0.77
SegNet4-T2	0.81	0.80	0.76

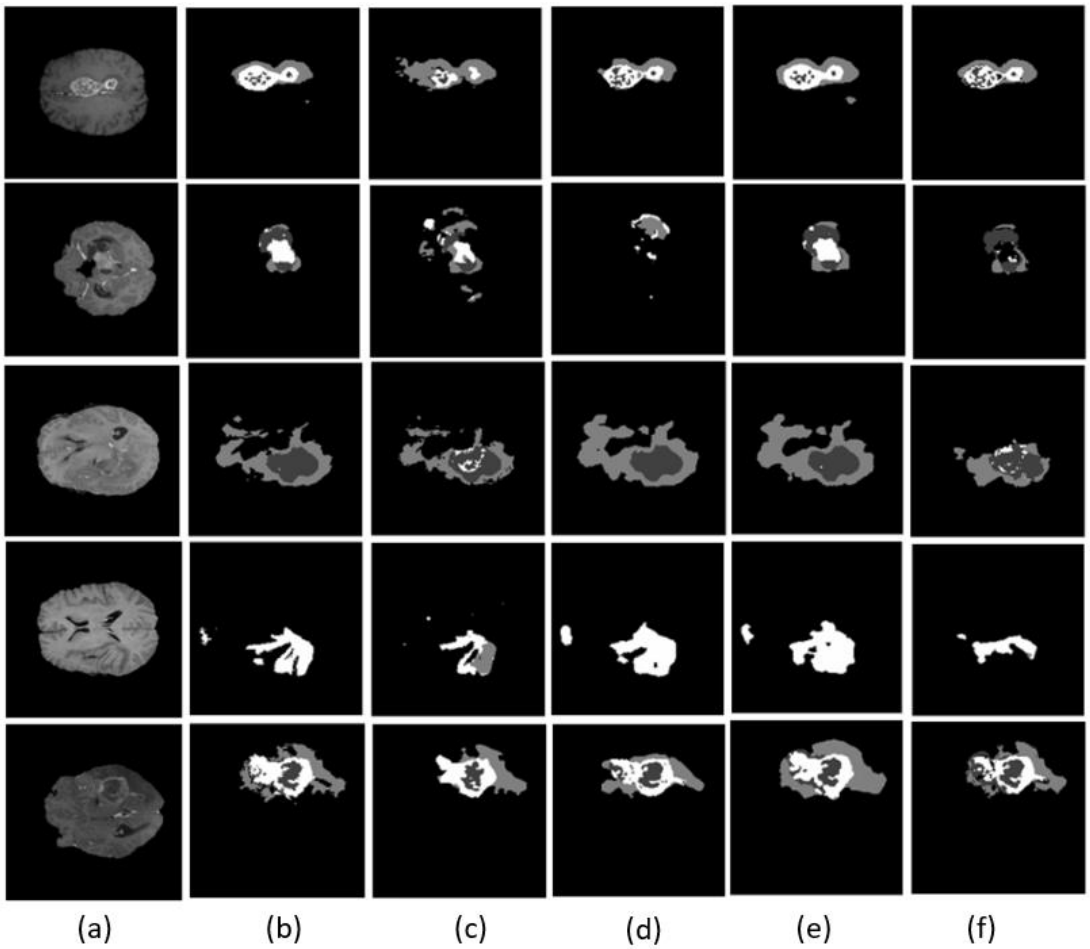

Figure 5-7: Segmentation results of SegNet models on the 3D dataset of each MRI modality, a, b, c, d, e and f, corresponding to MRI slices, ground truth, SegNet1 Flair, SegNet2 T1, SegNet3 T1ce and SegNet4 T2, respectively.

5.3.3 SegNet_Max_DT Model

In this comparison of the results of the experiments in Sections 5.3.1 and 5.3.2, it will be seen that more accurate results were obtained when the fourth-trained SegNet models were based on 3D data information as input. Therefore, these four-times-trained models were considered in this scenario so as to extract and incorporate their highest features and to combine them with the pixel intensities of the original MRI protocols. Then these combined features were fed into the DT classifier to classify the different parts of brain tissue. The evaluation results are summarised in Table 5-3, while some visual results from the semantic segmentation structures of SegNet models and Seg_Max_DT method from the axial view are shown in Figure 5-8.

Table 5-3: Segmentation results using SegNet_Max_DT in the proposed method

Method	F-measure		
	WT	TC	ET
SegNet_Max_DT	0.85	0.81	0.79

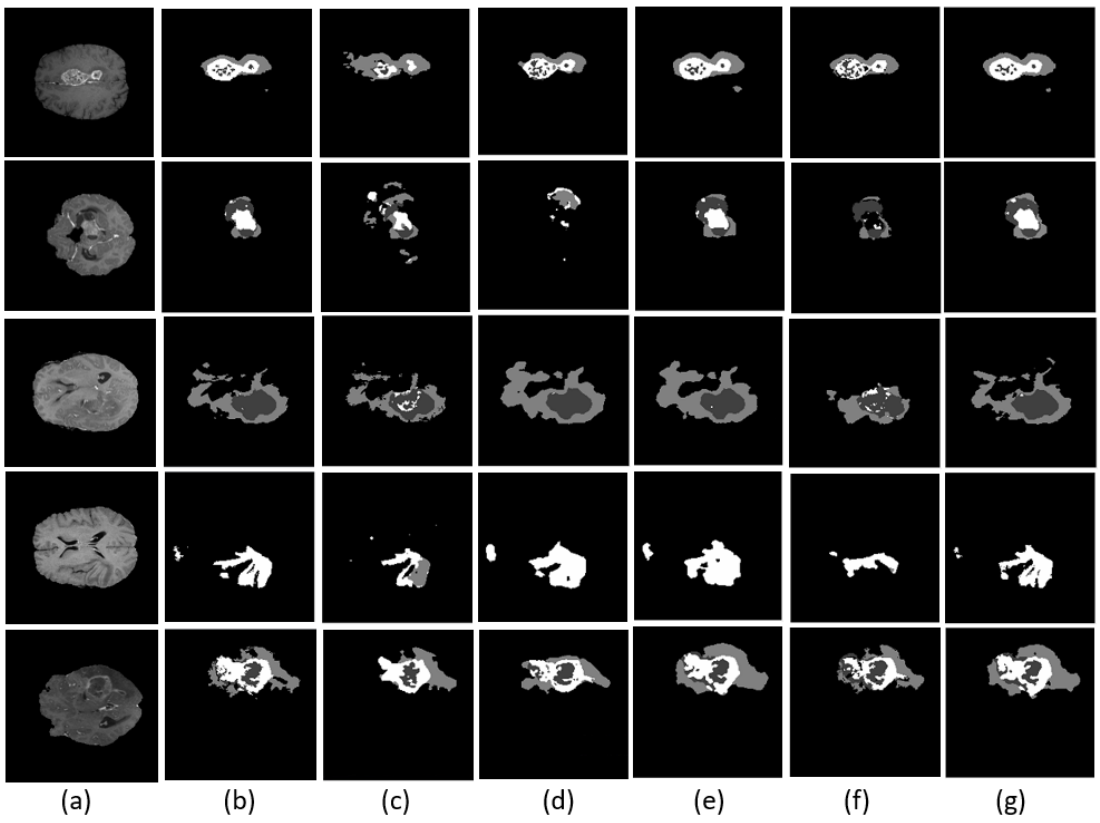

Figure 5-8: Segmentation results of SegNet models and SegNet DT method. a, b, c, d, e, f and g representing MRI slices, Ground truth, SegNet1 flair, SegNet2 t1, SegNet3 t1ce, SegNet4 t2 and SegNet _Max_ DT, respectively.

5.4 Discussion

In our results, we observed that our 3D model can accurately detect a brain tumour, even though we only trained each MRI modality separately and did not follow other studies that combined the four MRI modalities as input. The high degree of accuracy comes from the fact that the network architecture can capture fine 3D details of tumorous regions from adjacent MRI slices (j − 1, j, j + 1) of the same modality. Consequently, the convolutional layers can extract more features, which is extremely helpful in improving the performance of brain tumour segmentation. Moreover, our brain tumour segmentation was relatively accurate because it extracted the four highest feature maps, combined with the pixel intensity values of the original MRI images. The score maps were obtained from the last deconvolution layer in each SegNet model because this layer includes all the hierarchical features that contain finer details (at higher resolution), which gives accurate brain tumour detection results. Table 5-4 presents the evaluation results for the proposed methods in this chapter on the BRATS 2017 training dataset for the four MRI modalities. From Table 5-4, SegNet _Max_ DT performs better than individual SegNet models. As noted in Section 5.2.4, only the highest scores (strongest features) for each specific sub-tumour region were selected for classification, which is why we can obtain most accurate results from using SegNet_ Max _DT.

Table 5-4: Comparison of F-measure (mean and standard deviation) for our experiments separated to show whole tumour, tumour core and enhanced tumour results.

Methods		F-measure		
		WT	TC	ET
SegNet1-Flair	Mean	0.81	0.81	0.78
	Standard deviation	0.17	0.20	0.30
SegNet2-T1ce	Mean	0.83	0.80	0.78
	Standard deviation	0.21	0.16	0.26
SegNet3-T1	Mean	0.80	0.80	0.77
	Standard deviation	0.27	0.29	0.26
	Mean	0.81	0.80	0.76

SegNet4-T2	Standard deviation	0.19	0.26	0.36
SegNet_Max_DT	Mean	0.85	0.81	0.79
	Standard deviation	0.06	0.07	0.19

Table 5-5 shows that our method gives better results in core and enhanced tumour segmentation. As a whole, however, the accuracy of our complete segmentation is not better than that of Kamnitsas et al. (2018) and Casamitjana et al. (2018) because our method had relatively low accuracy in detecting oedema. Nonetheless, we considered the core or enhanced regions, which are much more important than the oedema region. We believe that it is worth sacrificing the accuracy of oedema detection if it means increasing the accuracy of detecting the core and enhanced tumour.

Table 5-5: Performance of our proposed method compared with other methods on BRATS 2017.

Method	**F-measure**		
	WT	**TC**	**ET**
Kamnitsas et al. (2018)	0.88	0.78	0.72
Casamitjana et al. (2018)	0.86	0.68	0.67
Bharath et al. (2017)	0.83	0.76	0.78
SegNet _Max_ DT	0.85	0.81	0.79

5.5 Conclusion

This study used the publicly available BRATS 2017 dataset. A DT and four SegNet models were trained with the same training dataset, which included ground truth. A testing dataset without ground truth was used to evaluate the system. Our experiments show that the SegNet architectures with 3D dataset and post-processing presented in this work can efficiently and automatically segment brain tumours, completing segmentation for an entire volume in four seconds on a GPU optimized workstation. However, some models (e.g. SegNet3 T1 and SegNet4 T2) do not give accurate results because T1 and T2 MRI modalities give only information related to healthy and whole tumour tissues but not other sub-parts of the tumour, such as necrosis and enhanced tumour. To tackle this problem, maximum feature maps from all SegNet models were combined, so that only strong and useful features from all the SegNet models were presented to the classifier. Four MRI modalities were trained separately for the following reasons. First, different modalities have different features, so we need to understand the effect of the features in each MRI modality or which features could increase the segmentation performance, and it is faster to train different simple models than to use one complex model. Second, specific features can be extracted that are directly related to the specific modality of each SegNet model, providing clinicians with specific information. Finally, one of the most common MRI limitations is the prolonged scan time required to get the various MRI modalities. Consequently, depending on a single modality to detect a brain tumour can be a good way of saving time in clinical applications. Although the training stage in the proposed method is time-consuming, which could be considered a limitation, the prediction phase rapidly processes the testing dataset to provide semantic segmentation and classification. While our method can segment core and enhanced tumours better than state-of-the-art methods, it is no better at segmenting complete tumours. However, further post-processing techniques could improve the accuracy of our method. In addition, the SegNet models could be saved as trained models and refined by using additional training datasets. Consequently, a longitudinal study using a range of FCN and CNN architectures should be used over time to improve the performance of the proposed system.

Chapter 6

Texture Feature of the ROI for Brain Tumour Segmentation

6.1 Introduction

As described in Chapter 2, the specific appearances of healthy or tumour brain tissues are presented in each MRI sequence. Combining all the MRI modalities helps to accurately segment a brain tumour. In Chapter 5, an automated method was proposed that used all of the information of the MRI modalities (i.e. FLAIR, T1, T1ce and T2). In this method, each pixel was considered in the 3D image. However, selecting only the region of interest (ROI), which represents only the extensions of complete tumour structures as input data and suppresses the intensity of other, irrelevant, areas, helps to reduce the computational complexity of the model, thanks to the reduced amount of data and smaller features. Additionally, enhanced tumour segmentation is very important because it is related to the effective region (cancer cells). However, the delineation of the tumour boundary (whole tumour) and the assessment of its size are preliminary steps in segmenting the class of the tumour.

Recently, many deep learning approaches have been suggested to provide more dense predictions at the pixel level. A recent network is SegNet, which was described in detail in Chapter 5. The output layer of the SegNet network provides feature maps of the same size as the input image. These feature maps are considered to be machine-learned features, which are generated from the local and global image information. As discussed in Chapter 1, the biggest challenge in brain tumour segmentation is to develop an effective method to accurately segment different sub-tumour structures, which are characterized by complexity, less regularity (especially in the number of classes), and seem to have a varied texture and shape. However, using a method that is based on deep learning only is insufficient for performing an accurate segmentation of the brain tumour region. The limitation is that the local features related to the changes of the texture tissue due to tumour growth are not sufficiently considered in the SegNet based approach (Alqazzaz et al. 2019). Meanwhile, some hand-crafted feature extraction methods take into account the local dependencies of the pixel classes, such as grey-level co-occurrence matrix (GLCM)-based texture features (Lai et al. 2011). The GLCM is perhaps the most popular texture-based method for MR images (Holli et al. 2010).

This chapter aims to develop a hybrid method arising from the need for highly accurate segmentation. We have proposed a new learning-based method that combines machine-learned features and hand-crafted features for the automated segmentation of brain

tumour structures from the ROI images generated from the MRI dataset. The machine-learned features are score maps that are extracted from the de-convolution layer in the trained SegNet network, while the hand-crafted features are the GLCM-based texture features.

The contributions reported in this chapter are as follows:

- An automatic method to generate a ROI segment, which is in agreement with experts' delineation across all grades of glioma, by using a single commonly used MRI protocol (i.e. FLAIR) as input data.

- A DT classifier is applied only to the pixels that are considered as the tissues of ROI, which helps to reduce the computational cost through reducing the data size for classification.

- A novel method developed to overcome the limitation of the SegNet network and improve the detection of oedema, necrosis and enhanced brain tumour regions by combining hand-crafted features with machine-learned features.

- A reduced number of detected classes, which helps to increase the performance accuracy of the machine learning (SegNet network and DT classifier).

- A new method of brain tumour segmentation through the connection between a 2labels mask (binary mask) and a 3labels mask, which increases the accuracy of the proposed method in distinguishing the tumour core and the active tumour regions.

6.2 The SegNet_GLCM_DT Method

In this section, the details of the proposed method are discussed; they involve the detection of tumour structures and extraction of the features from ROI for classification.

6.2.1 Overview of the Segmentation Method

The proposed segmentation method has four main stages: pre-processing, finding images of the region of interest, extracting features and classifying them. In the first stage, pre-processing analysis is used to prepare the data for the main parts of the method through the standard intensity ranges of MR images, to enhance the classification accuracy. Then the initial ROI is identified by choosing a single MRI modality, which is implemented on the SegNet model and gives a highly accurate performance. After generating a ROI that considers only the tumour boundary structure, the features for each pixel are extracted in the ROI using a SegNet model as machine-learned features and grey level co-occurrence matrix (GLCM) as hand-crafted features for texture analysis. Finally, the combined features are fed into the DT classifier to label the pixels to the corresponding tissues. The whole pipeline of the proposed method is illustrated in Figure 6-1 and termed the SegNet_GLCM_DT method.

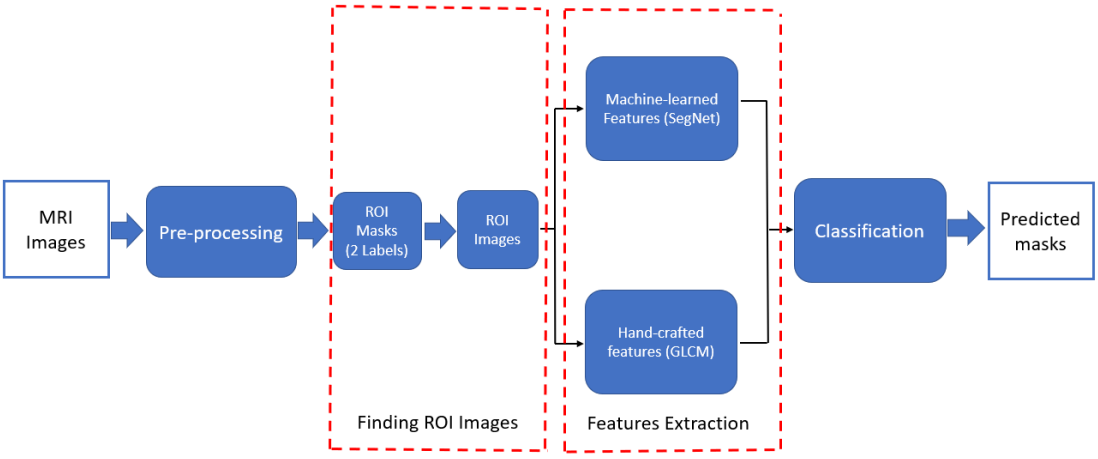

Figure 6-1: The workflow of the proposed segmentation method.

6.2.2 Pre-processing

The procedure that is used in this section is identical to the procedure that was described in Section 4.3.1.

6.2.3 ROI Masks

Management in terms of radiation dose planning and monitoring treatment response comes from an accurate detection of the extent and structure of the tumour. Additionally, a delineation of the size of the tumour, which is considered the ROI, is important for assessing the growth of glioma grades and for extracting imaging features from abnormal regions for tumour classification (Niyazi et al. 2016).

In this chapter, the initial ROI was identified using a semantic segmentation network, which is a SegNet model. The pre-trained SegNet model was modified to train each MRI modality separately for binary segmentation (normal and abnormal tissues). In an important step, ground truth masks were prepared for binary segmentation (see Figure 6-2).

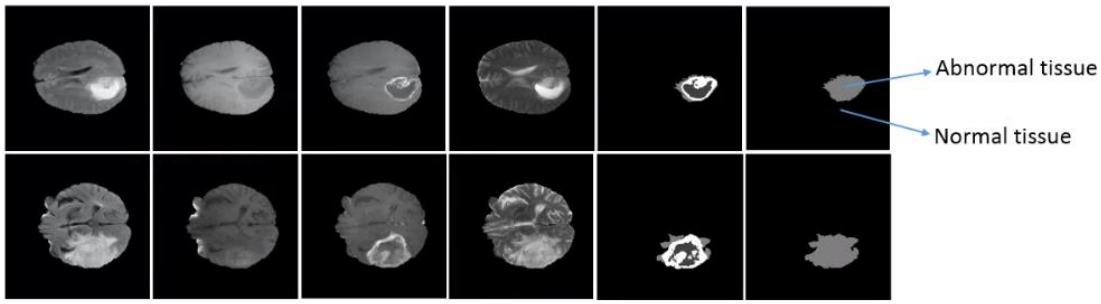

Figure 6-2: FLAIR, T1, T1ce and T2 MRI modalities, ground truth with four classes and ground truth with two classes (left to right).

6.2.3.1 Modality Selection for ROI Mask Generation

A- Experiment Setting

This section presents the results of calculating the initial creating ROI method. First, the dataset is outlined, followed by a description of the parameter setting of the model and the methods of evaluating the segmentation results. Subsequently, the results are be analysed.

The dataset that was used for this part of the research was the same dataset used in Section 4.3.1 (BRATS2017 dataset). The same procedure was used to separate the dataset – 75% of the patients formed the training set and 25% of them made up the testing set. The same corresponding ground truths were used with the two classes (see Figure 6-2).

The performance accuracy of the ROI masks method was evaluated on a test set of MRI modalities. In this section, the tumour structure is defined as label 1 and label 0 is used for everything else. The overlap ratio between the segmentation results and the ground truth that produced 2labels is evaluated below using the F-measure. This method was performed on the dataset MATLAB2018b on a PC with CPU Intel Core i7 and 16GB RAM with the operating system Windows 7.

To obtain an optimal ROI area, the pre-trained SegNet network was trained separately with each MRI modality. Hereafter, the four trained SegNet models are evaluated separately on the testing dataset of each MRI modality for binary image segmentation. The model that achieved the highest F-measure accuracy out of all four models would be selected to detect the ROI in MRI images. The following sections show the results and analysis of each model.

B- ROI Masks from Different Modalities

1- ROI_ Flair _SegNet model

In this experiment, the semantic segmentation SegNet model was trained with a single modality, which was a FLAIR image only for segmentation with two labels. In the testing stage, the trained SegNet model was applied, and labels were assigned to each pixel in the FLAIR modality. Then the area of the ROI was obtained by grouping the pixels as either tumour or background – the background included healthy tissue and image background. The results showed that the F-measure for ROI was significantly high (0.86). This suggests that using FLAIR modality with the input images in the SegNet network can accurately define the outer margins of a tumour region. The FLAIR protocol has been regarded as a highly effective sequence image that helps to separate the hyper-intensity oedema region from the cerebrospinal fluid (CSF) because the signal of the water molecule is suppressed in this type of MRI modality (Jin et al. 2014). Figure 6-3 shows the predicted ROI mask using the ROI_ Flair _SegNet method.

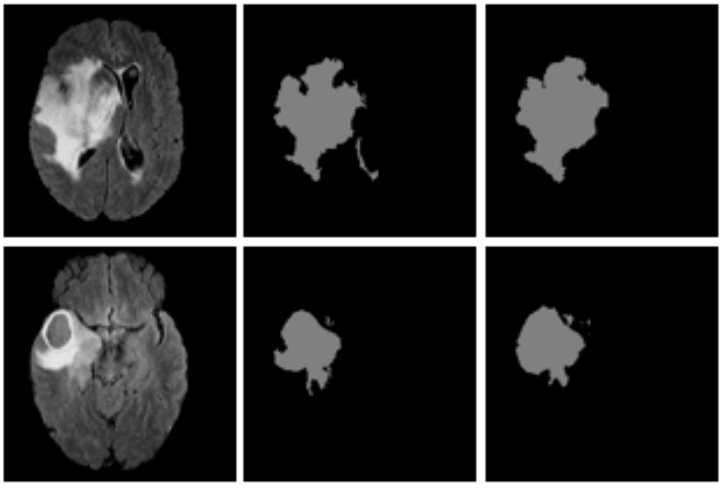

Figure 6-3: FLAIR modal images, ground truths and predicted masks of ROI using the ROI_ Flair _SegNet model (left to right).

2- ROI_T1_SegNet model

The model parameters settings in this experiment are the same as those for the ROI_Flair_SegNet model, except for the input image. T1 modality was used as the input

image. The overall F-measure was 0.74 for the testing set, which shows that the T1 modality presents less information related to the tumour regions than that related to the healthy tissues (see Figure 6-4).

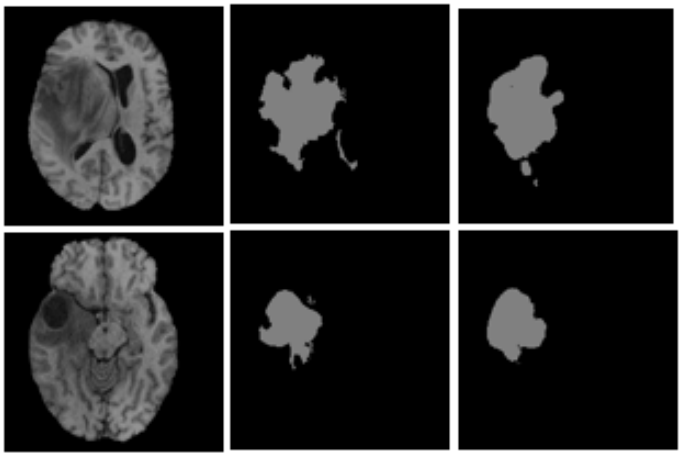

Figure 6-4: T1 modal images, ground truths and ROI masks using the ROI_T1_SegNet model (left to right).

3- ROI_T1ce_SegNet model

In this experiment, the T1ce protocol was used as an input image into the SegNet network. From the results of this model, the accuracy of F-measure for ROI was 0.76. Therefore, the T1ce protocol introduced information that revealed the necrosis and the active tumour region (enhanced tumour), which can be distinguished easily (Bauer et al. 2013). Moreover, these two regions together represent the core tumour, while our target was to detect the full extent of the tumour region (see Figure 6-5).

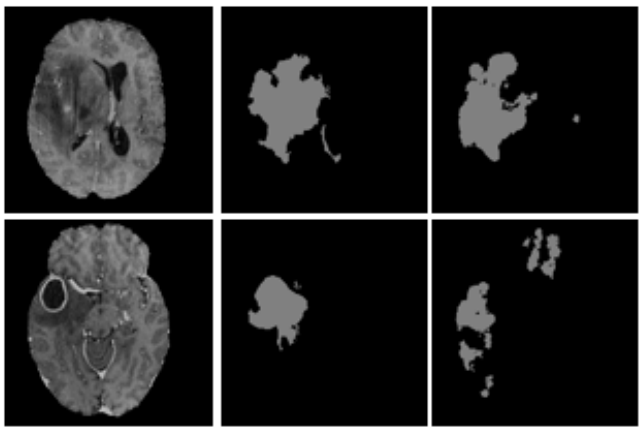

Figure 6-5: T1ce modal images, ground truths and ROI masks using the ROI_T1ce_SegNet model (left to right).

4- ROI_T2_SegNet model

In this scenario, the T2 sequence was used in the SegNet network with the same parameter settings as in the previous sections. The ROI can be detected in all the tested images where the F-measure was 0.80 (see Figure 6-6).

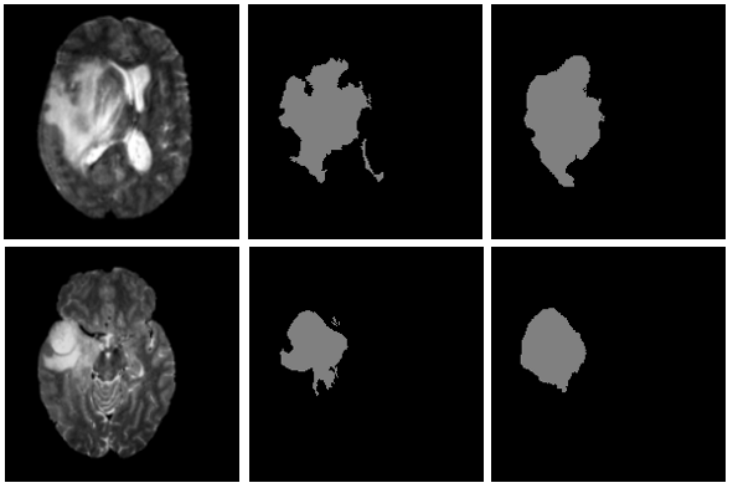

Figure 6-6: T2 modal images, ground truths and ROI masks using the ROI_T2_SegNet model (left to right).

C- Best ROI Masks

The initial ROI was experimentally detected using four models and from a comparison between the results with the four models. The ROI_FLAIR_SegNet model presents a high-performance accurate result for ROI detection. Therefore, the next stage of the proposed method was based on the ROI_FLAIR_SegNet model to generate an ROI mask. This was used to create ROI images (see the next section).

6.2.4 ROI MRI Images

The information for separating the different sub-tumour regions (i.e. oedema, necrosis, and enhanced tumour) exists in different MRI modalities. Therefore, in this section `we report the combination of three MRI modalities images (FLAIR, T1ce and T2). The ROI images were then generated from the three combined MRI modalities based on the obtained ROI mask images, where all of the pixels in the combined MRI modalities that corresponded to the zero values in the ROI masks were set to zero, while the others remained unchanged. The generated ROI images were used as the inputs in the next stage of our proposed method to segment the sub-tumour structures. Figure 6-7 shows examples of the process of generating ROI images using some MRI images.

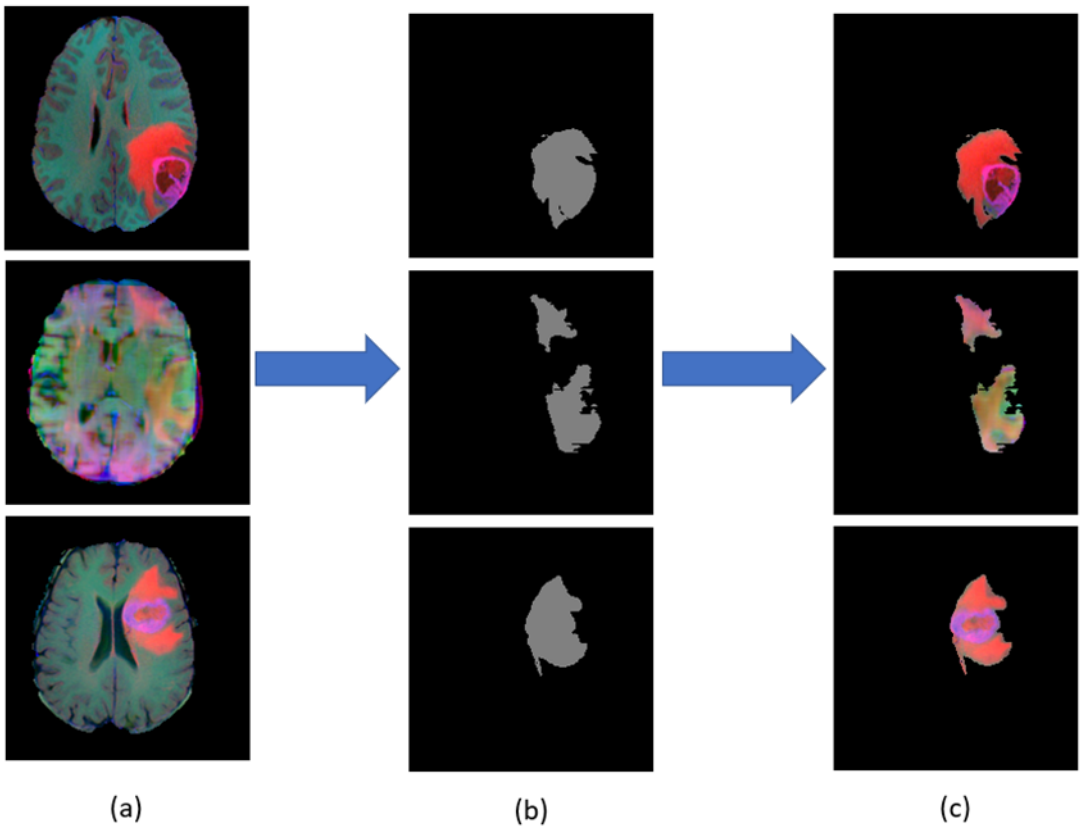

Figure 6-7: (a) Combined MRI modalities, (b) ROI mask images and (c) MRI ROI images.

6.2.5 Segmenting MRI Tumour Regions Using SegNet

In this part of the research, the pre-trained SegNet network architecture was modified and adopted to train it for a semantic pixel-wise segmentation of brain tumour regions (i.e. oedema, necrosis and enhanced) in input images that were ROI MRI images. In the testing stage the final segmentation was obtained by max voting to the final score maps of the SegNet. Figure 6-8 demonstrates some examples of dense classification output results that were generated using the SegNet network.

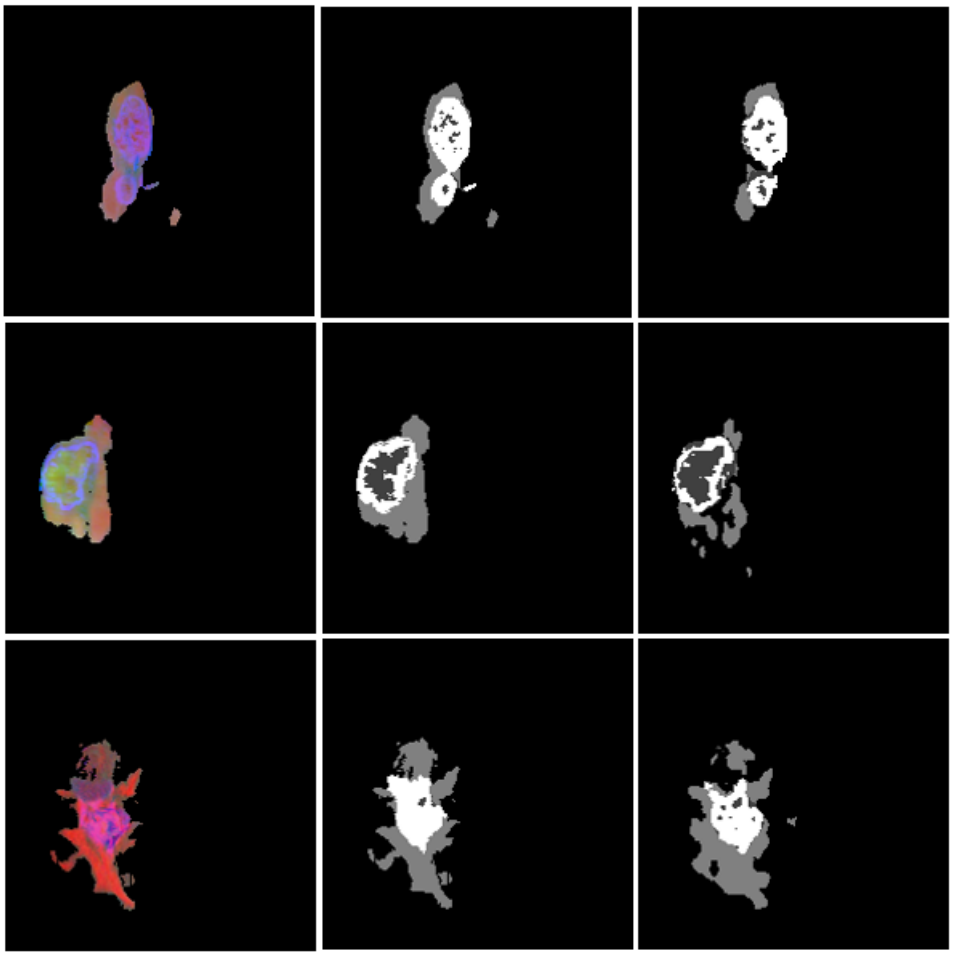

Figure 6-8: MRI ROI images, ground truth and predicted masks (left to right).

By comparing the output results with the ground truth, it can be seen that the SegNet network can successfully segment some parts of the different brain tumour regions. However, some of the output segmentation results label similar pixels as dissimilar (see Figure 6-8), which diminishes the performance of SegNet in segmenting brain tumour regions. This happens because SegNet cannot catch all the changes in the brain tissues that are caused by the tumour. Therefore, we used texture features to incorporate the information that reflected these tissue changes. Texture features that are based on the GLCM can indicate various types of region because the different tissues in the MR images appear as different textures. Consequently, the texture descriptors will have enough discriminatory power to distinguish between regions of different types (AG and Pattar 2017). Hence, fusing the GLCM-based texture features with the SegNet features will incorporate more powerful feature descriptors into the final segmentation, which

may help to overcome this limitation in the SegNet network and improve the performance of the brain tumour segmentation.

6.2.6 Machine Learned Features Extraction with SegNet

The features extracted from the SegNet network are score maps that are produced from the trained SegNet for each output class. Following the last decoder layer in the SegNet network, the final predicted segmentation mask was obtained by setting each pixel label to that of the score map with the maximum value in all the final maps. These score maps contain all of the features of the hierarchy that exhibit lower and higher resolution. It can be seen from Figure 6-9 that in the case of the BRATS dataset the number of classification labels is the same as the number of score maps.

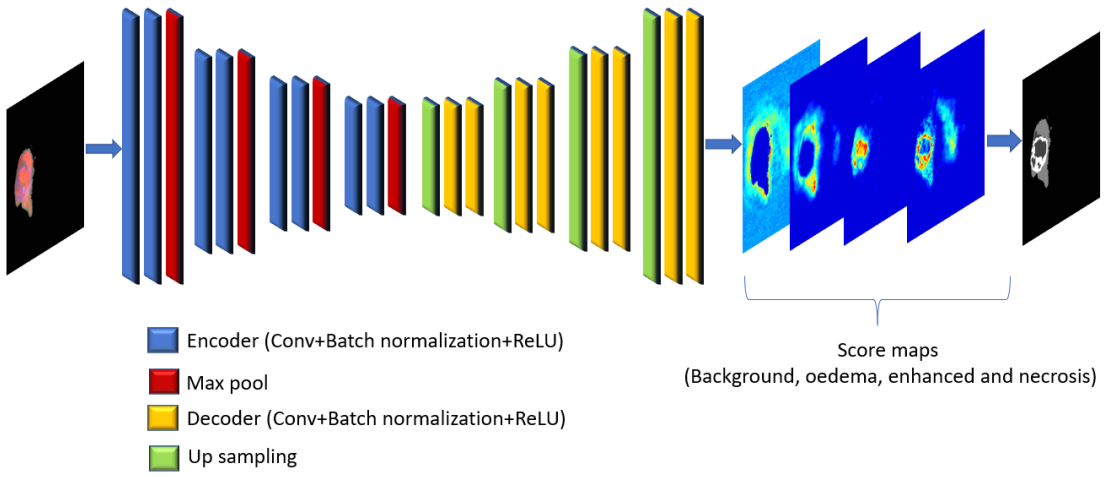

Figure 6-9: Score map extraction in the SegNet network.

A four-dimensional feature vector is created for each pixel in the MRI images. The value of each score map layer is equivalent to the value of each element in the feature vector for the corresponding pixel. Figure 6-10 shows the MRI protocol images and the SegNet-based score maps for each class.

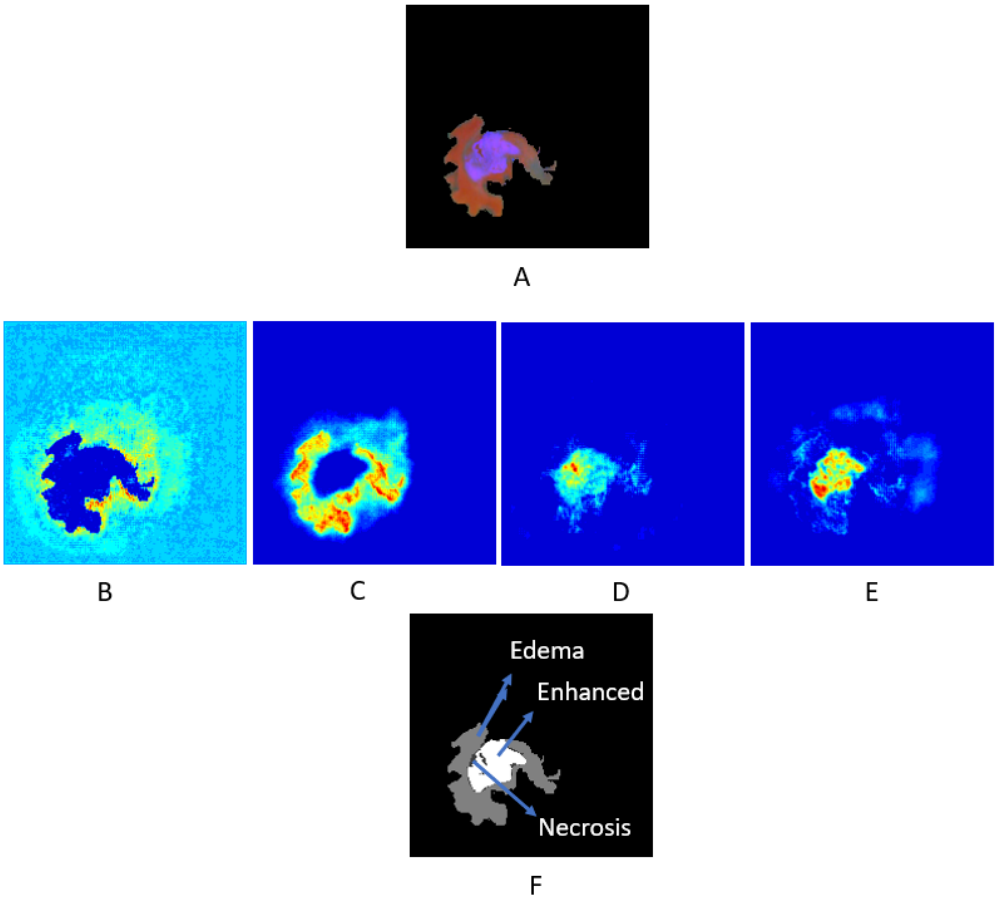

Figure 6-10: ROI image, SegNet based score maps (B: Background, C: oedema, D: necrosis and E: enhanced) and segmentation mask (top to bottom).

6.2.7 Hand-Crafted Features Extraction with GLCM

The results of the SegNet-based segmentation method showed a label disagreement between similar pixels in different tumour brain regions. The reson for this was that the MRI images of a brain tumour are complex because the tumour tissues are overlappe or arbitrary in shape, and there is less regularity in both the number of classes present in an image and their spatial arrangement. An additional difficulty is caused by the widely varying sizes of the object classes in the image. Consequently, the appearance (texture and shape) can also vary widely. Therefore, the greatest challenge for the SegNet-based segmentation method is to capture all the information in the tumorous regions. To overcome this drawback, GLCM-based textural features were extracted from the ROI images and merged with the SegNet features that were also extracted from the same region, in order to obtain a powerful feature descriptor that represented all of the

different tissue regions of the tumour. GLCMs can supply additional textural properties that may not be captured by the SegNet network alone. The most popular texture analysis methods for MR images were found to be the GLCMs (Holli et al. 2010). Moreover, Lai et al. (2011) praise the usefulness of GLCM-based textural features for very accurately separating the subtype of medulloblastoma in children. The next section discusses the GLCM texture analysis method that is employed in the present research.

6.2.7.1 GLCM Matrix-based Textural Features

Haralick et al. (Haralick et al. 1973) were the first to introduce the GLCM method, the earliest texture analyser for classifying aerial photographs and satellite images. In GLCM computing, a special relationship is considered and the frequency of grey levels is arranged between pairs of pixels across the whole intensity range. Therefore, Haralick features are much helpful for providing local pixels dependencies features. The spatial relationship is distinct in terms of distance (d) and angle (θ). The GLCMs have rows and columns that are equal to the number of grey levels. GLCMs count the number of pairs of grey level pixels at a distance d within an ROI in four directions (θ): 0^o, 45^o, 90^o, and 135^o.

The GLCMs can be reassembled, as shown in Figure 6-11. An example of a digital image is given in Figure 6-11 (A) with five grey levels (0, 1, 2, 3, and 4); and the GLCMs with d = 1, scanned in four directions, are created as shown in Figure 6-11 (B, C, D and E). The GLCMs show a range of patterns: for example, the pixel pair (2, 4) is counted differently in the four GLCMs. In the horizontal (0^o), the diagonal (45^o), the vertical (90^o) and the anti-diagonal (135^o) directions, the pixels pair (2, 4) appear 4, 1, 1 and 0 times, respectively.

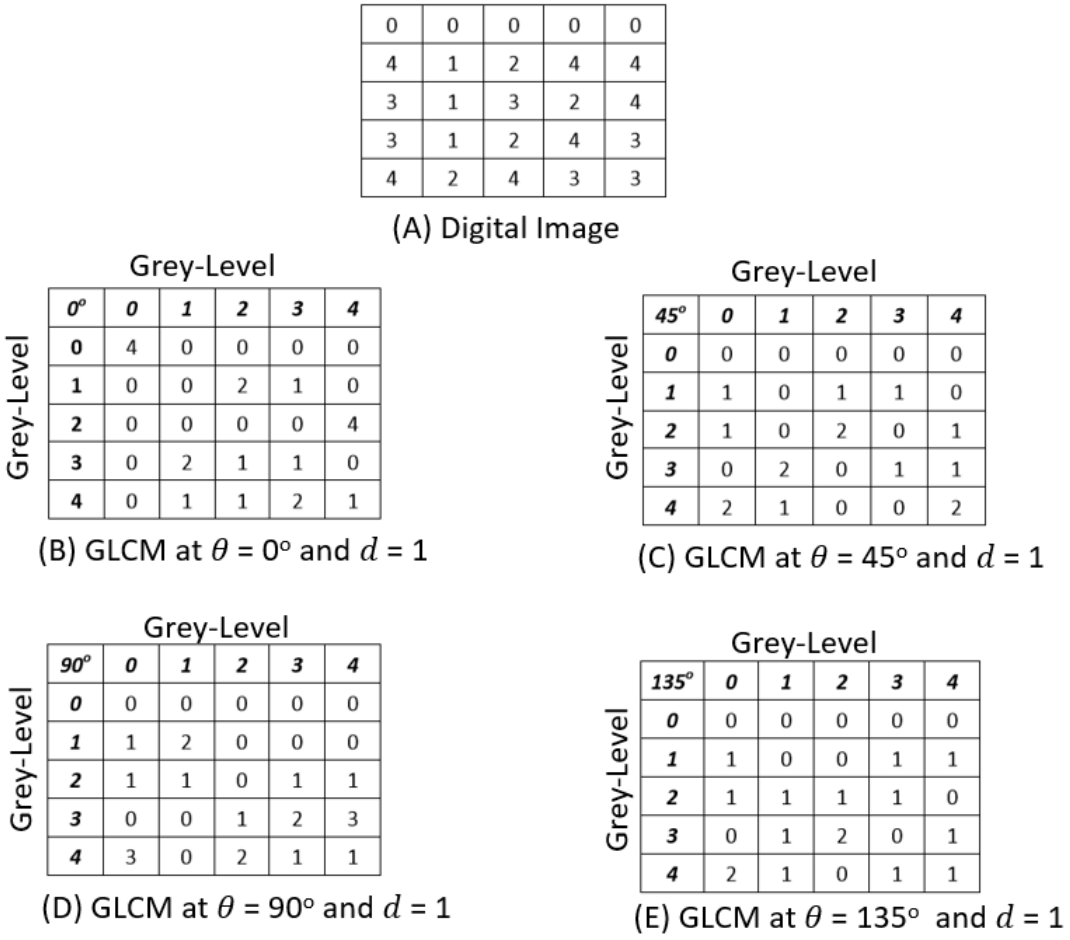

0	0	0	0	0
4	1	2	4	4
3	1	3	2	4
3	1	2	4	3
4	2	4	3	3

0°	0	1	2	3	4
0	4	0	0	0	0
1	0	0	2	1	0
2	0	0	0	0	4
3	0	2	1	1	0
4	0	1	1	2	1

45°	0	1	2	3	4
0	0	0	0	0	0
1	1	0	1	1	0
2	1	0	2	0	1
3	0	2	0	1	1
4	2	1	0	0	2

90°	0	1	2	3	4
0	0	0	0	0	0
1	1	2	0	0	0
2	1	1	0	1	1
3	0	0	1	2	3
4	3	0	2	1	1

135°	0	1	2	3	4
0	0	0	0	0	0
1	1	0	0	1	1
2	1	1	1	1	0
3	0	1	2	0	1
4	2	1	0	1	1

Figure 6-11: An example illustrating the generation of four co-occurrence matrices from the digital image.

In this thesis, the GLCMs for distance d=1are constructed in four directions: θ = 0º, 45º, 90º, and 135º. GLCM-based textural features are calculated by using the built-in function in MATLAB. The GLCM approach can deliver the spatial interrelationships of the grey tones, which are used to report the optimised brain tumour segmentation method in this chapter.

Three textural features can be extracted from each special-dependence matrices of the grey level for distance d=1 to extract the characteristics of the textural statistics of the brain tumour image. These selected features (ASM, Contrast and the correlation) provide the most useful features that related to our requirement (local pixel dependencies). The following will be defined as the three features to be considered (Haralick et al. 1973).

1- The angular second-moment feature (**ASM)** is a measure of the homogeneity of the image. **ASM** is high when the image is highly homogeneous or when pixels are very similar. It is calculated using

$$ASM = \sum_{i=0}^{N_g-1} \sum_{j=0}^{N_g-1} \boldsymbol{p_{ij}^2} \quad (6\text{-}1)$$

where *i* and *j* are the special coordinates of the function *p(i,j)*, and N_g is grey tone.

2- The contrast feature is a measure of the amount of local variations extant in the image and is calculated using

$$Contrast = \sum_{n=0}^{N_{g-1}} n^2 \left\{ \sum_{i=1}^{N_g} \sum_{j=1}^{N_g} p(i,j) \right\}, \quad |i-j| = n \quad (6\text{-}2)$$

3- The correlation feature is a measure of the linear dependency of the grey levels of neighbouring pixels in the image and is calculated using

$$Correlation = \frac{\sum_{i=0}^{Ng-1} \sum_{j=0}^{Ng-1} (i,j) \,.\, p(i,j) - \mu_x \mu_y}{\sigma_x \sigma_y} \quad (6\text{-}3)$$

where μ_x, μ_y, σ_x, σ_y are the means and standard deviation of p_x and p_y, p_x and p_y are calculated by:

$$p_x(i) = \sum_{j=1}^{N_g} P(i,j) \quad (6\text{-}4)$$

$$p_y(j) = \sum_{i=1}^{N_g} P(i,j) \quad (6\text{-}5)$$

6.2.8 Combined Feature Extraction

This section demonstrates the spatially combined features that were optimised from SegNet and the GLCM-based features. Figure 6-12 shows an example of a case image, a SegNet-based score map of the oedema class, and the feature representations of two pixels of different classes (oedema and necrosis). In the oedema score map of the SegNet network, there is no presentation of the obvious separation of the necrosis and oedema classes. The values for the corresponding pixels were 0.4186 and 0.4119, respectively. These two values are very close. Therefore, it seems that the presentation of the local boundaries of the tumour regions in the oedema score map does not have enough detail. Subsequently, the predicted mask image that was based only on the SegNet method did not match the ground truth image. The local neighbourhood dependencies of GLCM texture features made the labels (i.e. oedema and necrosis) more separable (see Figure 6-13).

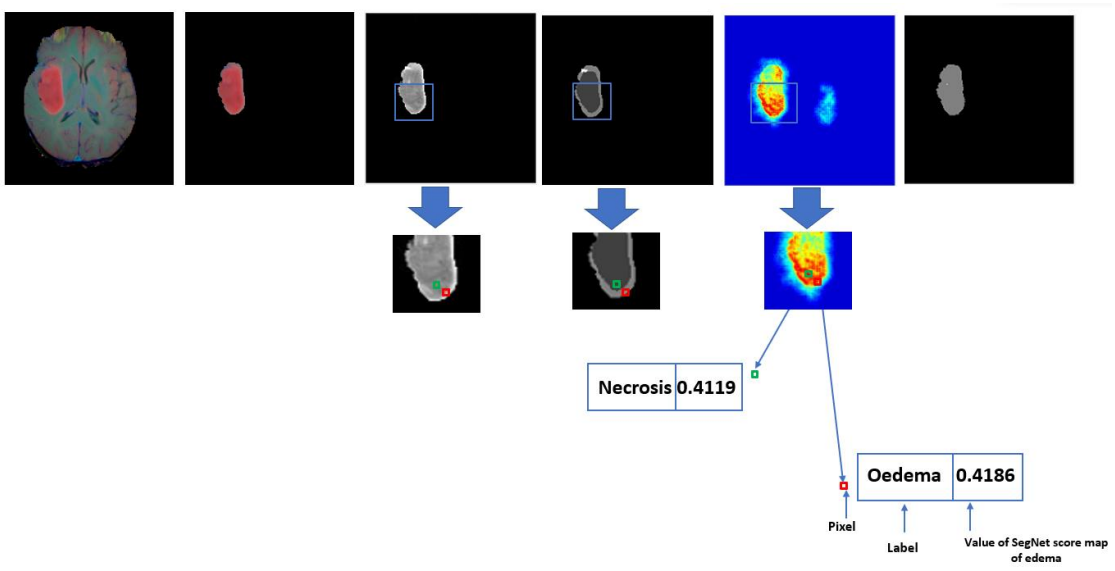

Figure 6-12: MRI modalities, ROI image, T1ce MRI modality, GT, SegNet score map of oedema and predicted mask (left to right).

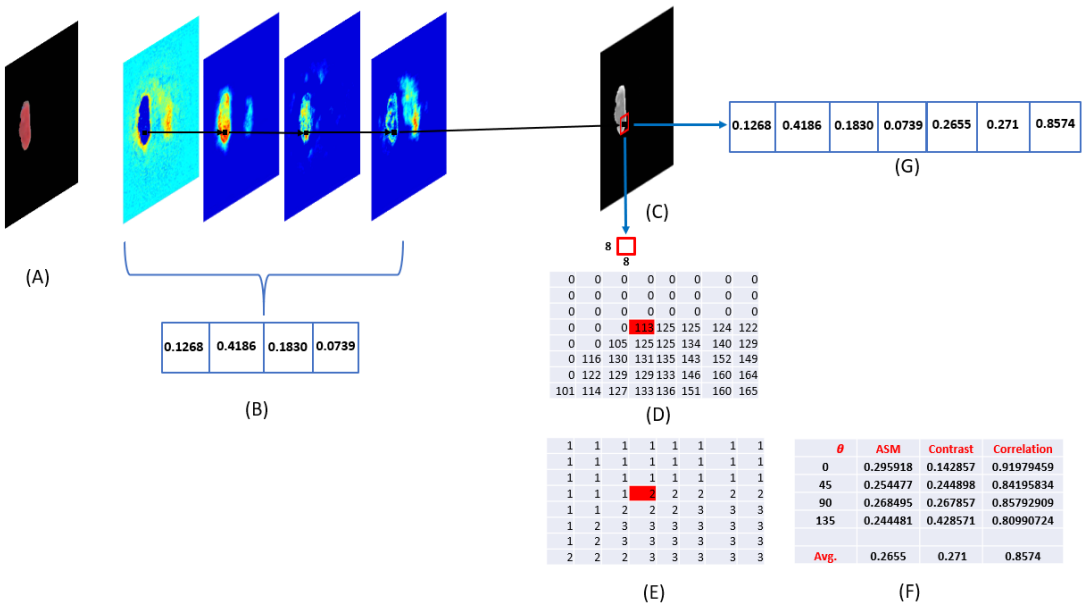

Figure 6-13: (A) ROI image, (B) SegNet score maps feature (background, oedema, necrosis and enhanced), (C) T1ce MRI modality, (D) A (8 × 8) T1ce image block of the pixel of interest in red colour, (E) clustered version of the image block for the same pixel of interest, (F) texture features extracted from GLCM spatial dependency matrices and (G) Output feature vector of the corresponding pixel.

The SegNet-based features were selected from each layer of the four score maps for the corresponding pixel. Meanwhile, the GLCM-based texture features were extracted in a fixed-size window of 8 × 8, centred on this pixel in the T1ce images. The T1ce MRI modality was selected because the tumour core has clear boundaries in this modality, which improves the segmentation performance of the tumour core. These textural features are based on the statistics that represent how frequently one grey level will appear with another specific grey level in the image.

The combined feature vector for each pixel consists of seven elements (Four SegNet scores (background, oedema, necrosis and enhanced) and three GLCM features (ASM, contrast and correlations) are shown in Figure 6-13 (G) and in Table 6-1. This information is then fed into the DT to classify the pixel.

Table 6-1: Feature details that are used in the proposed system.

Feature	Type	Total number
SegNet	Machine-learned	4
GLCM	Hand-Crafted	3
Total	-	7

6.2.9 DT Parameters and Segmentation

In ROI images, for each pixel in the tumour target area, a feature vector (i.e. 7 features for each pixel) is extracted and then fed into the DT classifier for training. As described in Section 4.3.5, different varieties of tree depth (D_{tree}) were calculated on the BRATS 2017 training patient datasets. The fine tree with D_{tree} =100 was observed to provide better classification accuracy than the other tree depths (medium and coarse tree). The final predicted mask was generated by mapping back the pixel class that was assigned for each pixel in the ROI images of the testing dataset to the volume of the segmentation mask.

6.3 Experiments on the Proposed Method

The experiments were evaluated on the BRATS2017 dataset. The overlap measures for a segmented tumour against ground truth were constructed for quantitative evaluations of the proposed method. In the following subsection, the evaluation and implementation of segmentation results are described.

6.3.1 Experiment Setting

The evaluation for this section is similar to the evaluation in Section 4.4.2.

The MATLAB deep learning toolbox was used in the training and testing SegNet model for semantic segmentation of the brain tumour and the DT classifier was implemented using the classification learner toolbox, which is also based on MATLAB. With respect to deep learning, the whole training process for the SegNet model took approximately 12 hours on a single NVIDIA GPU Titan XP.

In this section, two sets of qualified experiments were undertaken to evaluate the performance of the proposed method.

1- SegNet

   In this experiment, the SegNet was directly applied to the dataset to segment the tumour regions. No hand-crafted tuning was needed in this phase.

2- SegNet_GLCM_DT

   As discussed in Section 6.2.6, the GLCM based texture features provide strong descriptors that significantly represent the textural information from the different tissue regions of the tumour. Fusing the GLCM based texture features with the SegNet based features was selected in this phase so as to include more local information and optimise the segmentation of the brain tumour regions for efficiency and accuracy.

6.3.2 SegNet Result

Figure 6-8 provides the evaluation results obtained by applying the SegNet segmentation to the BRATS 2017 dataset in some patient samples. Table 6-2 shows that the accuracy of the F-measure in whole tumour segmentation is very good, 0.88 percent, using only SegNet. However, the F-measure in the tumour core and enhanced tumour are 0.63 and 0.60 percent, respectively. Therefore, SegNet can distinguish the region that shows the extent of the tumour, but it cannot accurately and locally determine the sub-region boundaries (core and enhanced tumour).

Table 6-2: Segmentation results for BRATS2017 dataset using SegNet method only.

Method	F-measure		
	WT	TC	ET
SegNet	0.88	0.63	0.60

6.3.3 SegNet_GLCM_DT Result

In this section, the GLCM based texture features are calculated in a bounding box neighbourhood window (e.g. 8×8). As described in Section 6.2.7.1, the parameters of GLCM matrixes are the distance and the angle. To cover orientation better in the texture tissues, four different angles were used, 0 º, 45 º, 90 º, 135 º. In addition, one pixel was selected as the distance between a pixel of interest and its neighbour.

Three types of feature (ASM, contrast and correlation) were calculated from the four GLCM special dependence matrixes for each pixel in the ROI of the T1ce model in a neighbourhood window of 8×8 around this pixel. These features were combined with the features extracted from the SegNet method (see Figure 6-13). Then the feature vectors were fed into the DT classifier. The parameter of DT was selected as in Section 6.2.8, (i.e. the number of tree depth D_{Tree} =100).

Table 6-3 provides the evaluation results obtained by applying SegNet_GLCM_DT to the BRATS2017 testing dataset. In addition, Figure 6-14 shows some patient cases (ROI images) which are the same as the cases in Figure 6-8.

Table 6-3: Segmentation results per patient case in the BRATS 2017 testing dataset using the SegNet_GLCM_DT method.

Method	F-measure		
	WT	**TC**	**ET**
SegNet_GLCM_DT	0.98	0.75	0.69

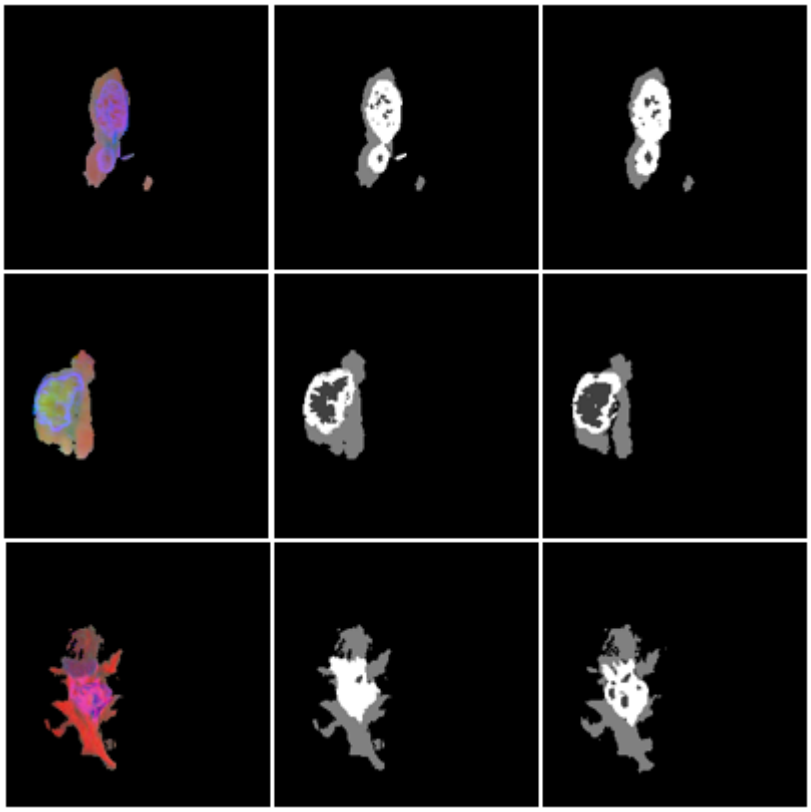

Figure 6-14: ROI images, Ground truth and predicted masks using SegNet_GLCM_DT (left to right)

As can be seen in Table 6-3, adding the GLCM based texture features to the pipeline improves the F-measure in the three different brain tumour structures (i.e. WT, TC and ET).

6.4 Modification of the Proposed Method

The previous sections have shown that the proposed SegNet_GLCM_DT method presents greater F-measure accuracy in the complete tumour than in the two other tumour structures (i.e. the tumour core and the enhanced tumour). To increase the robustness of the proposed method in segmenting the tumour core and enhanced tumour structures, further modifications were made to the proposed SegNet_GLCM_DT model. The first modification was to train and test the SegNet_GLCM_DT model to provide predicted masks of the brain tumour with only three labels (background, oedema, necrosis and enhanced tumour), instead of predicted masks with four labels (background, necrosis and enhanced tumour) in the original SegNet_GLCM_DT

method. The second modification process combined the ROI masks that had only two labels (background, complete tumour) with those that had three-label masks, so as to obtain the final segmentation masks of all the brain tumour regions using the mask fusion method. Figure 6-15 displays the modification of the proposed method, which is termed the modified SegNet_GLCM_DT method.

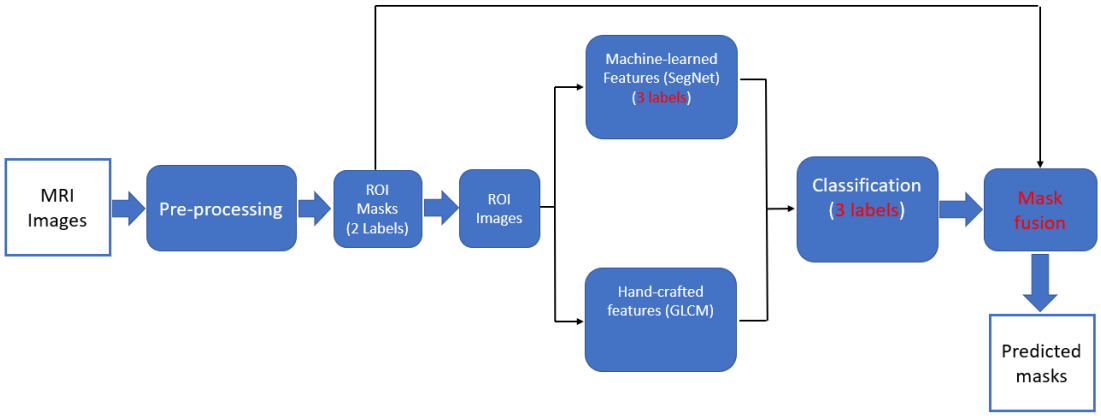

Figure 6-15: The pipeline of the modified SegNet_GLCM_DT segmentation method.

6.4.1 Segmented Masks of Three Labels

This section reports how the SegNet network was modified and adopted for the segmentation of the three-label brain tumour regions in the ROI images. To obtain ground truth with three-label images for training purposes, the original ground truth images were modified by removing the oedema part from the images (see Figure 6-16).

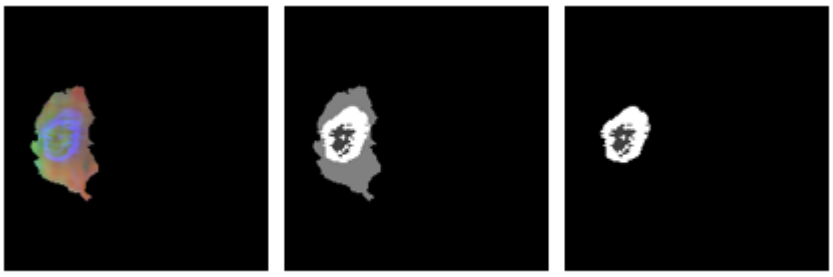

Figure 6-16: ROI image, original ground truth and 3-label ground truth (left to right).

The processes of obtaining ROI images in the modified proposed method were identical to those in the original proposed method; that is, pre-processing and ROI (2label) masks. There were three machine-learned features, namely, the score maps that were generated from the trained SegNet (with 3 labels). Therefore, for each pixel in the ROI images, a six-dimensional feature vector was constructed. The values of the first three elements in the feature vector were equivalent to the values of the three score maps for the corresponding pixel. Meanwhile, the element values in the second three elements of the feature vector represented the extracted GLCM-based textural features. Then the feature vectors were fed into a DT classifier to classify each ROI image pixel as a segmented mask with three labels (see Figure 6-17).

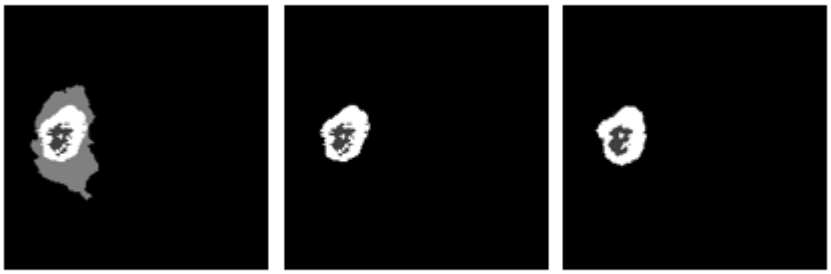

Figure 6-17: Original ground, 3label ground truth and predicted mask with of 3 labels (left to right).

6.4.2 Mask Fusion Method

The segmented mask with three labels ignores the oedema region. Therefore, the mask fusion method was adopted as a post-processing step to obtain the final segmentation mask results, which had the four brain tumour labels. In the mask fusion method, a combining procedure was considered between the ROI masks (with 2 labels) and the segmented masks with 3 labels, which represented the following conditions (see Figure 6-18):

1- The pixels within the ROI mask whose grey values were zero, and the grey values of the corresponding pixels in the 3-label mask were also zero. Hence, the corresponding pixel values in the output final mask were also equivalent to zero.

2- Pixels within the ROI mask area whose grey values were equal to 128, and the corresponding pixels in the 3-label masks whose grey values were zero had output corresponding pixel values in the final segmented mask of 128.

3- Pixels within the tumour region in the ROI mask whose grey values were 128, and corresponding pixel values in the 3-label masks which were equivalent to 64 had consistent pixels values in the output mask of 64.

4- The pixels within the ROI mask whose grey values were 128, and the matching pixels whose grey values in the 3-label masks were 255 had corresponding pixel values in the final mask of 255.

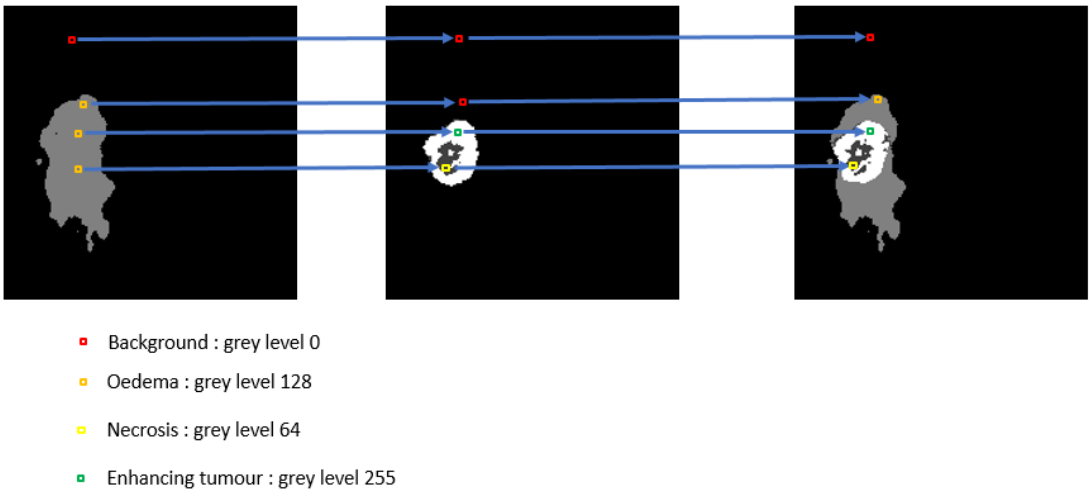

Figure 6-18: The process of mask fusion method: 2-label masks, 3-labelmasks and predicted mask of brain tumour regions (left to right).

6.5 Experiment on the Modified SegNet_GLCM_DT Method

This section presents the evaluation results of the modification SegNet_GLCM_DT in brain tumour segmentation. In this section the dataset, evaluation and implementation are described. Then two experiments were conducted: in the first experiment, the ROI images of the training dataset were used to train the SegNet 3-label model; and in the second experiment, the mask fusion method was optimised to obtain the final segmentation mask of a brain tumour.

6.5.1 Experimental Setting

The BRATS2017 dataset was analysed with this model, which was the same as the dataset that was used in the SegNet_GLCM_DT method. The evaluation and implementation processes that were used in the modification SegNet_GLCM_DT model were similar to the processes described in Section 4.4.2.

To evaluate the performance of the modification SegNet_GLCM_DT method, three experiments were performed using the BRATS 2017 dataset.

1- SegNet_ 3-label model

   In the first experiment, the ROI images were obtained using the same procedure that was used in the SegNet_GLCM_DT method. Then the SegNet model was trained to segment three labels (background, necrosis and enhanced tumour) of a brain tumour using the ROI image training dataset.

2- SegNet_GLCM_DT_ 3-label model

   The second experiment was designed to evaluate the 3-label masks of a brain tumour, a proposed method that was described in Section 6.4.1.

   In this phase, the parameters of the GLCM based texture features – that is, the distance, d=1, and the directions, θ=0^o, 45^o, 90^o, 135^o – had to be tuned; Correspondingly, the parameters of DT classifier were optimized as in Section 6.2.7; that is, the tree depth D_{Tree} = 100.

3- Mask fusion method

   The third experiment was conducted simply to add information about the ROI mask to the information about the segmented 3-label mask. The details of this method are clarified in Section 6.4.2, above.

6.5.2 Modified SegNet_GLCM_DT Experiment Results

Table 6-4 lists the evaluation results obtained by applying the modification SegNet_GLCM_DT method to the BRATS2017 dataset. Figure 6-19 shows the examples, which are the same as in Figure 6-8 and Figure 6-14, of the segmentation of tumour structures in some items of the BRATS2017 testing dataset, using the modified SegNet_GLCM_DT method.

Table 6-4: Segmentation results per patient cases in the BRATS 2017 testing dataset using the modified SegNet_GLCM_DT method.

Method	F-measure		
	WT	TC	ET
Modified SegNet_GLCM_DT	0.88	0.78	0.73

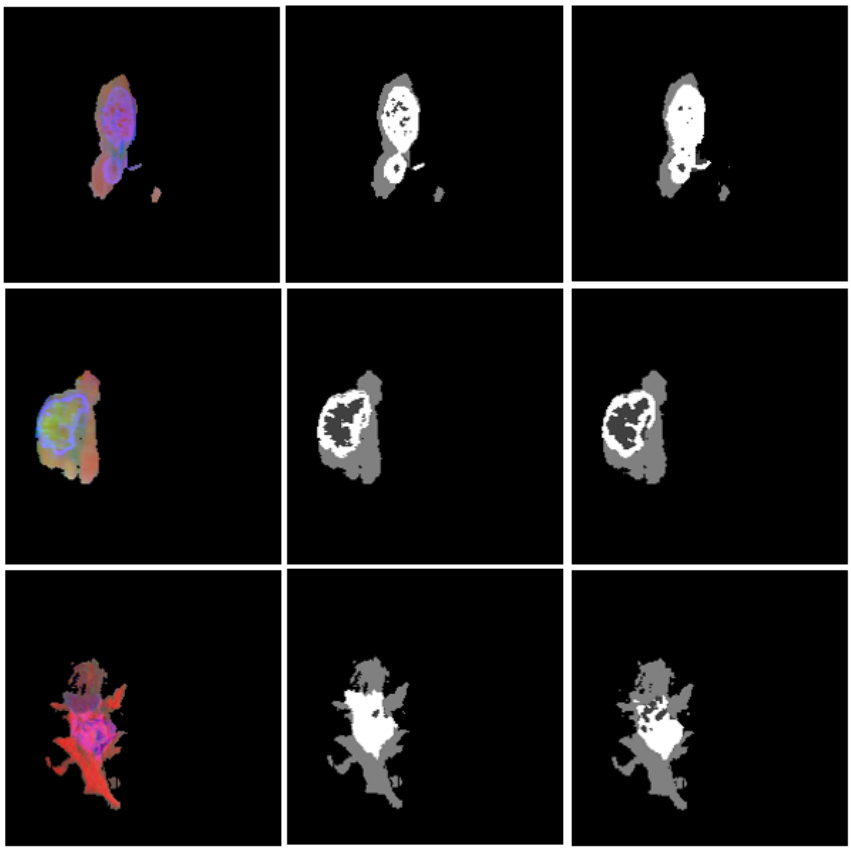

Figure 6-19: ROI images, ground truth and predicted masks using the modified SegNet_GLCM_DT (left to right).

As can be seen in Table 6-4, adding the modifications to the pipeline of the SegNet_GLCM_DT method improves the F-measure accuracy for the core and the enhanced tumour, while it somewhat reduces the accuracy of the tumour as a whole. This happens because the machine learning classifier does not need many threshold values to differentiate the data when the machine learning is being trained to detect a small number of classes. In such cases the training process is easier, and more accurate results are obtained.

Conversely, the process of training is complicated as the number of classes increases because more information is used by the machine learning to detect the labels by differentiating the values. In addition, the accuracy of the complete tumour is reduced because the oedema detection in this method is based on the results of the ROI mask model.

6.6 Discussion

This chapter has presented some contributions to our knowledge of brain tumour segmentation. First, a pre-trained SegNet-inspired deep convolutional neural network architecture was developed for binary segmentation to detect ROI mask images. We cannot use the ground truth of binary region images instead of the ROI masks for generating ROI images because the ground truth images are available only with the training dataset but not available with the testing dataset. Therefore, we developed model to generate ROI masks for detecting region of interest in the training and testing datasets. As part of the standard diagnostic clinical MRI of brain tumours, FLAIR images are often generated in clinical practice. The experimental results demonstrate a robustness and a high-performance accuracy of automated detection and segmentation of the complete tumour region in FLAIR MRI modality. For this reason, the ROI_FLAIR_SegNet model was chosen to segment the whole tumour boundary region. Second, a pre-trained SegNet network was also adopted but the SegNet network was used in this case to segment all the tumour regions according to the ROI MRI images that were obtained from the ROI masks. The experimental results demonstrate the highest accuracy in detecting whole tumours, but not in the detection of cores and enhanced tumours. The problem with this method was that it could not accurately detect all the changes in the texture of the brain tissue that had been caused by the tumour, especially in the enhanced tumour region, because this region presents more rough edges. Therefore, to overcome this problem, GLCM-based texture features were considered for use with SegNet-extracted features which provided a local dependences and neighbourhood system of the pixel for classification. The experimental results in Section 6.3.3 show that there was a significant improvement in the performance of the F-measure in detecting whole tumours. The accuracy of delineating the tumour core and enhanced tumour was also increased but was still less than state-of-the-art. Table 6-5 presents an overall comparison of the F-measure accuracy of each tumour part using different combinations of the suggested methods. Moreover, Table 6-6 shows a significant improvement in the results of our methods.

Table 6-5: Comparison of F-measure (mean and standard deviation) for our experiments separated for whole tumour, tumour core and enhanced tumour.

Methods		F-measure		
		WT	TC	ET
SegNet	Mean	0.88	0.63	0.60
	Standard deviation	0.03	0.33	0.37
SegNet_GLCM_DT	Mean	0.98	0.75	0.69
	Standard deviation	0.02	0.31	0.35
Modified SegNet_GLCM_DT	Mean	0.88	0.78	0.73
	Standard deviation	0.03	0.31	0.32

Table 6-6: Performance of P-values between our experiments for different brain tumour regions.

Methods	P-value		
	WT	TC	ET
SegNet Vs SegNet_GLCM_DT	<0.05	<0.05	<0.05
Modified SegNet_GLCM_DT Vs SegNet_GLCM_DT	<0.05	<0.05	<0.05

From Table 6-7 we can see that the SegNet_GLCM_DT method can get better results in whole tumour segmentation, although the accuracy with core and enhanced tumour segmentation is not better than that of Kamnitsas et al. (2018) and Wang et al. (2017). This is because the necrosis and enhanced tumour regions have complex structures compared with the oedema region, and our method has relatively low accuracy in the detection of necrosis and enhanced tumours.

Table 6-7: Performance of our proposed method compared with other methods on the BRATS 2017 dataset, using the SegNet_GLCM_DT method.

Method	F-measure		
	WT	**TC**	**ET**
Kamnitsas et.al. (2018)	0.88	0.78	0.72
Wang et al. (2017)	0.873	0.783	0.774
Casamitjana et.al. (2018)	0.86	0.68	0.67
SegNet _GLCM_ DT	0.98	0.75	0.69

Using two models, one for 2-label segmentation and another for 3-label segmentation allows a simpler and more accurate model for each task than using a single model for the substructures of the brain tumour that require a complex model. Therefore, a modification of the proposed method was devised for brain tumour segmentation. The results of the experiments in Section 6.5.2 show that there was a significant increase in the F-measure accuracy of the core and enhanced tumour. However, the accuracy of the whole tumour was less than that with the SegNet_GLCM_DT model because of the segmentation of the oedema based on the results of the ROI mask method.

6.7 Conclusion

This chapter has described four approaches. The first is the binary model, which was used to describe the ROI segments from the whole MRI image to reduce the computational complexity. Experimentally, we found that significant results in the ROI segmentation image were produced by applying the ROI_FLAIR_SegNet method to FLAIR protocol, unlike the results with other MRI modalities (i.e. T1, T1ce and T2).

The other three methods were used to detect different structures of brain tumour based on the data obtained from ROI images. The SegNet method cannot segment the core and enhanced tumour objects consistently and produced weak results. Combining the SegNet method with the GLCM-based texture features in the SegNet_GLCM_DT method produces good results in the tumour core and enhanced tumour segmentation structures, especially those in the tumour as a whole. Although the accuracy of the core and enhanced tumour results is positively changed when the SegNet_GLCM_DT method is used, they are still insufficient to segment the brain tumour tissue subtypes (i.e. necrosis and enhanced tumours). The modified SegNet_GLCM_DT method segments the core tumour and enhanced tumour objects more consistently than the SegNet_GLCM_DT method does.

Overall, our experimental results suggest that the SegNet_GLCM_DT method achieved promising results in the segmentation of whole tumours (0.98%). Meanwhile, the modified SegNet_GLCM_DT method has very good results in tumour core and enhanced tumour segmentation (0.78 % and 0.73%, respectively).

Chapter 7

Clinical Applications

7.1 Introduction

The objective of this chapter is to assess the robustness of the three proposed methods for brain tumour segmentation through a further validation using a practical clinical dataset of brain tumour-type glioma. In addition, this chapter explores the ability of these proposed methods to segment another brain tissue injury task, which is a stroke lesion. A practical clinical stroke lesion dataset and ISLES 2015 were used to train and evaluate the three proposed methods for stroke lesion segmentation.

7.2 Clinical Brain Tumour Segmentation

In this thesis, the three proposed segmentation methods were trained and evaluated using the BRATS 2017 dataset. This section describes how the clinical brain tumour dataset was collected and used to evaluate the three segmentation methods. Additionally, the evaluation results of the three segmentation methods using the clinical brain tumour dataset are compared with the evaluation results of the BRATS 2017 dataset.

7.2.1 Clinical Dataset

This section discusses the brain tumour clinical dataset that was provided by a hospital in China. This practical dataset included 29 patient files of MRI scans, as described in Section 2.5.1.2. Basically, each patient file included the four MRI protocols (i.e. FLAIR, T1, T1ce, and T2) and all the clinical datasets were used to further evaluate the three proposed segmentation methods. To prepare the clinical dataset for the proposed methods, trim processing was performed to remove the unnecessary black areas and information in the image, which gave input images of 192×192 pixels (see Figure 7-1).

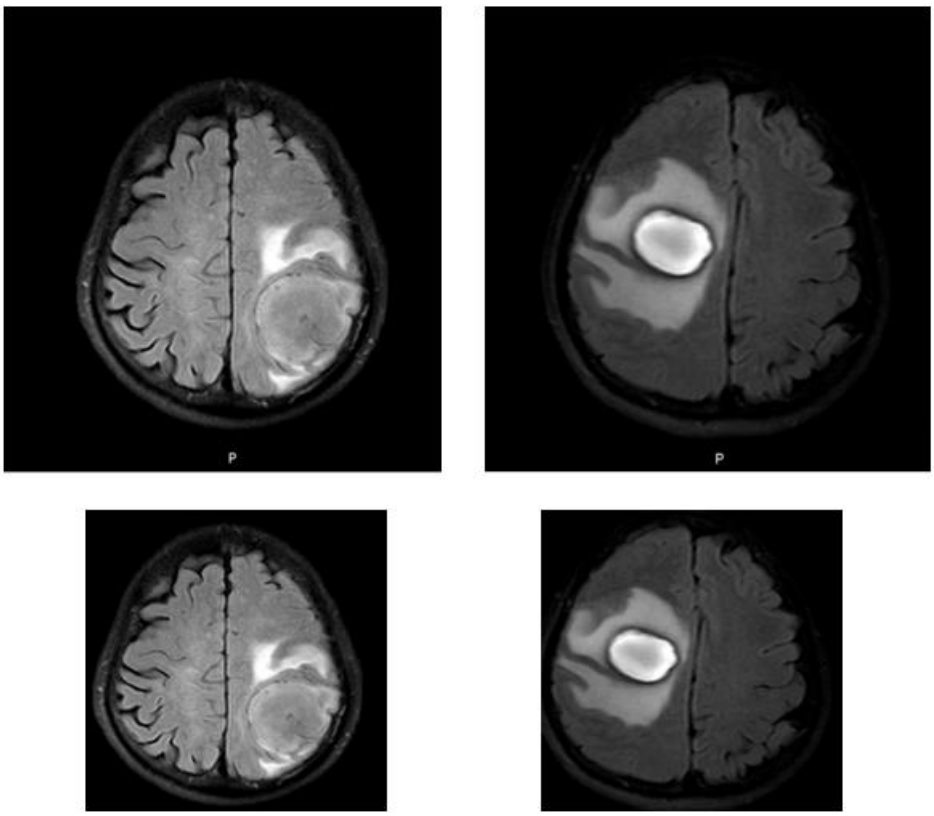

Figure 7-1: Some examples of clinical image data of brain tumour in patients, (first row to second row), images before cropping and images after cropping to 192x192 pixels.

7.2.2 Experimental Results

This section presents the process of evaluating the three proposed segmentation methods and also gives the performance results of brain tumour segmentation using a clinical brain tumour dataset. The pre-processing procedure for the clinical brain tumour dataset in the proposed methods is as follows: implement the bias field correction algorithm based on N4ITK, normalize the intensity and finally select the patches (note that patch extraction is pre-processed with respect to the data for the first proposed method only). The details of the pre-processing steps were given in Sections 4.3.1 and 4.3.1.1, above.

A- CIFAR _PI_HIS_DT

In the study case of the brain tumour segmentation, the performance of most of the models was evaluated in the three brain tumour structures (i.e. whole tumour, tumour core and enhanced tumour).

The clinical brain tumour dataset was implemented on the CIFAR _PI_HIS_DT model for evaluation using the same parameter settings as were used when the CIFAR _PI_HIS_DT model was evaluated on the BRATS 2017 testing dataset. Table 7-1 provides the evaluation results obtained by applying CIFAR_PI_HIS_DT to the brain tumour clinical dataset. Figure 7-2 shows some visual examples of MRI images with the predicted masks using the CIFAR _PI_HIS _DT method.

Table 7-1: Segmentation results from the clinical brain tumour dataset using CIFAR _PI_HIS_DT method.

Method	F-measure		
	WT	TC	ET
CIFAR_PI_HIS _DT	0.79	0.74	0.65

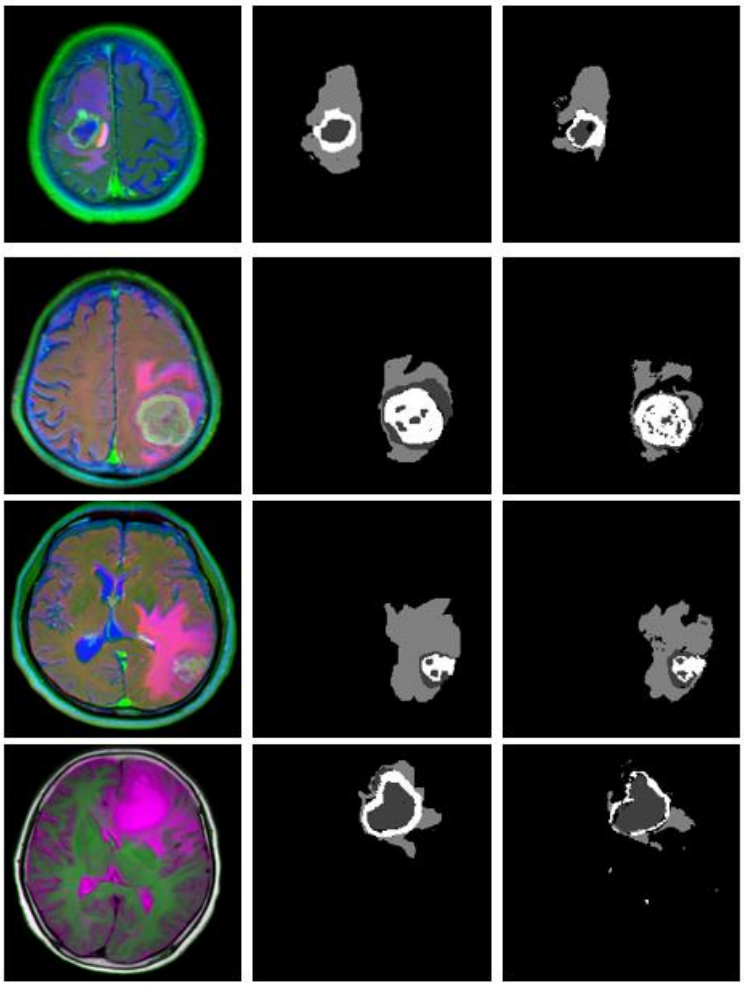

Figure 7-2: Segmentation results for some cases in the clinical brain tumour dataset. combined MRI modalities (FLAIR, T1ce and T2), ground truth images and segmentation masks using the CIFAR_PI_HIS _DT method (left to right).

B- SegNet_Max_ DT

The same parameter settings that were used in the proposed SegNet_Max_DT method were used to evaluate the method proposed in this section, using the clinical brain tumour dataset. Table 7-2 illustrates the evaluation results achieved by implementing SegNet_Max_DT on the brain tumour clinical dataset. Figure 7-3 shows some visual examples of patient MRI images with the segmented masks using the developed SegNet_Max_DT method.

Table 7-2: Segmentation average results on the clinical brain tumour dataset using the SegNet_Max_DT method.

Method	F-measure		
	WT	TC	ET
SegNet_Max_ DT	0.81	0.78	0.75

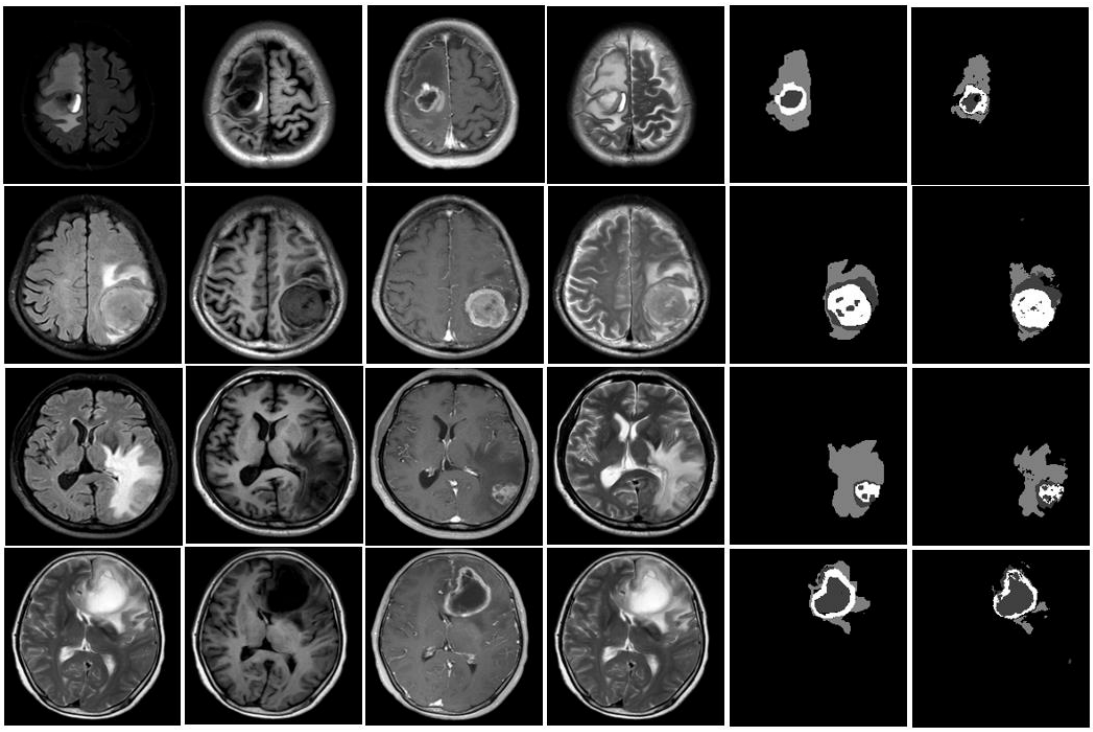

Figure 7-3: Segmentation results for some cases in the clinical brain tumour dataset. MRI modalities (FLAIR, T1, T1ce and T2), ground truth images and segmentation masks using the SegNet_Max_ DT method (left to right).

C- SegNet_GLCM_DT

After detecting the ROI area in different MRI modalities (i.e. FLAIR, T1ce and T2) and combining them to generate ROI images, as in Section 6.2.4, the ROI images were used to evaluate the developed SegNet_GLCM_DT method. The same parameter settings that were used to evaluate the use of the SegNet_GLCM_DT method on the BRATS 2017 dataset were used to evaluate this method on a clinical brain tumour dataset. Additionally, the modification of the SegNet_GLCM_DT method for use on the clinical

data was also evaluated with the same parameter settings that were used with the BRATS 2017 dataset. The results of evaluating the use of the SegNet_GLCM_DT and SegNet_GLCM_DT modification methods on the brain tumour clinical dataset are illustrated in Table 7-3.

Table 7-3 : Segmentation average results on the clinical brain tumour dataset using the SegNet_GLCM_DT method.

Method	F-measure		
	WT	TC	ET
SegNet_GLCM_DT	0.90	0.75	0.71
SegNet_GLCM_DT Modification	0.86	0.76	0.73

Figure 7-4 shows the segmented masks of the same visual examples of MRI images of patients as in the previous section using the SegNet_GLCM_DT method.

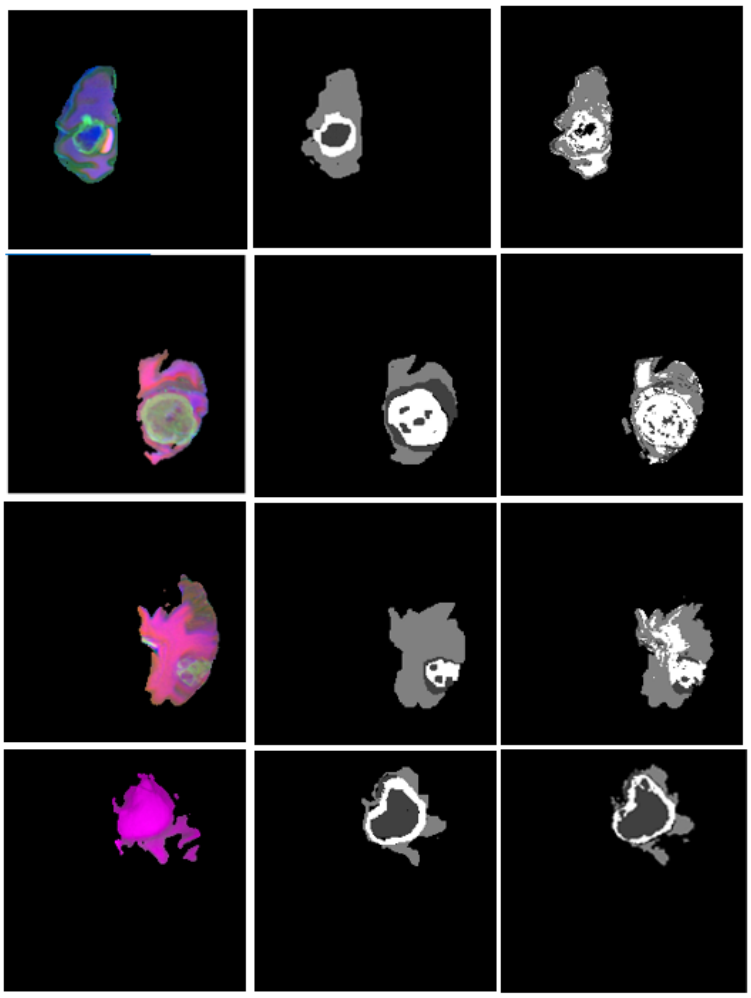

Figure 7-4 : Segmentation results for some cases in the clinical brain tumour dataset using SegNet_GLCM_DT. MRI ROI images, ground truth and predicted masks (left to right).

7.2.3 Discussion for Brain Tumour Segmentation

In this chapter, a clinical brain tumour dataset was collected and used for the further evaluation process because the target of our investigation is to develop segmentation methods for clinical diagnostic use.

We compared the performance of the three developed segmentation methods on the BRATS 2017 and clinical test datasets, as summarised in Figure 7-5, where method 1C is the result of method 1 on the clinical dataset and method 1P is the result of method 1 on the public dataset and so on and where method 3MC is the result of method 3 modification in the clinical dataset and method 3MP is the result of method 3 modification on the public dataset.

In terms of the F-measure for the complete tumour, the SegNet_GLCM_DT method provided the highest score in the chart when BRATS 2017 and clinical dataset were used. The scores were 0.98 and 0.90, respectively, for WT segmentation. Meanwhile the SegNet_Max_DT method achieved F-measures of 0.81 and 0.78 respectively for the tumour core, and 0.79 and 0.75 for the enhanced tumour in the BRATS 2017 and clinical datasets. These values are the highest scores in terms of tumour core and enhanced tumour in the chart. The CIFAR_PI_HIS _DT method provided an F-measure of 0.84 and 0.79 for the whole tumour using the BRATS 2017 and clinical datasets, respectively, which were very close to the SegNet_Max_DT method rates (i.e. 0.85 and 0.81).

Still, it should be highlighted that the quantitative results achieved in the clinical dataset were sometimes lower than the performed results in BRATS 2017 dataset. This may have happened because the BRATS 2017 dataset was provided by a specific website for scientific use and is downloaded by means of a 3T MRI scanner. Therefore, this dataset has high resolution with a better signal-to-noise ratio than the clinical dataset has. The latter is downloaded via a 1.5 T scanner; hence, the image slices usually have a lower resolution.

Overall, the promising results in the BRATS 2017 and clinical dataset show the great potential of these three developed methods in brain tumour segmentation. They are highly eligible for clinical diagnostic applications.

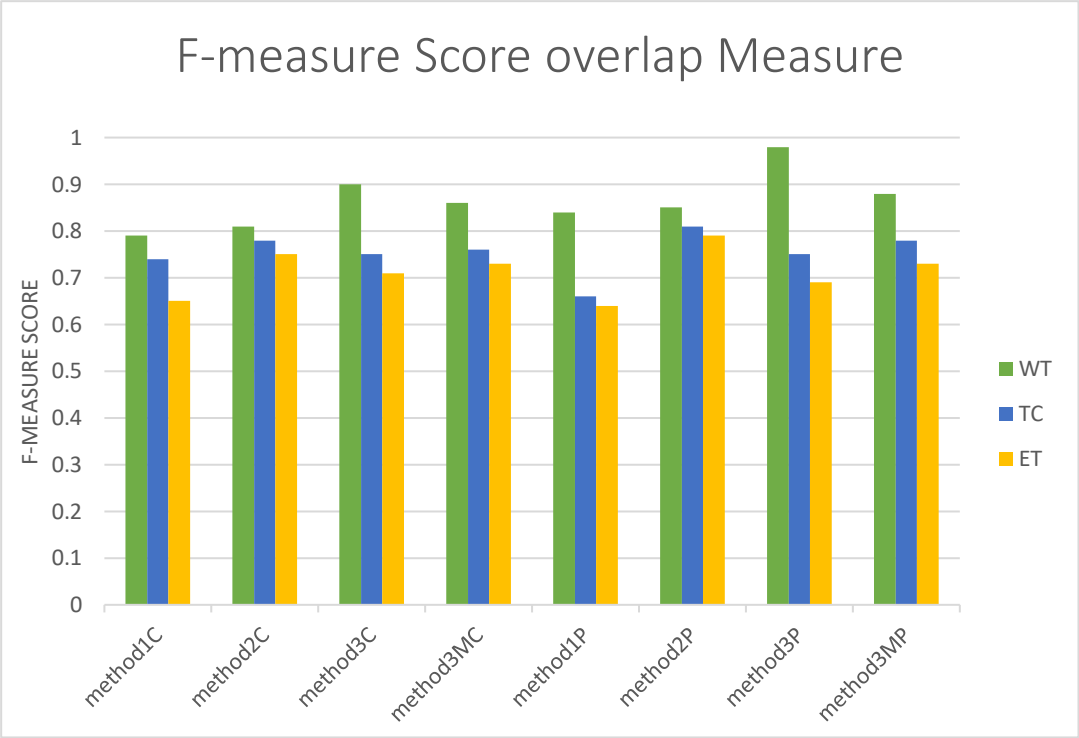

Figure 7-5: Comparison of F-measure with the three developed methods of brain tumour segmentation using BRATS 2017 and a clinical dataset.

7.3 Stroke lesion Segmentation

In this section, the three developed methods for brain tumour segmentation are reported as used in the task of stroke lesion segmentation. The clinical stroke lesion dataset, when collected, was used with the ISLES 2015 to train and test these three modified segmentation methods. In this section, the details of these modified proposed methods for stroke lesion segmentation are discussed, including the dataset, the transferred learning now used for stroke lesion segmentation and the evaluation results.

7.3.1 Dataset

All the patient subjects of the clinical dataset and the ISLES 2015 dataset (58 patient files) were included in this study. In total, 80% of the patients (22 public and 24 clinical data) were used for training the developed segmentation methods and 20% of them (6 public and 6 clinical datasets) were assigned to the testing set. The details of these datasets are presented in Section 2.5.2, above. We excluded T1 modality in the experiments because this modality was unavailable in the clinical dataset and contains comparatively little information for the stroke lesion area.

The three acquired MRI sequences (FLAIR, DWI and T2) of the clinical dataset were pre-processed to allow easy application of the proposed methods for the stroke lesion segmentation task. Skull stripping is a common pre-processing stage in most MRI brain segmentation techniques (Menze et al. 2015). It is a method of separating the brain tissues and non-brain tissues from the skull. In Choubey and Agrawal (2012), the importance of skull stripping in MRI brain image analysis is pointed out. In this work, the skull is removed from all the MRI sequences using 3D Slicer software (3D Slicer 2019).

Registration is another important pre-processing step for brain image segmentation because it ensures the same slice position of all the MRI sequences, which allows optimal image measurement and evaluation. The T2 and DWI images are registered according to the corresponding FLAIR images of MRI sequences, while also using MATLAB's building functions. The ground truth of the ischemic lesion dataset was manually annotated by knowledgeable experts in the hospital.

7.3.2 Transfer Learning for Stroke Lesion Segmentation

In this thesis, CIFAR and SegNet deep learning networks were used in the three proposed methods of brain tumour segmentation. These trained networks can again be employed to train for the task of stroke lesion segmentation because they usually have initialised weights from the images of brain tissues. It entails some modifications to these deep learning networks, but it is helpful to fine tune these networks with the transfer learning for the stroke lesion segmentation task and easier than training the networks from scratch, especially given the small size of the stroke lesion training dataset. First, according to the input data, the three MRI sequences of stroke lesion

(FLAIR, DWI and T2) were used to figure the input data instead of the MRI protocols used for a brain tumour. We then specified the size of the input images in relation to the size of the previously used images of a brain tumour in each network. Second, to fine-tune and retrain the CIFAR and SegNet networks for stroke lesion segmentation, we replaced the last layers and set the fully connected layer (FC2) of the network, which originally had four classes, to a more suitable number of classes, i.e. two (i.e. background and stroke lesion). Moreover, we increased the learning rate factors of the fully connected layer to learn more quickly in the new layers than in the transferred layers.

7.3.3 Experiment Results

In this section, the data pre-processing implementation and data augmentation are described, before reporting the experiments of the three proposed segmentation methods for stroke lesion segmentation. Finally, the evaluation and the comprehensive experimental results are discussed in order to produce quantitative evaluations.

A- Pre-processing

The intensity of each image slice is initially normalized by subtracting the mean of the image intensities and dividing the result by their standard deviation. An N4ITK filter was applied to ensure that all of the data had a similar range of intensities. Then, only patches of 32×32 were extracted after being combined with the three MRI sequence images of stroke lesion (i.e. FLAIR, DWI and T2). The aim in the stroke lesion segmentation task is to segment only one region (i.e. the stroke lesion area). In addition, all of the MRI sequences of the clinical dataset represent the information that helps to separate the whole lesion boundary region from the healthy tissue in the brain. Therefore, a fixed square with a window size of 64 × 64 was not used in this task. The patch extraction pre-processing was implemented only on the data for the first proposed method.

B- Data Augmentation

To avoid overfitting because of the small size of the training dataset, two types of data augmentation were deployed in this work. First, the data were augmented by horizontally and vertically flipping, and randomly rotating the extracted patches.

Second, we oversampled the extracted patches with pixel lesions to address the class imbalance. The data were augmented in the training dataset only, with their labels.

7.3.3.1 CIFAR _PI_HIS_DT for Stroke Lesion Segmentation

After transfer learning in the CIFAR network for stroke lesion segmentation, the CIFAR-based features were extracted as machine features. A two-dimensional feature vector was constructed from each pixel in combined MRI images (i.e. FLAIR, DWI and T2) with values that were equivalent to the probability values of the feature extraction layer. The histogram-based texture features were extracted according to the number of clusters, which was equal to four. We did this because the major tissues in MR images of stroke lesion are of four types, namely, WM, GM, CSF and the stroke lesion region.

The histogram of the quantized image was calculated in the same 9×9 fixed window, which is centred on the corresponding pixel. The details of the histogram-based texture features were discussed in Section 4.3.3. Consequently, the feature vector that is calculated by combining the machine features with the histogram-based texture features and pixel intensity in the MRI sequences comprises nine elements. Then these feature vectors were fed into the DT classifier to train the model for stroke lesion segmentation.

Evaluation

The trained model was tested separately on the clinical testing dataset and the ISLES 2015 testing dataset. Figure 7-6 plots some examples of predicted results for the patients, where the lesions were in different regions in the brain tissue.

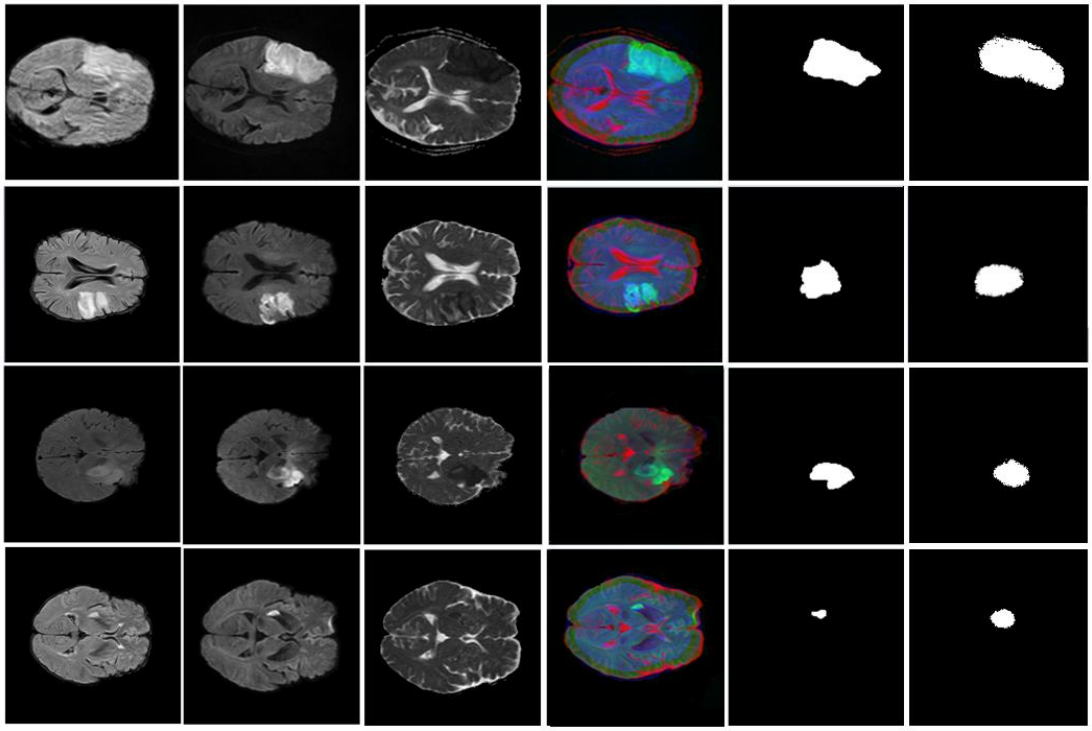

Figure 7-6: Examples of stroke lesion segmentation. MRI sequences of stroke lesion (FLAIR, DWI and T2), three combined MRI sequences, ground truth images and predicted masks (left to right).

As Figure 7-6 shows, the CIFAR _PI_HIS_DT model is sensitive when used to segment large and small stroke lesion areas. Table 7-4 summarizes the results for the stroke lesion testing datasets. It can be seen from the results that the modified CIFAR_PI_HIS _DT model can separate the region that includes the lesion, but it cannot accurately determine the boundaries of the stroke lesion area.

Table 7-4: Performance of the CIFAR_PI_HIS _DT model on the clinical testing dataset and the ISLES 2015 dataset of stroke lesion cases.

Method	F-measure	
	Clinical dataset	ISLES 2015
CIFAR_PI_HIS _DT	0.62	0.49

7.3.3.2 SegNet_Max_DT for Stroke Lesion Segmentation

With regard to the 3D database construction, no 3D MRI database generation was performed because of the small size of the training dataset. There are four MRI modalities (i.e. FLAIR, T1, T1ce and T2) in the BRATS 2017 dataset. Therefore, four MRI modalities were implemented when the SegNet_Max_DT model was used for brain tumour segmentation. In the clinical stroke lesion dataset, only three MRI sequences were acquired (i.e. FLAIR, DWI and T2). Therefore, three MRI sequences were used in the SegNet_Max_DT model for stroke lesion segmentation. Transfer learning was implemented in the three selected pre-trained SegNet models (SegNet1-Flair, SegNet2-T1ce and SegNet4-T2) for stroke lesion segmentation. Flair, DWI and T2 respectively were used in pre-training the SegNet1-Flair, SegNet2-T1ce and SegNet4-T2 models. These three models were selected because they achieved higher performance accuracy in the complete tumour segmentation than the SegNet4-T1 model, and only three models were needed.

After transfer learning and obtaining the SegNet1-Flair, SegNet2-DWI and SegNet3-T2 models, the two highest score maps were extracted from the last deconvolution layer in each model. They were joined with the pixel intensity values of the three original MRI sequence images (i.e. Flair, DWI and T2) and seen as feature vectors. Finally, the feature vectors of five element length were introduced into a DT classifier for stroke lesion segmentation.

Evaluation

Table 7-5 provides the evaluation results obtained by applying the SegNet_Max_DT segmentation on the stroke lesion testing datasets. Figure 7-7 demonstrates some segmented stroke lesion examples from patient cases. From this result, it can be seen that the SegNet_Max_DT method is able to successfully segment stroke lesion with greater accuracy than the CIFAR _PI_HIS_DT model.

Table 7-5: Performance result of SegNet_Max_DT model on the clinical testing dataset and ISLES 2015 stroke lesion dataset.

Method	F-measure	
	Clinical dataset	ISLES 2015
SegNet_Max_DT	0.68	0.52

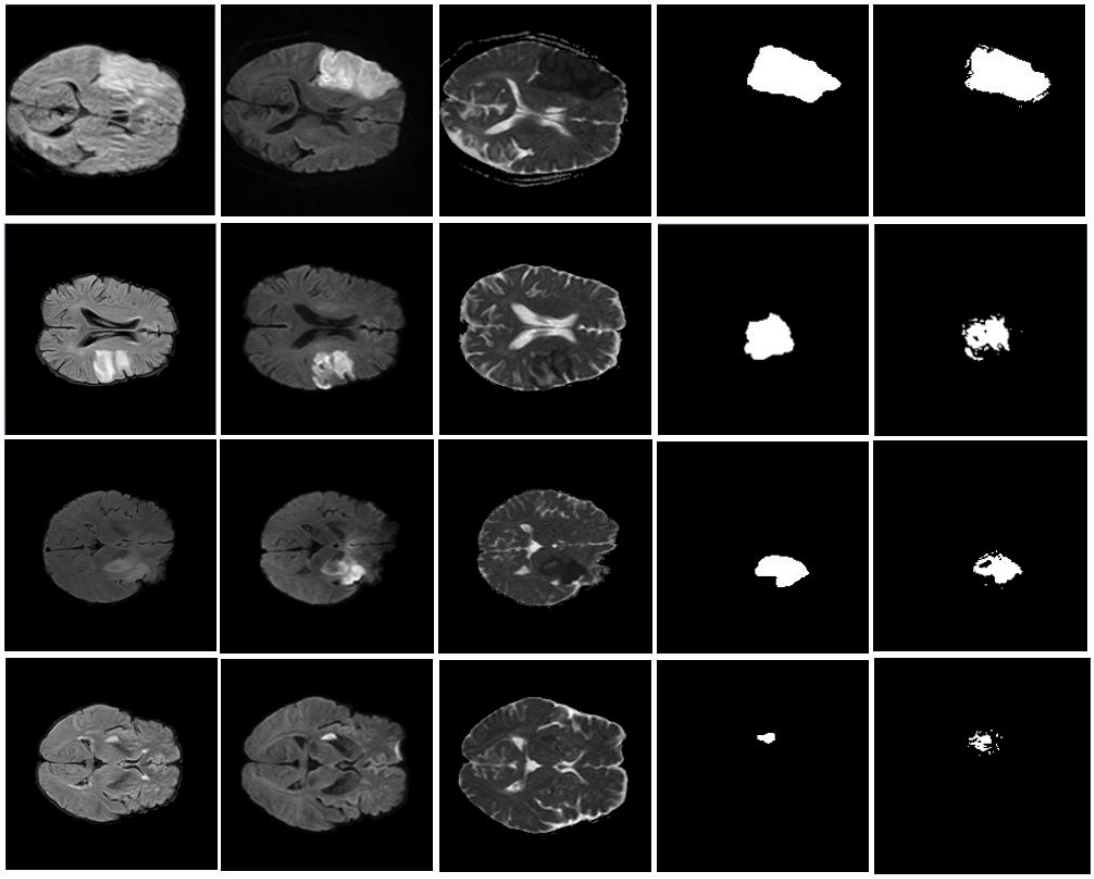

Figure 7-7: Examples of stroke lesion segmentation. MRI sequences of stroke lesion (FLAIR, DWI and T2), ground truth images and predicted masks (left to right).

7.3.3.3 SegNet_GLCM_DT for Stroke Lesion Segmentation

As mentioned in Section 6.2.3.1 (C- Best ROI Masks), the ROI masks of stroke lesion were generated on the basis of transfer learning from the ROI_FLAIR_SegNet model of brain tumour, using FLAIR images of stroke lesion. Then the ROI images of stroke lesion were generated by combining the three MRI sequences (i.e. FLAIR, DWI and T2) based on those ROI masks (see Section 6.2.4).

The trained SegNet network for brain tumour segmentation in Section 6.2.5 was also retrained for stroke lesion segmentation using ROI stroke images. The machine features that represent the score maps which are equal to the number of labels (i.e. background and stroke lesion) were extracted from the last deconvolution layer in the trained SegNet network for stroke lesion segmentation. Meanwhile, the GLCM-based texture features that are represented as crafted-designed features were extracted in a fixed size 8×8 window, centred on this pixel in FLAIR images of a stroke lesion. The FLAIR MRI sequence was selected because the stroke lesion has clearer boundaries in this modality, which improves the segmentation of the stroke lesion. The same three textural features that were used in Section 6.2.6.1 were extracted from each special-dependence matrix of the grey level for distance d=1. The deep learning-based and hand-crafted features were combined to make a feature vector length equal to five elements, which was later fed into the decision tree classifier for stroke lesion segmentation.

Evaluation

The trained network was tested on the stroke lesion testing datasets. Table 7-6 summarises the results for both testing datasets. Figure 7-8 plots the same examples of segmentation in Figure 7-6 and Figure 7-7, where the lesions are located in different parts of the brain.

Table 7-6: Performance result of SegNet_GLCM_DT model on the clinical and ISLES 2015 test datasets of stroke lesion.

Method	F-measure	
	Clinical dataset	ISLES 2015
SegNet_GLCM_DT	0.75	0.57

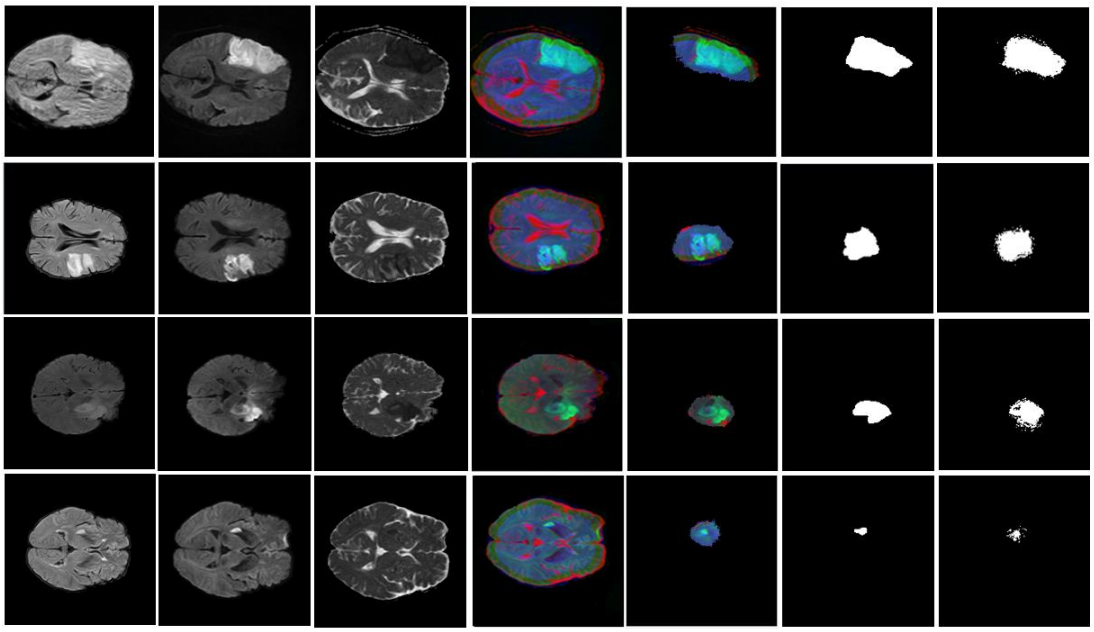

Figure 7-8: Examples of stroke lesion segmentation. MRI sequences of stroke lesion (FLAIR, DWI and T2), three combined MRI sequences, ROI images, ground truth images and predicted masks (left to right).

In Figure 7-8, the seventh column shows an example of the fine segmentation results which are better than the initial segmentation, illustrated in the fifth column (ROI masks). The GLCM texture features help the SegNet network to capture some texture features that come from changes in the tissues due to the progress of the lesion. Therefore, the SegNet_GLCM_DT can be said to achieve greater accuracy than the other developed algorithms in the ischemic stroke lesion segmentation.

7.3.4 Discussion for Ischemic Stroke Lesion

This chapter presented new methods for the segmentation of stroke lesion evidence from multi-modal MRI datasets using the three methods proposed in this thesis and employing transfer learning on pre-trained networks. The publicly available ISLES 2015 dataset together with a stroke lesion clinical dataset were used in this investigation to modify and evaluate the three developed segmentation methods of segmenting stroke lesions for clinical diagnosis purposes.

The results of the experiments demonstrate that the CIFAR_PI_HIS_DT and SegNet_MAX_DT methods were able to automatically locate the lesion areas but not accurately segment the lesion structure boundaries. The SegNet_GLCM_DT method achieved the highest scores in the chart, which were 0.57 and 0.75, respectively, for the ISLES 2015 and stroke lesion clinical dataset (see Figure 7-9) where method1C is the result of method 1 on the stroke lesion clinical dataset and method 1P is the result of method 1 on the public dataset (ISLES2015), and so on. It is clear from Figure 7-9 that the results for the clinical dataset are mostly higher than the results for the public dataset (ISLES2015). This is because the public dataset includes a large variety of patient images as examples (involving different tumour sizes, irregular shapes, and diverse tumour locations) which all affect the segmentation results. The cooperation with the Chinese hospital provided very good evidence of the accuracy of our work. Moreover, our evaluation results in the clinical dataset were considered by clinician experts, who stated that the output predicted segmentation masks were very precise in diagnosing stroke lesion and better than manual segmentation.

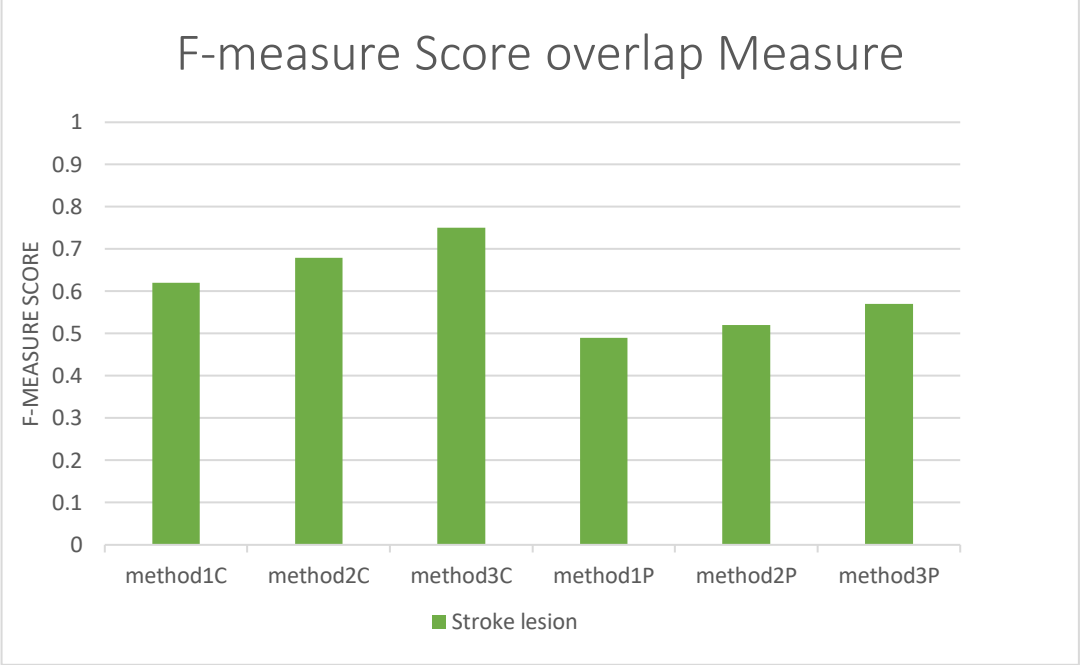

Figure 7-9: Comparison of F-measure with the three developed methods of ischemic stroke lesion segmentation using ISLES 2015 and a clinical dataset.

In Table 7-7, the quantitative results of the best modified segmentation method (SegNet_Max_DT) in subacute stroke lesion segmentation are in the upper range of previous works (Halme et al. 2015; Reza and Iftekharuddin 2015; Robben et al. 2015 and Feng et al. 2015). However, in some cases, our accuracy is slightly lower than the state-of-the art method in Kamnitsas et al. (2015). This is because we have only small datasets, so the experimental results cannot fully reflect the potential of the proposed method. Additionally, it is worth mentioning that the state-of-the-art method, such as reported in Kamnitsas et al. (2015), used more MRI modalities (including T1, T2, DWI and FLAIR) than ours. The incorporation of multi-modal MRI information can help to enhance the accuracy of the segmentation results. It is expected that the accuracy of the proposed method (SegNet_GLCM_DT) will increase if more MRI modalities and large datasets are available. Still, the results achieved with the method proposed in this work (SegNet_GLCM_DT) can be considered very good. Moreover, it is beneficial to segment multiple stroke lesions very accurately (see Figure 7-8). Finally, the proposed method is flexible enough to add to other MRI sequences and thus improve the segmentation results of stroke lesion.

Table 7-7: Performance of our proposed method (Modified SegNet_GLCM_DT) compared with other methods on the ISLES 2015 dataset.

Methods	F-measure
Halme et al. (2015)	0.47
Reza and Iftekharuddin (2015)	0.43
Robben et al. (2015)	0.43
Kamnitsas et al. (2015)	0.59
Feng et al. (2015)	0.55
Modified SegNet_GLCM_DT	0.57

Overall, the modified segmentation methods achieved a promising result in stroke lesion segmentation, especially in the SegNet_GLCM_DT method in the follow up clinical and ISLES 2015 datasets. In addition, employing transfer learning to adapt brain tumour segmentation for stroke lesion segmentation, as proposed in this chapter could open the way to adapting many methods of brain tumour segmentation with deep learning to stroke lesion segmentation in the future.

7.4 Conclusion

In this chapter a clinical brain tumour dataset was used to further assess the robustness of the three suggested methods of brain tumour segmentation for clinical diagnostic use. The results achieved with clinical brain tumour and BRATS 2017 datasets were compared. The adaptation and evaluation of the three developed methods for ischemic stroke lesion segmentation using ISLES 2015 and clinical dataset were described. These modified methods for the stroke lesion task achieved good segmentation results, especially in the third modified segmentation method (SegNet_GLCM_DT) on the ISLES 2015 and clinical datasets.

Chapter 8

Conclusions and Future Work

8.1 Introduction

In this thesis, three different methods were developed to detect and segment brain tumour and sub-tumour regions with gliomas. These methods were CIFAR _PI_HIS _DT, SegNet_Max_DT and SegNet_GLCM_DT. Furthermore, we demonstrated the capabilities of these proposed methods, which can be applied with a few significant modifications to other segmentation tasks, such as ischemic stroke lesion.

8.2 Proposed Methods

In the first successful method (CIFAR _PI_HIS _DT), which was investigated in Chapter 4, we improved the CIFAR network classification by combining CIFAR-learned features with histogram-based texture features to provide a robust descriptor that can indicate the local dependences and provide global information for accurate brain tumour segmentation. The important histogram-based texture features were generated from quantized images of MRI modalities (FLAIR, T1ce and T2) using the Otsu thresholding technique and summing up the intensity values of the original MRI modalities (i.e. FLAIR, T1ce and T2) that corresponded to each cluster in a specific window size. Experimentally, we found that the improved CIFAR_PI_HIS_DT method was more robust and discriminatory in segmenting the tumour and sub-tumour regions than the CIFAR, CIFAR-DT or CIFAR_PI_DT methods. This method demonstrated high performance with F-measures of 0.84, 0.66 and 0.64, respectively, in whole tumour, tumour core and enhanced tumour segmentation, using public data (BRATS 2017).

In the second proposed method (SegNet_Max_DT), which was studied in Chapter 5, we presented a new technique: combining maximum feature maps in the four SegNet models (SegNet1-Flair, SegNet2-T1ce, SegNet3-T1 and SegNet4-T2) to better exploit the multi-modalities of MRI and 3D data information. The 3D data information was optimised by joining three slice sequences (***j-1, j, j+1***) in each MRI modality and using them as input data to the SegNet network. Four maximum map features were selected from 16 machine-learned features across the range of MRI modalities to improve the employment of the hierarchy map features alone. It took account of the various brain tumour segmentation labels (i.e. background, oedema, necrosis and enhanced tumour).

The experimental results show that the 3D joint slices method further uses 3D data information. In addition, the method of selecting maximum features in the SegNet_Max_DT model shows potential, providing consistent improvement on the configuration of our model. SegNet_Max_DT using the BRATS 2017 dataset demonstrated higher segmentation performance than the state-of-the art methods in tumour core and enhanced tumour, yielding F-measures of 0.81 and 0.79, respectively, but it achieved 0.85 in the whole tumour segmentation, which is less than state-of-the art.

In the third method (SegNet_GLCM_DT) that we developed, ROI was initially segmented using a single modality (FLAIR). The ROI_FLAIR_SegNet model was mainly based on the deep learning method (SegNet) for the initial segmenting of the complete tumour structure and generation of ROI masks. The ROI masks were exploited to make ROI images that contained three MRI modalities (FLAIR, T1ce and T2) and used as an input to train the SegNet network. Combining machine learned features with hand-crafted features helps to compensate for the limitations of SegNet and is a powerful adjunct in brain tumour segmentation. Therefore, we extracted machine-based learned features and hand-crafted based features from the corresponding pixels in the ROI images. The machine-learned features were extracted from the last full convolution layer in the trained SegNet network (i.e. background, oedema, necrosis and enhanced). Haralick GLCM were used as hand-crafted features: they form a diverse set of unrelated functions computed from the co-occurrence matrices. ASM, contrast and correlation features were the most important and effective for improving the segmentation of a brain tumour. We used square 8×8 blocks to extract the GLCM features from the T1ce image modality of the corresponding pixel. Consequently, seven elements were involved in the combined feature vector for each corresponding pixel, which were then fed into DT to classify the pixel. The experimental results show that although the combined feature vector of the SegNet_GLCM_DT method has only seven elements, using the BRATS 2017 dataset it can discriminate and can segment brain tumour regions with F-measures of 0.98, 0.75 and 0.69 for whole tumour, tumour core and enhanced tumour, respectively.

Some modifications were made to the SegNet_GLCM_DT method to increase its robustness in segmenting the tumour core and enhanced tumour structures. In the first modification, the SegNet_GLCM_DT model was trained and tested to provide three label predicted masks (i.e. background, necrosis and enhanced tumour). The second modification was to add the mask fusion method, which combined the ROI masks of two labels (i.e. background and complete tumour) and three labels to obtain final segmentation masks of all of the brain tumour regions. The experimental results illustrate that adding the modifications to the pipeline of the SegNet_GLCM_DT method improves the accuracy of the F-measure for core and enhanced tumour regions (0.78 and 0.73, respectively) because of the significant influence of the segmentation results of the SegNet network on the accuracy when the training involves fewer classes.

8.2.1 Application to Brain Tumours

To further assess the robustness of the three proposed methods, a practical clinical brain tumour dataset was used to evaluate them.

The first segmentation method (CIFAR_PI_HIS_DT) had F-measures of 0.79, 0.74 and 0.65 for WT, TC and ET, respectively. In the second proposed method (SegNet_Max_DT), the performance of the F-measure for WT, TC and ET measured 0.81, 0.78 and 0.75, respectively. The third segmentation method (SegNet_GLCM_DT) achieved 0.90, 0.75 and 0.71 accuracy for WT, TC and ET, respectively, while the modified SegNet_GLCM_DT obtained 0.86, 0.76 and 0.73 accuracy for WT, TC and ET, respectively.

Overall, the results achieved from the three proposed methods using BRATS 2017 and practical clinical datasets are comparable in brain tumour segmentation

8.2.2 Application to Ischemic Stroke Lesion

We tested the ability of our three brain tumour segmentation methods in an ischemic stroke lesion segmentation task. A few modifications were made to these proposed methods for stroke lesion segmentation.

In the first segmentation method (CIFAR _PI_HIS _DT), we transferred the learning in CIFAR into stroke lesion classification. In the histogram texture feature extraction, four

clusters were selected because there are four tissue types (i.e. WM, GM, CSF and stroke lesion) in the MRI images of stroke lesions. The machine learning features were combined with the histogram-based texture features that were extracted from the combined MRI modalities (i.e. FLAIR, DWI and T2). The length of the feature vector was nine elements, which were then fed into DT to classify the pixels. Experimentally, we found that the modified CIFAR_PI_HIS _DT model is able to segment a stroke lesion with an F-measure of 0.62 when the clinical dataset was used and 0.49 when the ISLES 2015 dataset was used.

In the second segmentation method (SegNet_Max_DT), SegNet1-Flair, SegNet2-T1ce and SegNet4-T2 models were selected to implement the transfer learning, while the SegNet1-Flair, SegNet2-DWI and SegNet3-T2 models that had been obtained were implemented for stroke lesion segmentation using Flair, DWI and T2 MRI modalities. The feature vector was produced by combining the two highest scoring maps that had been extracted from the last fully convolutional layer in each model and the pixel intensity values of the original MRI sequences of stroke lesion (i.e. Flair, DWI and T2). A five-feature vector was used as input to DT to classify the pixels. The corresponding result for the ISLES 2015 experiment was 0.52, while the F-measure in the clinical dataset experiment was 0.68. The experimental results illustrate that the performance of this suggested algorithm is better than that of our previously proposed algorithm (CIFAR _PI_HIS _DT) in stroke lesion segmentation.

In the third segmentation method (SegNet_GLCM_DT), the transfer learning was implemented in the ROI_FLAIR_SegNet model as a first step in detecting the location of initial stroke lesions and generating ROI masks using a single modality (FLAIR). ROI masks were used to generate ROI images from MRI modalities (FLAIR, DWI and T2). The learning in the SegNet network (investigated in Section 6.2.5) was transferred to stroke lesion segmentation. The GLCM method considers hand-crafted features that are described in the FLAIR modality by an 8×8 block of the corresponding pixel. Hand crafted features (i.e. ASM, contrast and homogeneity) were then combined with machine-based learned features of SegNet (i.e. background and stroke lesion) to produce more accurate stroke lesion segmentation. The experimental work shows that incorporating the GLCM-specified features with the machine-based features improved the segmentation of stroke lesions; for example, it increased the F-measure from 0.55 to 0.75 and from 0.46 to 0.57 when the clinical dataset and ISLES 2015 dataset, respectively, were used.

Overall, CIFAR _PI_HIS _DT and SegNet_Max_DT methods were able to segment the stroke lesion. However, the SegNet_GLCM_DT method provided the best results of all the algorithms in the stroke lesion segmentation task because this method makes use of the advantages of both machine-learned based and hand-crafted features to produce more accurate segmentation. The SegNet features in the third method were able to detect and localise the stroke lesion with fewer false positives. Meanwhile, the hand-crafted GLCM features were able to accurately segment the stroke lesion boundaries and provide fine segmentation outputs.

8.3 Future work

Below, we introduce some of the ideas that we would wish to pursue in future research projects.

1- In CIFAR_PI_HIS _DT, SegNet_Max_DT and SegNet_GLCM_DT methods, a larger clinical database of brain tumour and stroke lesion could be used to make the training process more efficient. Additionally, these methods could be applied to other more complicated and clinically important medical imaging problems that need to be investigated.

2- We want to adapt the algorithm that was developed in Chapter 4 to classify the types of brain tissue injury (i.e. brain tumour or ischemic stroke lesion) by training this model with many examples from the brain tumour and ischemic stroke lesion databases.

3- We want to study the effect of tumour size on the segmentation efficiency of each developed method by calculating the F-measure for each patient and to find the limitations (if any) in our proposed methods.

4- To guide clinical treatment, the classification of stroke lesion should be perfectly achieved. Therefore, more MRI images should be collected, including all types of stroke lesion.

References

3D Slicer, 2019. Available at: http://www.slicer.org/ [Accessed: 11 July 2019].

Abulnaga, S.M. and Rubin, J. 2018. Ischemic stroke lesion segmentation in CT perfusion scans using pyramid pooling and focal loss. In International MICCAI Brainlesion Workshop (pp. 352-363). Springer, Cham.

AG, A.P. and Pattar, S.Y. 2017. Textural feature extraction and analysis for brain tumors using MRI. International Journal of Scientific and Research Publications 7(8).

Albers, G.W. 1998. Diffusion-weighted MRI for evaluation of acute stroke. Neurology 51(3 SUPPL.)

Alqazzaz, S. et al. 2019. Automated brain tumor segmentation on multi-modal MR image using SegNet. Computational Visual Media 5(2), pp. 209–219.

Alvarez, J.M. et al. 2012. Road scene segmentation from a single image. In European Conference on Computer ision (pp. 376-389). Springer, Berlin, Heidelberg.

Amiri, S. et al. 2016. Deep random forest-based learning transfer to SVM for brain tumor segmentation. In: 2nd International Conference on Advanced Technologies for Signal and Image Processing, ATSIP 2016., pp. 297–302.

Angelini, E. et al. 2007. Glioma dynamics and computational models: A review of segmentation, registration, and in silico growth algorithms and their Clinical Applications. Current Medical Imaging Reviews 3(4), pp. 262–276.

Azhari, E.E.M. et al. 2014. Tumor detection in medical imaging: A survey. International Journal of Advanced Information Technology, 4(1), p.21.

Badrinarayanan, V. et al. 2017. Segnet: A deep convolutional encoder-decoder architecture for image segmentation. IEEE Transactions on Pattern Analysis and Machine Intelligence 39(12), pp.

Bakas, S. et al. 2017. Segmentation labels and radiomic features for the pre-operative scans of the TCGA-GBM collection. The Cancer Imaging Archive.

Bakas, S. et al. 2017. Advancing the cancer genome atlas glioma MRI collections with expert segmentation labels and radiomic features. Scientific Data 4(July), pp. 1–13.

Bakas, S. et al. 2018. Identifying the best machine learning algorithms for brain tumor segmentation, progression assessment, and overall survival prediction in the BRATS challenge.

Barucci, A. et al. 2016. Diffusion-Weighted MR imaging: Clinical applications of kurtosis analysis to prostate cancer. ArXiv Preprint ArXiv:1611.08163.

Basser, P.J. and Jones, D.K. 2002. Diffusion-tensor MRI: Theory, experimental design and data analysis - A technical review. NMR in Biomedicine 15(7–8), pp. 456–467.

Bauer, S. et al. 2013. Integrated segmentation of brain tumor images for radiotherapy and neurosurgery. International Journal of Imaging Systems and Technology 23(1), pp. 59–63.

Bauer, S. et al. 2013a. A survey of MRI-based medical image analysis for brain tumor studies. Physics in Medicine and Biology 58(13). doi: 10.1088/0031-9155/58/13/R97.

Bharath, H.N. et al. 2017. Tumor segmentation from multimodal MRI using random forest with superpixel and tensor based feature extraction. Springer, Cham , pp. 463–473.

Bjornerud, A. 2008. The Physics of Magnetic Resonance Imaging: FYS-KJM 4740. Department of Physics.

Brain Tumour Research . What's the difference between primary and secondary brain tumours? Available at: https://www.braintumourresearch.org/info-support/what-is-a-brain-tumour? [Accessed: 8 June 2019].

Brostow, G.J. et al. 2009. Semantic object classes in video: A high-definition ground truth database. Pattern Recognition Letters, 30(2), pp.88-97.

Casamitjana, A. 2017. Cascaded V-Net using ROI masks for brain tumor segmentation. In International MICCAI Brainlesion Workshop (pp. 381-391). Springer, Cham.

Castillo, L.S. et al. 2017. Volumetric multimodality neural network for brain tumor segmentation. In 13th International Conference on Medical Information Processing and Analysis . International Society for Optics and Photonics, (Vol. 10572, p. 105720E).

Chang, P.D. 2016. Fully convolutional deep residual neural networks for brain tumor segmentation. In International Workshop on Brainlesion: Glioma, Multiple Sclerosis, Stroke and Traumatic Brain Injuries . Springer, Cham, (pp. 108-118).

Chen, L. et al. 2017. Fully automatic acute ischemic lesion segmentation in DWI using

convolutional neural networks. NeuroImage: Clinical 15(January), pp. 633–643. doi: 10.1016/j.nicl.2017.06.016.

Chen, L. et al. 2018. Apparent diffusion coefficient value for prediction of hemorrhagic transformation in acute ischemic infarction. 11(1), pp. 109–117.

Chen, S. et al. 2017. Brain tumor segmentation with label distribution learning and multi-level feature representation. 2017 International MICCAI BRATS Challenge.

Chitradevi, A. and Sadasivam, V. 2016. Various approaches for medical image segmentation: A survey. Current Medical Imaging Reviews 12(2), pp. 77–94.

Choubey, M. and Agrawal, S. 2012. A fully automatic approach to detect brain cancer using random Walk Algorithm. 3(1), pp. 265–268.

Davy, A. et al. 2014. Brain tumor segmentation with deep neural networks. Medical Image Analysis 35, pp. 18–31.

Donahue, J. et al. 2014. Decaf: A deep convolutional activation feature for generic visual recognition. Jmlr.org .

Drevelegas, A. and Papanikolaou, N. 2011. Imaging modalities in brain tumors. In Imaging of brain tumors with Histological Correlations (pp. 13-33). Springer, Berlin, Heidelberg.

Eftimov, T. et al. 2007. Management of recurrent high-grade gliomas. Cancer Therapy 5, pp. 243–252.

Fasihi, M. S. and Mikhael, W.B. 2016. Overview of current biomedical image segmentation methods. 2016 International Conference on Computional Science and Computional Intelligence , pp. 803–808.

Feng, C. et al. 2015. Segmentation of ischemic stroke lesions in multi-spectral MR images using weighting suppressed FCM and three phase level set. In BrainLes 2015 (pp. 233-245). Springer, Cham.

Fink, J.R. 2015. Multimodality brain tumor imaging: MR imaging, PET, and PET/MR imaging. Journal of Nuclear Medicine, 56(10), pp.1554-1561.

Gardner, W.J. 2018. Brain Tumors. Postgraduate Medicine 1(6), pp. 454–459.

Garcia-Garcia, A. et al. 2017. A review on deep learning techniques applied to semantic segmentation. ArXiv Preprint ArXiv:1704.06857.

Goetz, M. et al. 2015. DALSA: Domain adaptation for supervised learning from sparsely annotated MR Images. IEEE Transactions on Medical Imaging 35(1), pp. 184–196.

Goodenberger, M.L. and Jenkins, R.B. 2012. Genetics of adult glioma. Cancer Genetics 205(12), pp. 613–621.

Gordillo, N. et al. 2013. State of the art survey on MRI brain tumor segmentation. 31, pp. 1426–1438.

Hagmann, P. et al. 2006. Understanding diffusion MR imaging techniques: From scalar diffusion-weighted imaging to diffusion tensor imaging and beyond. Radiographics 26(SPEC. ISS.), pp. 205–224.

Halme, H.L. et al. 2015. ISLES (SISS) challenge 2015: segmentation of stroke lesions using spatial normalization, random forest classification and contextual clustering. In BrainLes 2015 (pp. 211-221). Springer, Cham.

Haralick, R.M. et al. 1973. Textural features for image classification. IEEE Transactions on Systems, Man and Cybernetics SMC-3(6), pp. 610–621.

Harefa, J. et al. 2017. Comparison classifier: support vector machine (SVM) and K-nearest neighbor (K-NN) in digital mammogram images. Jurnal Informatika dan Sistem Informasi, 2(2), pp.35-40.

Hassan, E. and Aboshgifa, A. 2015. Detecting brain tumour from MR image using matlab GUI programme. International Journal of Computer Science & Engineering Survey 6(6), pp. 47–60.

Havaei, M. et al. 2017. Brain tumor segmentation with Deep Neural Networks. Medical Image Analysis 35, pp. 18–31.

Holli, K.K. et al. 2010. Texture analysis of MR images of patients with mild traumatic brain injury. BMC Medical Imaging 10(8).

Hsu, C. W. et al. 2003. A practical guide to support vector classification. Department of Computer Science, National Taiwan University.

Huang, Z.Y. et al. 2005. Characterization of mercurial-bound metallothioneins in rat kidney by hyphenated techniques. Chinese Journal of Inorganic Chemistry .

Huisman, T.A. 2010. Diffusion-weighted and diffusion tensor imaging of the brain,

made easy. Cancer Imaging, 10(1A), p.S163.

Hu, K. et al. 2019. Brain tumor segmentation using multi-cascaded convolutional neural networks and conditional random field. IEEE Access, 7, pp.92615-92629.

Hu, X. et al. 2020. Brain SegNet: 3D local refinement network for brain lesion segmentation. BMC Medical Imaging, 20(1), p.17.

Jalab, H. and Alwaeli, A.M. 2019. Magnetic resonance imaging segmentation techniques of brain tumors: A review. Archives of Neuroscience In Press (In Press), pp. 1–7.

Jin, L. et al. 2014. A Survey of MRI-based brain tumor segmentation methods jin. Tsinghua Science and Technology 19 (6), pp. 578–595.

Jr, P.S. 2000. Magnetic resonance imaging principles , Methods , and Techniques.

Juan-Albarracín, J. et al. 2015. Automated glioblastoma segmentation based on a multiparametric structured unsupervised classification. Plos one 10(5), pp. 1–20.

Kamnitsas, K. et al. 2015. Multi-scale 3D convolutional neural networks for lesion segmentation in brain MRI. Ischemic stroke lesion segmentation, 13, p.46.

Kamnitsas, K. et al. 2017. Efficient multi-scale 3D CNN with fully connected CRF for accurate brain lesion segmentation. Medical Image Analysis 36, pp. 61–78.

Kamnitsas, K. et al. 2018. Ensembles of multiple models and architectures for robust brain tumour segmentation. In International MICCAI Brainlesion Workshop (pp. 450-462). Springer, Cham.

Kane, I. et al. 2007. Comparison of 10 different magnetic resonance perfusion imaging processing methods in acute ischemic stroke: Effect on lesion size, proportion of patients with diffusion/perfusion mismatch, clinical scores, and radiologic outcomes. Stroke 38(12), pp. 3158–3164.

Kaur, E.N. and Kaur, E.Y. 2015. Object classification techniques using machine learning model. International Journal of Computer Trends and Technology 18(4), pp. 170–174.

Kesavaraj, G. and Sukumaran, S. 2013. A study on classification techniques in data mining. In 2013 Fourth International Conference on Computing, Communications and Networking Technologies (ICCCNT) (pp. 1-7). IEEE.

Kim, B.J. et al. 2014. Magnetic resonance imaging in acute ischemic stroke treatment. Journal of Stroke 16(3), p. 131.

Kotsiantis, S.B. et al. 2007. Supervised machine learning: A review of classification techniques. Emerging Artificial Intelligence Applications in Computer Engineering, 160, pp.3-24.

Krizhevsky, A. 2009. Learning multiple layers of features from tiny images. Available at: https://www.cs.toronto.edu/~kriz/learning-features-2009-TR. pdf [Accessed: 6 November 2018].

Lai, M. 2015. Deep learning for medical image segmentation. ArXiv Preprint ArXiv:1505.02000.

Lai, Y. et al. 2011. A texture-based classifier to discriminate anaplastic from non-anaplastic medulloblastoma. In: 2011 IEEE 37th Annual Northeast Bioengineering Conference, NEBEC 2011. IEEE, pp. 1–2.

Leeflang, M.M.G. et al. 2018. Annals of internal medicine academia and clinic. academia and clinic 149(12), pp. 889–898.

Li, J. et al. 2017. Pedestrian detection with dilated convolution, region proposal network and boosted decision trees. Proceedings of the International Joint Conference on Neural Networks 2017-May, pp. 4052–4057.

Liao, P.S. et al. 2001. A fast algorithm for multilevel thresholding. Journal of Information Science and Engineering 17(5), pp. 713–727.

Long, J. et al. 2015. Fully convolutional networks for semantic segmentation. IEEE Transactions on Pattern Analysis and Machine Intelligence 39(4), pp. 640–651.

Lorenzo, P.R. et al. 2019. Segmenting brain tumors from FLAIR MRI using fully convolutional neural networks. Computer methods and programs in biomedicine, 176, pp.135-148.

Louis, D.N. et al. 2007. The 2007 WHO classification of tumours of the central nervous system. Acta Neuropathol 114, 97–109.

Louis, D.N. et al. 2016. The 2016 world health organization classification of tumors of the central nervous system: A summary. Acta Neuropathologica 131(6), pp. 803–820.

Maier, O. et al. 2017. ISLES 2015 - A public evaluation benchmark for ischemic stroke lesion segmentation from multispectral MRI. Medical Image Analysis 35, pp. 250–269.

Majnik, M. and Bosni, Z. 2013. ROC analysis of classifiers in machine learning: A survey. Intelligent Data Analysis 17(3), pp. 531–558.

Mayfield Brain and Spine 1999. Anatomy of the Brain. The Internet Stroke Center , pp. 1–6.

Menze, B. et al. 2015. The multimodal brain tumor image segmentation benchmark (BRATS). IEEE Transactions on Medical Imaging 34.

Meier, R. et al. 2013. A hybrid model for multimodal brain tumor segmentation. Multimodal Brain Tumor Segmentation, 31, pp.31-37.

Miller, K. et al. 2010. Biomechanics of the brain for computer-integrated surgery. Acta of Bioengineering and Biomechanics, 12(2), pp.25-37.

Mudry, A. and Tjellström, A. 2011. Historical background of bone conduction hearing devices and bone conduction hearing aids. Advances in Oto-Rhino-Laryngology 71, pp. 1–9.

Myles, A.J. et al. 2004. An introduction to decision tree modeling. Journal of Chemometrics 18(6), pp. 275–285.

Niyazi, M. et al. 2016. ESTRO-ACROP guideline “target delineation of glioblastomas”. Radiotherapy and Oncology, 118(1), pp.35-42.

Noh, H. et al. 2015. Learning deconvolution network for semantic segmentation. In: Proceedings of the IEEE International Conference on Computer Vision., pp. 1520–1528.

Norouzi, A. et al. 2014. Medical image segmentation methods, algorithms, and applications. IETE Technical Review (Institution of Electronics and Telecommunication Engineers, India) 31(3), pp. 199–213.

Odland, A. et al. 2015. Volumetric glioma quantification : comparison of manual and semi-automatic tumor segmentation for the quantification of tumor growth. 56(11), pp. 1396–1403.

Orrù, G. et al. 2012. Using support vector machine to identify imaging biomarkers of

neurological and psychiatric disease: A critical review. Neuroscience and Biobehavioral Reviews 36(4), pp. 1140–1152.

Osman, A.F. 2017. Fully automated glioma brain tumors segmentation and patient overall survival prediction with SVMs learning algorithms. Proceedings of MICCAI-BRATS Challenge, pp.211-218.

Otsu, N. 1979. Otsu 1979 Otsu thresold method. IEEE Transactions on Systems, Man, and Cybernetics 9(1), pp. 62–66.

Paciaroni, M. et al. 2008. Early hemorrhagic transformation of brain infarction: Rate, predictive factors, and influence on clinical outcome: Results of a prospective multicenter study. Stroke 39(8), pp. 2249–2256.

Paolillo, M. and Schinelli, S. 2015. Brain infiltration by cancer cells: different roads to the same target? Journal of Cancer Metastasis and Treatment 0(0), p. 0.

Patil, D.D. and Deore, S.G. 2013. Medical Image Segmentation: A review. International Journal of Computer Science and Mobile Computing 2(1), pp. 22–27.

Pedapati, P. and Tannedi, R.V. 2018. Brain Tumour Detection using HOG by SVM.

Pereira, S. et al. 2016. Brain tumor segmentation using convolutional neural networks in MRI images. IEEE Transactions on Medical Imaging 35(5), pp. 1240–1251.

Pham, D.L. et al. 2000. Current methods in medical image segmentation. Annual Review of Biomedical Engineering, 2(1), pp.315-337.

Phophalia, A. and and Maji, P. 2017. Multimodal brain tumor segmentation using ensemble of forest method. Springer, Cham , pp. 159–168.

Prasanna, P. et al. 2019. Radiomics-based convolutional neural network for brain tumor segmentation on multiparametric magnetic resonance imaging. Journal of Medical Imaging, 6(2), p.024005.

Razzak, M.I. et al. 2018. Efficient brain tumor segmentation with multiscale two-pathway-group conventional neural networks. IEEE Journal of Biomedical and Health Informatics, 23(5), pp.1911-1919.

Rehman, Z.U.et al. 2019. Fully automated multi-parametric brain tumour segmentation using superpixel based classification. Expert Systems with Applications, 118, pp. 598-613.

Revanuru, K. and Shah, N., 2017. Fully automatic brain tumour segmentation using random forests and patient survival prediction using XGBoost. Proceedings of the 6th MICCAI-BRATS Challenge, pp.239-243.

Reza, S.M. and Iftekharuddin, K. 2015. Ischemic stroke lesion segmentation using local gradient and texture features. Ischemic Stroke Lesion Segmentation, p.23.

Roberts, T.P.L. and Mikulis, D. 2007. Neuro MR: Principles. Journal of Magnetic Resonance Imaging 26(4), pp. 823–837.

Robben, D. et al 2015. A Voxel-wise, cascaded classification approach to ischemic stroke lesion segmentation. In BrainLes 2015 (pp. 254-265). Springer, Cham.

Ronneberger, O. et al. 2015. U-net: Convolutional networks for biomedical image segmentation. In International Conference on Medical Image Computing and Computer-Assisted Intervention (pp. 234-241). Springer, Cham.

Roy, S. et al. 2013. A review on automated brain tumor detection and segmentation from MRI of brain. ArXiv Preprint ArXiv:1312.6150.

Ruan, S. et al. 2007. Tumor segmentation from a multispectral MRI images by using support vector machine classification. In 2007 4th IEEE International Symposium on Biomedical Imaging: From Nano to Macro (pp. 1236-1239). IEEE.

Shanthi, K.J. and Kumar, M.S. 2007. Skull stripping and automatic segmentation of brain MRI using seed growth and threshold techniques. 2007 International Conference on Intelligent and Advanced Systems, ICIAS 2007 , pp. 422–426.

Shelhamer, E. et al. 2017. Fully convolutional networks for semantic segmentation. IEEE Transactions on Pattern Analysis and Machine Intelligence 39(4), pp. 640–651.

Singh, A. 2016. A review of supervised machine learning algorithms. In 2016 3rd International Conference on Computing for Sustainable Global Development (INDIACom) (pp. 1310-1315). IEEE.

Springenberg, J.T. et al. 2015. Striving for simplicity: The all convolutional net. arXiv preprint arXiv:1412.6806.

Stieber, V.W. 2016. Low-grade gliomas. Curr Treat Options Oncol 2(1534-6277 (Linking)), pp. 495–506.

Subbanna, N.K. et al. 2019. Stroke lesion segmentation in FLAIR MRI datasets using

customized markov random fields. Frontiers in Neurology, 10, p.541.

The Brain Tumour Charity. 2000. Understanding brain tumours; Glioblastoma Research. Available at: https://www.thebraintumourcharity.org/our-research/research-tumour-type/glioblastoma/.

Tustison, N.J. et al. 2010. N4ITK: Improved N3 bias correction. IEEE Transactions on Medical Imaging 29(6), pp. 1310–20.

Walker, J.M. 2010. Data mining techniques for the life science.

Wallace, F. and Wallace, B.F. 1973. A i t h.

Wang, G. et al. 2017. Automatic brain tumor segmentation using cascaded anisotropic convolutional neural networks. In International MICCAI Brainlesion Workshop (pp. 178-190). Springer, Cham.

Win, S.L. and Urvey, S. 2014. Tumor detection in medical imaging : a. 4(1), pp. 21–29.

Wittenauer, R. and Smith, L. 2012. Ischaemic and haemorrhagic stroke. Priority Medicines for Europe and the World 'A Public Health Approach to Innovation'. Background Paper 6.6 Ischaemic and Haemorrhagic Stroke (December), p. 46.

Wu, B. et al. 2010. Visualizing 3D objects from 2D cross sectional images displayed in-situ versus ex-situ. Journal of Experimental Psychology: Applied, 16(1), p.45.

Zeng, Z. 2013. Medical image segmentation on multimodality images (Doctoral dissertation, Aberystwyth University).

Zhang, R. et al. 2018. Automatic segmentation of acute ischemic stroke from DWI using 3-D fully convolutional DenseNets. IEEE Transactions on Medical Imaging, 37(9), pp.2149-2160.

Zhao, F. and Xie, X. 2013. An overview of interactive medical image segmentation. Annals of the BMVA 2013(7), pp. 1–22.

Zheng, S. et al. 2015. Conditional random fields as recurrent neural networks. In Proceedings of the IEEE International Conference on Computer Vision (pp. 1529-1537).

Zhuang, A.H. et al. 2006. Skull-stripping magnetic resonance brain images using a model-based level set. NeuroImage 32(1), pp. 79–92.

Zikic, D. et al. 2012. Decision forests for tissue-specific segmentation of high-grade gliomas in multi-channel MR. In International Conference on Medical Image Computing and Computer-Assisted Intervention (pp. 369-376). Springer, Berlin, Heidelberg.

Zikic, D. et al. 2014. Segmentation of brain tumor tissues with convolutional neural networks. Proceedings MICCAI-BRATS (September 2014), pp. 36–39.

Appendix

List of Publications

Published Paper

- Alqazzaz, S., Sun, X., Yang, X. and Nokes, L., 2019. Automated brain tumour segmentation on multi-modal MR image using SegNet. Computational Visual Media, 5(2), pp.209-219.
- Al-qazzaz, S., Sun, X., Yang, H., Yang, Y., Xu, R., Nokes, L. and Yang, X., 2020. Image classification-based brain tumour tissue segmentation. Multimedia Tools and Applications, pp.1-16.

Papers under Review

- Al-qazzaz, S., Sun, X., Yang, H., Yang, Y., Xu, R., Zhang, Y., Nokes, L. and Yang, X., 2020. Combined Features in Region of Interest for Brain Tumor Segmentation. Machine Vision and Applications.

- Al-qazzaz, S., Sun, X., Dong, Y., Chen, S., Li, H., Hu, W., Nokes, L. and Yang, X., 2020. Stroke Lesion Segmentation Using Transfer Learning. Multimedia Tools and Applications.